Fall 2021

Design and Development of Soft Earthworm Robot Driven by Fibrous Artificial Muscles

Beau Ragland

DESIGN AND DEVELOPMENT OF SOFT EARTHWORM ROBOT DRIVEN BY FIBROUS ARTIFICIAL MUSCLES

by

BEAU RAGLAND

(Under the Direction of Lianjun Wu)

ABSTRACT

Earthworm robots have proven their viability in the fields of medicine, reconnaissance, search and rescue, and infrastructure inspection. These robots are traditionally typically hard-shelled and must be tethered to whatever drives their locomotion. For this reason, truly autonomous capabilities are not yet feasible. The goal of this thesis is to introduce a robot that not only sets the groundwork for autonomous locomotion, but also is safe for human-robot interaction. This was done by ensuring that the actuation principle utilized by the robot is safe around humans and can work in an untethered design. Artificial muscle actuation allowed for these prerequisites to be met. These artificial muscles are made of fishing line and are twisted, wrapped in conductive heating wire, and then coiled around a mandrel rod. When electrical current passes through the heating wire, the artificial muscles expand or contract, depending on how they were created. After the muscles were manufactured, experiments were done to test their functionality. Data was collected via a series of experiments to investigate the effect of various processing parameters on the performance, such as the diameter of the mandrel coiling rod, the applied dead weight, the applied current, cyclic tests, and pulse tests. After acquiring data from the artificial muscles, a prototype was designed that would incorporate the expansion and contraction artificial muscles. This prototype featured two variable friction end caps on either side that were

driven via expansion muscles, and a central actuation chamber driven via an antagonistic spring and contraction artificial muscle. The prototype proved its locomotion capabilities while remaining safe for human-robot interaction. Data was collected on the prototype in two experiments – one to observe the effect of varying induced currents on axial deformation and velocity, and one to observe the effect of varying deadweights on the same metrics. The prototype was not untethered, but future research in the implementation of an on-board power source and microcontroller could prove highly feasible with this design.

INDEX WORDS: Fibrous artificial muscles, Soft earthworm robot, Soft actuators, Soft robotics, Georgia Southern University

DESIGN AND DEVELOPMENT OF SOFT EARTHWORM ROBOT DRIVEN BY FIBROUS ARTIFICIAL MUSCLES

by

BEAU RAGLAND

B.S., Georgia Southern University, 2020

M.S., Georgia Southern University, 2021

A Thesis Submitted to the Graduate Faculty of Georgia Southern University in Partial Fulfillment of the Requirements for the Degree

MASTER OF SCIENCE

ALLEN E. PAULSON COLLEGE OF ENGINEERING AND INFORMATION TECHNOLOGY

DESIGN AND DEVELOPMENT OF SOFT EARTHWORM ROBOT DRIVEN BY FIBROUS ARTIFICIAL MUSCLES

by

BEAU RAGLAND

Major Professor: Lianjun Wu

Committee: Valdamir Gurau

Yue Zhang

Electronic Version Approved:

December 2021

ACKNOWLEDGMENTS

I would like to thank my thesis chair Dr. Wu for all his gracious help in organizing and facilitating the work done on this thesis. Without his guidance I would not have been able to accomplish what I accomplished, especially in the time frame it was done. Dr. Wu has sacrificed a lot of his time and energy to help me finish this thesis, and for that I am very grateful. I would also like to thank my other committee members Dr. Zhang and Dr. Gurau for agreeing to review and give their valuable feedback to my thesis document. Additionally, I would like to thank my colleagues, peers, and other faculty members in the Manufacturing Engineering program such as Andrew Michaud, Ryan Daigneault, and Dr. Cox for their advice and support.

Finally, I would like to thank my family and girlfriend for their unwavering support through this demanding year and a half. Without their belief in me as well as their thoughts and prayers I would not have had the drive to keep pushing through to the end.

TABLE OF CONTENTS

LIST OF TABLES

LIST OF FIGURES

LIST OF EQUATIONS

CHAPTER 1
INTRODUCTION

Soft earthworm robots are a small niche in the overarching field of soft robotics, which is a subset of the much larger and more encompassing field of robotics. Soft robotics, as their name suggests, are made of soft materials that are typically flexible and stretchable. They vary from the hard materials with invariable mechanical, rheological, and electrical properties. Soft robots can be used to safely interface collaboratively with humans without the fear of serious bodily harm which can be a risk when dealing with traditional hard robots. These soft robots can feature smart materials that can be configured to accommodate 3D printing, making them invaluable in their ease of manufacturing (Alici 2018). They can be actuated in many ways including - servo-driven flexible plates (Hayato, Takeshi, and Nakamura 2008), pneumatically (Heung, Chiu, and Li 2016) (Ge et al. 2019), auger/screw shaped drills (Nagaoka et al. 2008) (Fujiwara et al. 2018) (Tadami et al. 2018), granular fluidization (Nagaoka et al. 2008), soft-rigid hybrid actuators (Zhang, Wang, et al. 2020), shape memory alloys (Kim et al. 2006) (Chatterjee, Niiyama, and Kawahara 2017), magnetically (Saga and Nakamura 2004) (Joyee and Pan 2019), compliant modular mesh (Kandhari et al. 2018), hydraulically (Xavier, Fleming, and Yong 2019), and via voice coil (Nemitz et al. 2016). These actuation principles along with their corresponding motion mechanisms, actuator technology, and control strategy can be seen in Table 1-1. Almost all these actuation principles generate motion with contraction, expansion, or torsional motion caused by stimuli such as light, heat, and applied electric and magnetic field (El-Atab et al. 2020). Soft robots are currently being utilized for the creation of soft grippers, which have proved highly effective at grabbing irregular or fragile items, the creation of flexible exosuits to enhance human

strength, biomedical surgical invasive tool manufacturing, and the manufacturing of biomimetic robots, which is the focus of this research.

Researchers have already found methods to create soft earthworm robots that utilize the principles of peristaltic movement to send “waves” of pneumatic actuations through the body of the robot, which allows for a crawling type of locomotion. The robots can do tasks as complex as climb 90 degrees pipes, which has many applications in the fields of infrastructural pipe inspection. Other applications of these robots include various military uses in the way of tunnel burrowing and reconnaissance, search and rescue missions for those trapped under avalanches, gastrointestinal tract inspection, and more.

The industry of soft robotics is not without its issues, however. Many challenges are introduced when working with soft materials such as silicone or rubber, and when actuation methods such as pneumatic tubes restrict the ability to create untethered, as well as more complex locomotion. Current research in the field of biomimetic soft earthworm robots has shown that soft materials can be slow and cumbersome to manufacture, and that designs cannot easily allow for a truly autonomous soft earthworm without seriously compromising the robots size and functionality. The idea of a soft earthworm robot that can move autonomously without wires or pneumatic tubes attached seems just within reach however and will greatly increase the applications and the efficacy of this design.

An answer to this roadblock may lie within a different, largely unexplored method of actuation – artificial fiber muscles. These muscles can be produced with very low-cost materials such as fishing line or sewing thread. They function by first being tightly coiled, and secondly having heat introduced to these coils. This heat can be from ambient temperature, a heat gun, or from interwoven metal wire with an electric current passed through it. When heat is introduced

these fibers contract in the axial direction and expand in the radial direction, which can allow for simple linear actuation. Not only are they highly cost effective, but they produce very respectable force and displacement, allowing for contraction up to 49%, and force generation 100 times higher than that of a human muscle of the same length and weight. Creating bundles of these muscles can allow for powerful actuation in a small area.

Using these artificial muscles within the context of a soft earthworm could allow for a truly autonomous and untethered design. If a soft material shell is used to house the artificial muscles along with an onboard power source and a microcontroller, then these robots could be the first of their kind to allow for cheap, easy to manufacture designs that still maintain a manageable size.

A more traditional option to manufacture this soft silicone shell would be to fasten the inner mechanisms within a hand poured silicone shell. This would require first the manufacturing of a mold – most likely out of a 3D printed material to allow for easy adjustments to be made. The silicone can then be hand-poured into the mold and allowed to cure before removing the finished silicone shell from the mold. The inner mechanisms – the artificial muscles, the microcontroller device, and the onboard power source – would then need to be attached to end caps within the silicone shell with epoxy/super glue. A faster method which would also allow for highly repeatable and larger-scale production would be to utilize a printer that can print with silicone. This would alleviate the time-consuming step of hand-pouring the silicone – which can also allow more room for human error.

The 3D printing industry has begun to produce commercially made 3D printers capable of printing soft silicone materials. One such printer is the Hyrel 3D Hydra 16A. This printer features 5 modular print head slots that allow for high resolution printing with plug-and-play

functionality, meaning that print heads can easily be changed in and out. The printer can be used in tandem with traditional "hard" filament printheads to create hybrid structures containing multiple materials to allow for easier production of biomimetic soft robots such as soft earthworms.

Understanding what has been done in the current literature is an important step in identifying what can be done to introduce some innovation. Table 1-1 aims to show what technologies already exist in the field of soft earthworm robots in a concise way, in an effort to help examine what new technologies can be deployed.

Actuation Principle	Motion Mechanism	Actuator Technology	Control Strategy
Servo-Driven Flexible Plates	Peristalsis	Servo-actuated flexible plates (Hayato, Takeshi, and Nakamura 2008)	Robot can be driven and turned via expansion/contraction of opposing flexible plates with small servo motors
Fully Soft-Bodied Pneumatically Driven	Soft Body Peristalsis	Chambers of silicone inflated/deflated (Heung, Chiu, and Li 2016)	Robot is connected to a compressor with hoses – each of the sections can be individually inflated and deflated to allow for peristaltic movement
Digging Auger Earthworm Robot	Peristalsis	Contracted/expanded electrically (Fujiwara et al. 2018) (Tadami et al. 2018)	Propulsion units contracted/expanded to produce peristaltic movement, forcing the auger into the digging medium
Burrowing Screw Robot	Screw Drilling	Electrically driven contra-rotor screw (Nagaoka et al. 2008)	Robot is put nose-down into digging medium (lunar regolith) and burrows straight down without turning capabilities
Tip-Extension with Granular Fluidization	Burrowing	Air-induced fluidization with tip-extension (Naclerio et al. 2018)	Digging medium (sand) is fluidized with air from a compressor. The fluidized sand allows for low resistance when burrowing tip first

Soft-Rigid Hybrid Actuator	Multidirectional Bending	Pneumatically driven internal chambers/electrically driven electrode (Zhang, Wang, et al. 2020)	a. Voltage controlled mode for minute adjustments b. Pressure controlled for higher output force and coarse adjustments
Single Pneumatically Driven Robot with Active Surface Gripping Sections	Peristalsis	Single, accordion like soft pneumatic middle section (Ge et al. 2019)	A posterior and anterior segment anchor in a staggered pattern to allow for a soft silicone central driving unit to produce peristaltic motion with simplistic actuation
Shape Memory Alloy Actuation	Peristalsis	Shape memory alloy spring driven linear actuation (Kim et al. 2006)	On/Off signal via a wireless communication device interfacing through an onboard transmitter
Permanent Magnetic Actuation	Inchworm-Like Crawling	Permanent posterior and anterior magnets (Joyee and Pan 2019)	Sequential magnetic force actuation in anterior and posterior legs of the robot to create a push-pull crawling movement
Permanent Water-Based Magnetic Actuation	Peristalsis	Water-based magnetic fluid that changes its viscosity when magnetized (Saga and Nakamura 2004)	Segments are made of natural rubber tube and filled with water-based magnetic fluid that can be actuated with an external wireless magnetic field
Compliant Modular Mesh Worm Robot with Steering	Peristalsis	12 small actuator motors (Kandhari et al. 2018)	2 small electric actuator motors in each segment bend the flexible tubes or rods that make up the outer shell in a wave-like propagation, while small linear springs return each segment to its initial state
Hydraulic Fiber-Reinforced Actuation	Peristalsis	Fiber-reinforced extending, contracting, bending, and twisting actuators (Xavier, Fleming, and Yong 2019)	Hydraulic fluid is connected to the actuators with small hoses to allow for complex motion that is safer for human interface in biomedical applications such as steerable catheters or endoscopes
Voice Coil Modular Actuation	Peristalsis	Electromagnetic voice coils encompassed in flexible membranes (Nemitz et al. 2016)	1 voice coil is present in each elastomeric body segment, which can act in both directions – shortening and lengthening the segment for movement
Hydrostatic Skeleton with Shape Memory Alloys	Peristalsis	Shape memory alloy springs	Each soft hydrostatic segment is pressured by the axially-arranged shape

		(Chatterjee, Niiyama, and Kawahara 2017)	memory alloys to create friction and produce peristaltic movement on flat ground

Table 1-1: Overview of Existing Earthworm Robot Actuation Principles

CHAPTER 2
LITERATURE REVIEW

Zoomorphic robots are nothing new in the overarching field of robotics and automation. Humans have used nature as a reference when creating and innovating for as long as they've been on Earth. In some cases, this inspiration is very apparent. In the field of soft and flexible robotics, it can be seen very clearly in robots that closely resemble octopus tentacles and earthworms. There are also many anthropomorphic robots that closely resemble human hands and fingers that can do tasks that many traditional "hard" robots struggle with – such as grabbing fragile or irregular things with consistency and delicacy. The focus of this research however is to shed light specifically on those robots that look and function like earthworms. These soft robotic earthworms offer unique advantages with their shape, functionality, and flexibility. They have a plethora of applications including but not limited to military use, gastrointestinal tract inspection, pipe inspection, search and rescue, and more. In order to delve into this topic, the literature that has already been written about these soft earthworm robots must be reviewed.

The first hurdle in producing these earthworm robots is to determine the best way to mimic the movement of an earthworm utilizing flexible or soft segments. Earthworms move via peristaltic crawling, meaning they move by wavelike muscular contractions much in the same way as the esophagus and intestines move material through the body. Earthworms' bodies are partitioned into numerous segments that are divided by septa and a coelom that contains the animal's gastrointestinal tract as well as nerve circuits. These nerve circuits send signals to the two sets of muscles within the worm – the outer circular muscles and the inner longitudinal muscles. The outer circular muscles actuate in a radial manner. They cause their respective segment to become thinner, extending the segment in the axial direction. The longitudinal

muscles actuate in the axial direction, causing their respective segment to become thicker, shrinking it in the axial direction.

For an earthworm to move, it needs to actuate these muscle groups in a peristaltic motion starting from the front of the animal moving to the rear. It does this by first contracting the longitudinal muscles in the anterior segments of its body. By doing this and thickening its anterior segments, friction between said segments and the ground is increased, which causes these segments to remain in contact with the surface. This contraction propagates to its posterior, and the animal's rear segments are pulled in the direction of movement. The anterior segments then extend in the axial direction using the circular outer muscles. Friction is reduced in these thinner sections, and they move smoothly in the direction of movement. These extended segments continually propagate towards the posterior, while forward segments are pushed in the direction of movement.

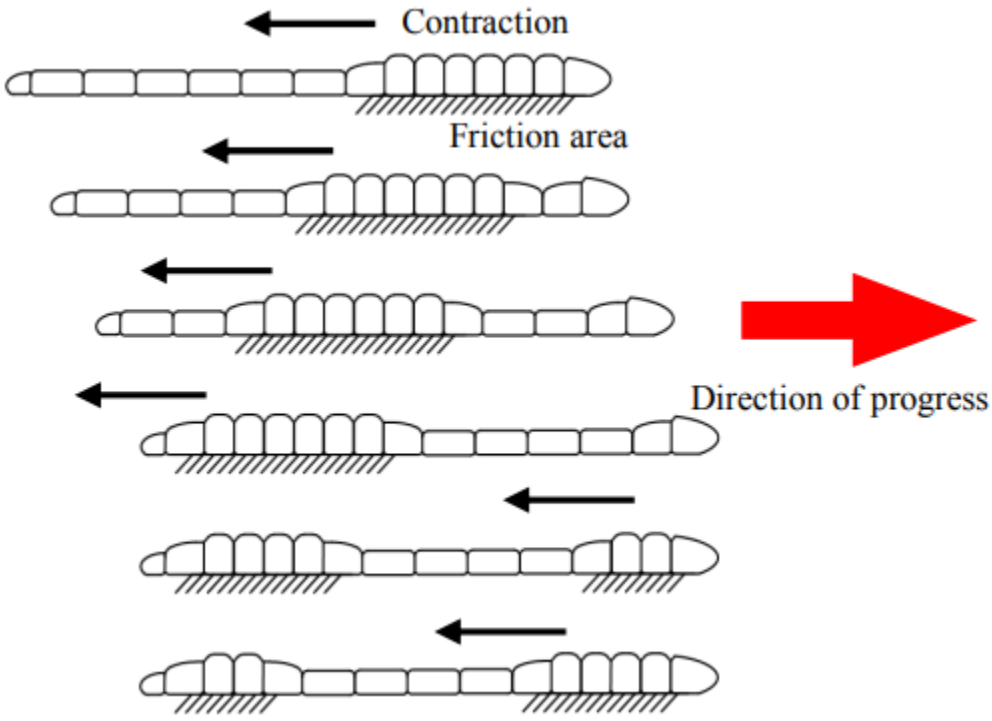

Figure 2-1: Peristaltic Locomotion Pattern of an Earthworm (Hayato, Takeshi, and Nakamura 2008)

Researchers at Chuo University in Hachioji, Japan, observed this motion in biological earthworms by sectioning off 6 equal sized segments in the worm and filming the worm move. By tracking the location of each segment, the researchers could determine how long each peristaltic period was and how fast the animal could move on a flat surface. (Hayato, Takeshi, and Nakamura 2008)

The advantages robotic peristaltic movement were obvious from studying how earthworms move. This type of movement requires less space than a bipedal or wheel-based motion, and it provides excellent stability on irregular ground and inside narrow pipes or tunnels. This type of movement is very suitable for exploration, rescue, endoscopic applications, and more. To implement this kind of movement robotically, research teams could not use traditional "hard" robotic units. This is where soft and flexible robotics has the advantage.

The research team at Chuo University were able to make a rudimentary earthworm robot with flexible joints that could do basic tasks. They found that by creating 7 flexible units, each containing 2 small servo motors that shifted flexible plates on the outside of the robot, they could emulate simple tasks such as slowly peristaltically crawling, turning, and climbing through tubes.

Manufacturing the prototype involved creating several contraction-extension units – referred to as CEs – and controlling them using a PIC (peripheral interface controller). The CEs are connected axially and in segments of at least 3 to allow for peristaltic locomotion. Within each CE is a servomotor and a crank. The crank converts the servomotors rotational movement into linear movement. A rubber sheet is attached to each belt within the CE segment to increase friction with the surface. The rotational angle of the servomotor is used to generate locomotion and is controlled by a PWM (pulse-width modulation) timer which is output from the PIC (Takashi, Tomohide, and and Yoichi 2006). Their prototype can be seen in Figure 2-2.

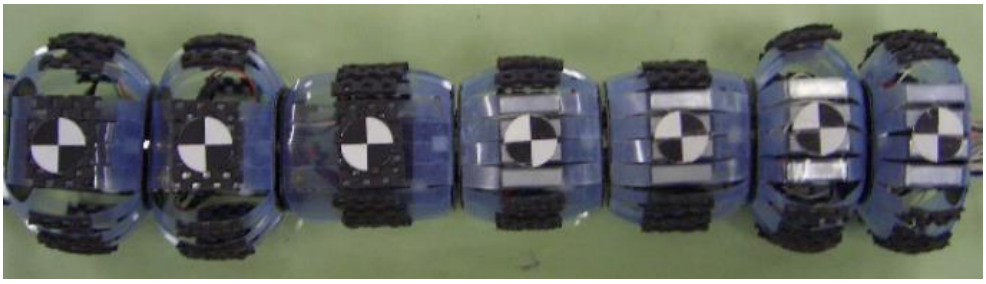

Figure 2-2: Chuo University Peristaltic Crawling Robot (Hayato, Takeshi, and Nakamura 2008)

The team gathered data on the robot's performance by recording its motion with a camera and tracking each unit's position and the time it took to reach its destination. They found that it was able to effectively crawl and turn on flat ground as well as crawl through tubes that had 90 degree turns straight up – albeit very slowly.

In 2011, two previous researchers, as well as 5 other team members set out to improve on their previous research. They created a robot that can use sensors to produce a 3D model of the inside of a pipe by crawling through it and recording data on the pipe using an omni-directional rangefinder (Yamashita et al. 2011).

Pipe inspection is one of the main advantages a soft robotic earthworm would have over any other type of robot in the field. By utilizing the flexibility and geometry of the robot, these researchers found a way to remedy a problem in a new way with a new technology. Gas and water pipes are found anywhere there is infrastructure, and they are crucial to everyday life. It is valuable information to know whether these pipes have developed cracks or other internal damages due to age that would otherwise be invisible to human eyes. Efforts have been made in the past to develop robots that can scan and image these pipes for damage, but they are slow because they use a camera to take pictures and must stop frequently to record images. A more

effective method would be to use an omni-directional vision sensor that can take images in 360 degrees which passively measures points within the pipe to create a 3D image.

Researchers built upon the earthworm robot in Figure 2-2 by adding a passive omni-directional vision sensor. The robot was able to image the defect in the pipe to an accuracy of 1 mm and produce a 3D image as seen in Figure 2-3 below, proving that the proposed method of image acquisition and analysis was effective and highly precise. Their research provides a valuable blueprint for how to integrate sensors into a prototype to collect valuable data in the field.

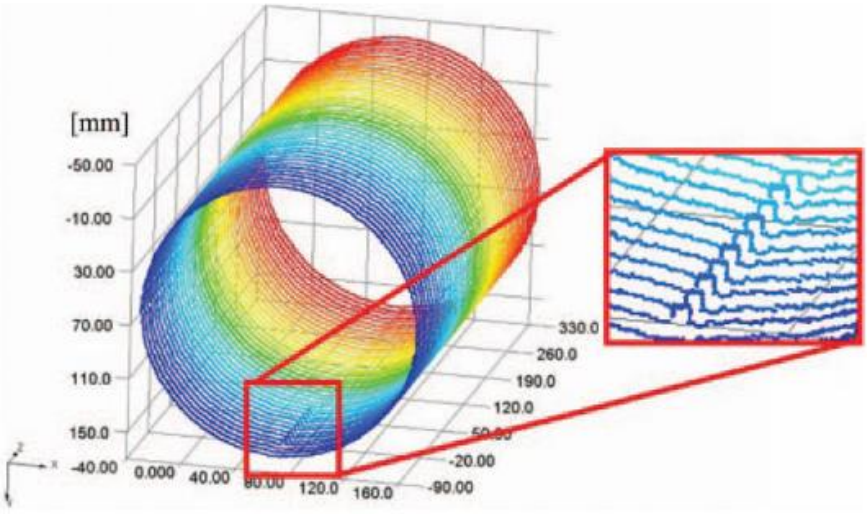

Figure 2-3: Result of 3D Shape Measurement (Yamashita et al. 2011)

One potential application of earthworm robots comes in the form of gastrointestinal (GI) tract inspection using a softer version of said robot. When creating any kind of robot or apparatus that is to be inserted into the human body it is extremely important that it created out of safe material and is a size that won't cause bodily harm. Soft is one of the key words in soft robotics, and it implies the use of highly elastic materials e.g., silicone rubber that can be used to create

actuators and replace rigid bodies found in traditional hard robotics. These soft actuators and bodies work together to generate movement, in this case the zoomorphic movement of a biological earthworm, without the need for complex structure, all while remaining intrinsically safe for human robot interaction. To create a robot that can inspect the gastrointestinal tract, researchers in Qingdao, China utilized a fully soft bodied approach to prototype an earthworm robot capable of crawling around a colon to check for digestive diseases (Heung, Chiu, and Li 2016).

The most conventional and commonly utilized method of gastrointestinal tract inspection is through the use of flexible endoscopes. Doctors insert these endoscopes into the colon through the anus and must manually rotate and push them through the organ. When they come up on turns, they must manually twist the device which always carries the risk of puncturing the colon. In addition to this drawback, this procedure also calls for sedation to the patient. This isn't the only option currently available, however - capsule endoscopes containing a micro camera, power module, antenna, and image transmission module can also be used. These capsules are very useful in looking at the small intestine section of the gastrointestinal tract due to how difficult it is to reach. However, the device cannot be steered, can get stuck in the small intestines if tumors are present, does not provide accurate information on the exact whereabouts of abnormalities are, cannot repeatedly inspect a suspected area, and has a low coverage rate in larger areas such as the stomach and colon.

To solve the drawbacks of the existing gastrointestinal tract inspection devices, the Qingdao researchers looked to a soft robotic earthworm. The earthworm contained 3 sections – 2 expanding sections and 1 extending middle section that could also bend to steer the robot. To achieve the earthworm-like movement, the robot first anchors its rear section to its environment,

and the other two sections relax. Then, the middle section extends and bends according to the direction it needs to go. Once the middle section is fully extended/bent with the rear section anchored in place, the front section expands and anchors to its environment as well. Finally, the rear section relaxes and the middle section contracts, pulling the robot in the desired direction of locomotion. To achieve this motion, the robot utilizes pneumatics to expand air chambers within each section of its silicone rubber structure.

The robot is made with a single piece of hyper elastic material – in this case silicone rubber – with 3 separate chambers as mentioned previously. Each chamber is wrapped in fiber to constrain it and force it to actuate in a certain desired manner. The end chambers have the same wrapping because their function is the same – the fiber runs along the chambers lengthwise causing them to inflate radially. The central section has fiber wrapping that runs perpendicular to the lengthwise wrapping in the end sections and in a double helix pattern. This forces the central section to inflate longitudinally. The prototype is made using virtual lost wax casting method, which is done by 3D mold printing, mixing silicone rubber and filling the mold, curing, and demolding (Marchese, Katzschmann, and Rus 2015). The silicone used is SmoothOn^{TM} EcoFlex^{TM} 00-30.

Experiments were first done in a PVC tube. 3 prototypes of varying section lengths (seen in Figure 2-4) were inserted into the PVC tube, and their crawling speed was measured at 0 degrees and then again at varying angles. Through this experiment, it was found that speed was directly proportional to the length of the middle section. The researchers also tested the robot's performance when a payload was attached to the rear of it to simulate drag. The velocity of the prototype tested was unchanged at a payload weight of 0.12 kg, and the earthworm robot stopped completely when the payload weight was 0.48 kg. The bending functionality of the robot was

also tested, and it was found that the maximum bending angle was greater than 90 degrees in all direction, making it well suited for a 3D tubular environment.

Figure 2-4: Prototypes of the soft earthworm robot: (a) Version 1; (b) Version 2; (c) Version 3 (Heung, Chiu, and Li 2016)

Another unique function that earthworm robots provide is their ability to burrow in soft ground much like their biological counterparts. Researchers in Seoul, South Korea have researched this application and have used a similar design to the previously mentioned one that was created for gastrointestinal tract inspection (Liu et al. 2019). Their robot, which has an extensile actuator in its center, and two contractile anchor actuators on either end, also utilizes pneumatically driven soft chambers that can be actuated with servos. For their robot to effectively burrow through the earth, they had to ensure that it could get adequate traction and be able to fight through high amounts of drag without stopping. To do this, the researchers looked to the biological counterpart and took note of the setae on the sides of its body. These setae are small bristles on the sides of the animal that help anchor and control the animal in the soil. They hold the worm firmly in place while other parts of its body protrude forward. To mimic this, a Kirigami-like skin was developed. Kirigami is a variation of origami that allows for cutting of

the paper rather than just solely folding the paper. This type of pattern allows for better traction and payload carrying abilities.

The Kirigami skin is made of silicone plastic (SmoothOn™ DragonSkin10™ NV) which allows for the robot to maintain its flexibility. The Kirigami pattern is featured on the two anchoring sections on either end of the robot, and it features repeating overlapping patterns that can be flexed up and down to allow for contraction. The middle extensile section of the robot also features an inner layer of silicone-plastic, but unlike the contractile sections of the robot, it also features a Kevlar thread double helical outer layer to allow ruggedness and rigidity. The 3 sections are connected via a press-fit rings, which allows flexible tygon tubes to be routed inside each actuator. The tygon tubes control each actuator via 5-port solenoid valves which are connected to an Arduino Due controller. The robot also has a conical nose on the front end to allow it to more easily reduce the resistance force acting opposite to its direction of motion. The Kirigami skin itself is manufactured out of a polyester plastic sheet. A 100 mm by 100 mm square of polyester plastic is coated with the silicone plastic and after the silicone is cured a 1mm membrane of silicone plastic is left atop the skin. The Kirigami shape is then partially laser cut at low power and rolled into a hollow cylinder which is 20mm in diameter.

Extensive testing was done on this Kirigami skin to ensure that it would be beneficial to the underground peristaltic crawling of the robot. One of the main reasons the pattern was chosen was that it stretches easily in the vertical direction but does not stretch in the horizontal direction.

The performance of their robot in their experimental procedures was highly dependent on the robot's ability to effectively anchor itself with its contractile actuators. To prove their work with the Kirigami pattern was effective, the robot needed to be able to pull a payload through soil at a speed that was deemed acceptable. Drag force was measured with a uniaxial testing

machine, and a relation between drag force and hole diameter was evaluated. This relationship was observed in 3 conditions – with a bare robot (no Kirigami skin), with a plastic Kirigami skinned robot, and with a silicone-plastic Kirigami skinned robot. The 3 different conditions can be seen in Figure 2-5. The bare robot yielded the lowest maximum drag force, the plastic Kirigami skinned robot yielded the second lowest maximum drag force, and the silicone plastic Kirigami skinned robot yielded the highest maximum drag force. This is likely because the silicone plastic Kirigami skin was thicker and more rigid than its plastic counterpart, which allows for better traction and higher drag force.

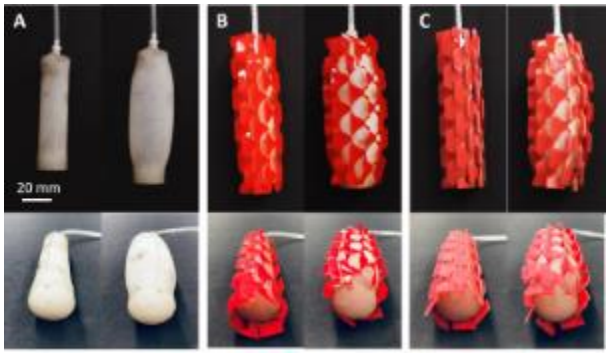

Figure 2-5: Different drag force test conditions: (a) No Kirigami skin; (b) Plastic Kirigami skin; (c) Silicone-Plastic Kirigami skin (Liu et al. 2019)

One of the most coveted characteristics of biological earthworms to implement into a soft robot is their stretchability. The issue that many researchers run into, however, is that when implementing sensors and joints into their robots, they lose a percentage of said robot's stretchability. A team of researchers based out of Atlanta, Georgia set out to design an earthworm robot that could incorporate tough, reliable, and most importantly stretchable sensors that could be incorporated into a truly soft design.

Many types of sensors have already been developed for this type of earthworm project, including resistive, piezoresistive, capacitive, and optical sensors. They are typically

encapsulated into silicone or rubbery materials to protect them and to still maintain a degree of elasticity, but by doing so the robot loses its ability for 100% stretchability. Recent research has been done to combat this issue, but none of them have demonstrated complete integration and wireless communication abilities. The team of Atlanta researchers wanted to not only have their robot maintain 100% stretchability, but also demonstrate the ability to communicate data over long range wirelessly (Goldoni et al. 2020).

The strain sensors would need to be able to be integrated into the soft outer skin of the robot. This was done via two types of silicone elastomers which are integrated in a tight sensor-to-body fashion to allow for high accuracy and sensitivity. The outer strain sensor communicates with the wireless electronic unit via nanomembrane interconnectors that are highly stretchable and bendable due to their miniaturized printed manufacturing. This wireless electronic unit is housed within the robot in a 3D printed plastic case to protect it from external stresses during locomotion. It can interface long range with Bluetooth technology, making it great for long range manually controllable applications. These technologies can be seen in Figure 2-6.

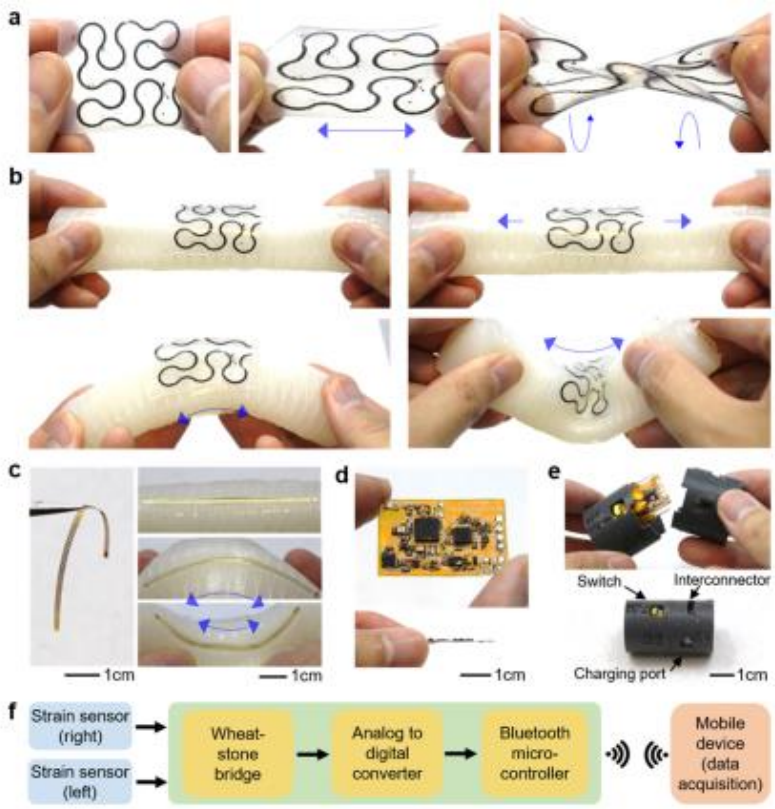

Figure 2-6: Overview of a wireless strain sensing system integrated with a segment of a soft earthworm robot. (a) Nanocomposite strain sensor at upstretched (left), stretched horizontally (middle), and twisted by fingers (right). (b) Sensor-embedded robotic segment at rest (top left), uniaxially stretched (top right), outward bending (bottom left), and inward bending (bottom right). (c) Nanomembrane stretchable interconnectors than can endure multimodal stretching and bending on a soft robotic segment without mechanical fracture. (d) Photos of a miniaturized wireless circuit showing the top view of the entire circuit (top) and side view (bottom). (e) 3D-printed plastic case that incorporates the wireless circuit with dedicated apertures providing physical access. (f) Flowchart showing the signal path from strain sensors to the mobile device. (Goldoni et al. 2020)

To create these soft strain sensors, the team utilized screen printing technology, which allows for high scalability and low cost. The strain sensors are made of conductive carbon nanotubes, which still allow for full stretchability. The sensor features an open mesh serpentine design which is based on a previous work of the research team that allows optimal stretchability parameters with a radius of curvature of 270 degrees and a width of 1 mm (Figure 2-6a). These sensors, after being screen printed onto the soft material on both sides of the robot, are then

connected to nanomembrane interconnectors (Figure 2-6c) which communicate their data with the wireless electronic system (Figure 2-6e).

Experiments were done to test the reliability, sensitivity and accuracy of the sensors. First, the sensor was held at a fixed strain for 20 seconds following 10% stretching. The results showed that the sensor allowed for excellent stability in terms of resistance when kept at a constant strain up until around 80% strain. Another test was then done which called for cyclic stretching from 0% to 100% uniaxial strain up to 500 times to ensure the reliability of the sensors. The strain sensors maintained their sensitivity throughout the test showing a marginal drift in their values throughout each cycle. Tensile stretching tests were also done at two different speeds – 50 mm/min and 200 mm/min. The test showed typical viscoelastic behavior of the sensor at high speed and the resistance change during loading and unloading cycles were nearly identical. Atop this, the carbon nanotubes were minimally influenced by the rearrangement effect. Tests were also done to check the accuracy and sensitivity of the sensors when manually bent, squeezed, elongated, compressed, and vibrated. The embedded sensors demonstrated their ability to detect external and internal stimuli with a high degree of sensitivity which mimic real world situations that the robot will experience.

This research showed that sensors and nanomembrane interconnectors can be seamlessly integrated into a soft robotic earthworm without any need to sacrifice stretchability. The team managed to keep a stretchability of 100% with a gauge factor of 38.7 all while maintaining a high degree of reliability, sensitivity, and accuracy. In addition, their robot can wirelessly interface over a long range due to Bluetooth technology, which is something that had not yet been utilized for a soft robot earthworm.

Drilling is one of the main applications of earthworm robots. Their biological counterparts are very effective at it, and peristaltic motion excels when there are more surfaces to touch and more friction that can be produced. There is something that robotic earthworms have an advantage in over their biological counterparts – they can burrow underwater. This was the basis of a study done by a team of Japanese researchers (Liu et al. 2019; Isaka et al. 2019). The idea was to create a robust earthworm robot that can navigate around the seafloor and excavate mineral resources found at the bottom of the ocean.

To do this, researchers came up with a design like those seen prior, but with an auger integrated within the crawling subunits. The locomotion of the robot works similarly to other earthworm robot designs that feature pneumatically driven segments that mimic the wavelike peristaltic movements of biological earthworms. To integrate a digging mechanism, an excavation unit was designed that features a corkscrew-like shaft that moves dirt or soil up through the robot and stores it within the casing pipe to be retrieved by researchers. The design can be seen in Figures 2-7 and 2-8.

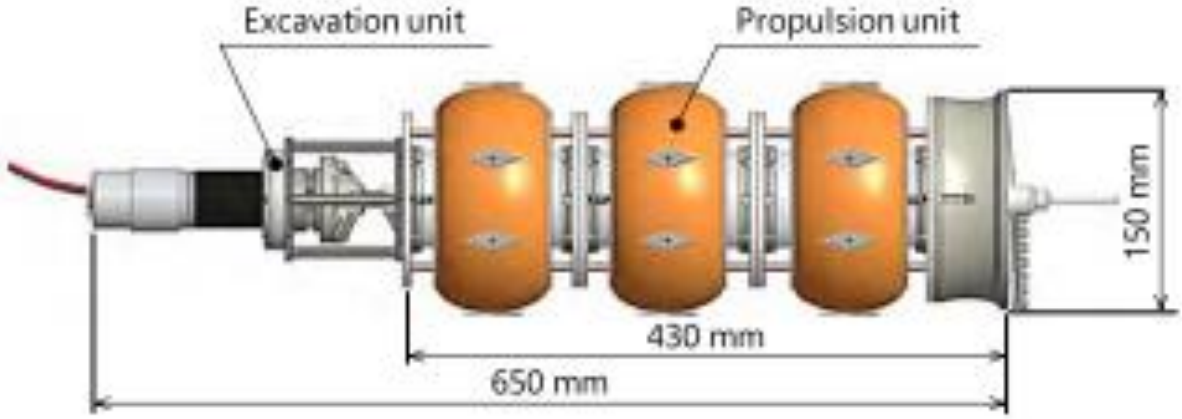

Figure 2-7: SEAVO II Underwater Drilling Earthworm Robot (Isaka et al. 2019)

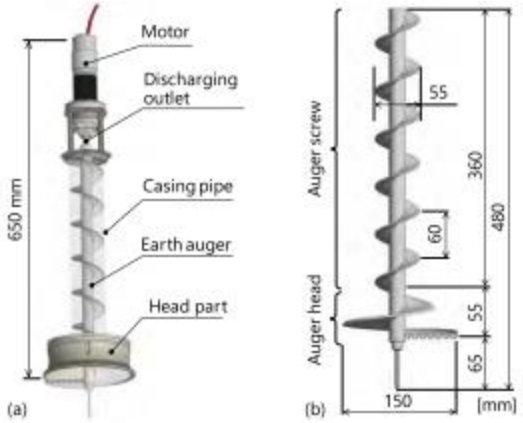

Figure 2-8: (a) Schematic Diagram of the Excavation Unit; (b) Schematic Diagram of the Earth Auger (Isaka et al. 2019)

To collect samples, the motor turns on when the robot is in position on the seafloor and the auger begins to spin. The earthworm robot then begins to expand and contract its segments in a wavelike pattern to move it forward and force the dirt or soil into the casing pipe. To ensure the design was functional, the team designed experiments in tanks of simulated ground submerged in water. They first tested only the excavation unit to determine the correct motor speed and crawling speed, as well as observed differences between dry and underwater ground drilling. The team then did a full test with the SEAVO II robot in the test tank. The robot excavated 430 mm in 4686 seconds.

The SEAVO II also has a counterpart with a flexible auger supported at both ends that is designed to collect regolith samples from the surface of the moon. This robot, called the LEAVO, and looks very similar to the previously mentioned design. It features an auger system running through the middle of a 3-segment propulsion unit. The main difference in the LEAVO is the flexibility of its auger component while remaining dustproof, and it's both-ends supported type auger configuration (Fujiwara et al. 2018).

The research team had to ensure that the robot could excavate holes to collect regolith samples at a particular layer. They determined that it was necessary to implement a degree of flexibility within the robot to allow it to reach the desired layer by changing excavation direction. A curving system was designed by incorporating universal joints in the auger to allow it to be passively bent when the propulsion units were activated in certain configurations. Two O-rings were arranged on the inner wall of the front disk of the excavation unit to ensure dust did not infiltrate the prototype. These disks fill the interspace between the disk and casing pipe via their elastic deformation. The excavation unit can be seen in Figure 2-9.

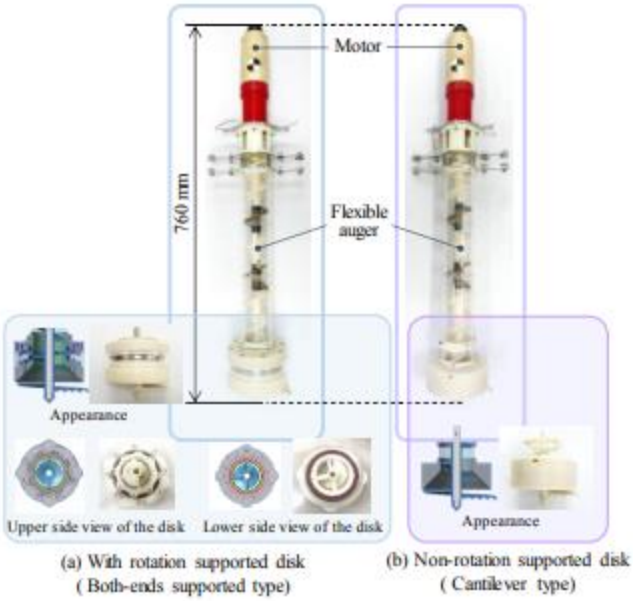

Figure 2-9: Flexible Auger Excavation Units (Fujiwara et al. 2018)

The two excavation units seen in Figure 2-9 have one difference in how they are supported rotationally. Excavation unit (a) features a disc at the drilling end of the unit that supports it rotationally (both-ends supported type), whereas unit (b) is a more traditional design that features no support disk (cantilever type). The research team wanted to see if the both-ends supported design would help lower runout at the auger tip and if it would produce better drilling results than the cantilever design. Two experiments were designed to test and compare the two designs. First, the two designs were mounted above a camera with a tracking point being attached to the end of the auger tip. The camera tracked and plotted the point onto a graph and showed very clearly that the both-ends supported type of support system drastically reduced the axis runout. The second experiment was designed to compare the hole diameters and torque generated by the two designs. The two designs – both-ends supported type and cantilever type - drilled a hole over the course of 720 seconds. Torque and hole diameter was measured for each. The both-ends supported type yielded a driving torque of 2.2 N m and drilled a hole that was

smaller and 1 mm larger than the target diameter. The cantilever type yielded a driving torque of 0.2 N m and drilled a larger hole that was 9 mm larger than the target diameter.

The both-ends supported flexible auger proved to be the better choice for the purpose of lunar regolith sample collecting with its low axial runout, high driving torque, and more accurate hole diameter.

Manufacturing methods of these various designs vary, however there are a few established methods that can be used for soft-bodied robots – which are the focus of this research. Three major fabrication techniques are touched on in a 2015 research paper on the subject of pneumatically-driven soft fluidic elastomer robots (Marchese, Katzschmann, and Rus 2015) which is relevant to the subject of soft earthworm robotics. The first of these is lamination casting with heterogeneous embeddings. This method involves casting the outer layers of the robot separately using soft lithography techniques to inlay pneumatic channel structures. These outer layers are then laminated together with a constraint layer to form the actuator. Air supply lines can then be fed into the actuation chambers.

The second method is called retractable pin casting. In short, this casting technique involves pouring a multi-stage mold around metal rods that can later be removed to create the cavities used for pneumatic actuation. This method allows for casting without lamination, which can help reduce ruptures and delamination of the layers.

The third and final method mentioned was briefly touched on previously and is called lost wax casting (Zhang, Zhu, et al. 2020). This involves several steps which can be seen in Figure 2-10. The steps are as follows: harder silicone rubber is poured into a mold which contains a 3D printed model of the wax core. The mold is removed, and the rubber mold is left inside the outer

mold. A rod or tube is laid into the cavity of the rubber mold, supported on both ends by the outer mold. The wax is heated until liquified. The assembly of the rubber mold and outer mold is heated to the same temperature as the wax. Using a syringe, the liquid wax is injected into the assembly. Uncured silicone rubber is poured into the assembled mold. Stiffer rubber is poured on top of the cured actuator to form a constraint layer. Cured actuator is removed from the mold. The wax core is melted out with and oven, and finally, silicone tubing is added and plugged using silicone sealant. The advantage this method has over the other two is the lack of delamination, and the allowance for more complex channel structures than what is offered with metal rods.

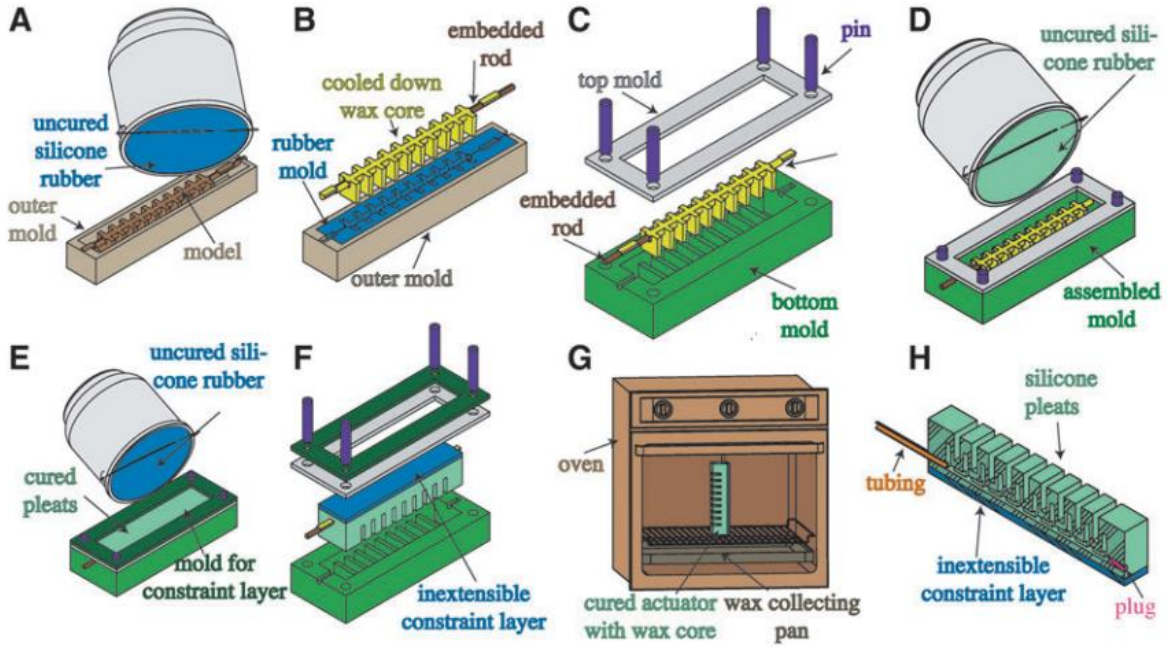

Figure 2-10: Fabrication process for the pleated actuator morphology: (A) pour and cure a rubber mold; (B) pour wax core with embedded supportive rod; (C) combine bottom mold, top mold, and wax core using pins; (D) pour rubber into assembled mold; (E) pour stiffer rubber on top of the cured actuator to form a constraint layer; (F) remove cured actuator from mold; (G) melt out wax core from the actuator using an oven; and (H) add silicone tubing and plug using silicone sealant (Marchese, Katzschmann, and Rus 2015)

One major area that has largely been untouched concerning its application in the field of soft earthworm robotics is low-cost artificial fiber muscles. These muscles can be developed with the use of nylon fishing line as well as sewing thread. They are developed simply by introducing tight twists into the fibers to create a coil that can contract and expand when introduced to heat to lift and push loads that are extremely efficient for their size and weight when compared to human muscles. In fact, these muscles can contract by up to 49% and lift loads 100 times heavier than what a human muscle of the same size, weight, and length can lift. They can generate up to 5.3 kilowatts of mechanical work per kilogram of muscle weight, akin to the work produced by a jet engine (Haines et al. 2014). The structures that can be produced by coiling nylon and sewing thread can be seen in Figure 2-11.

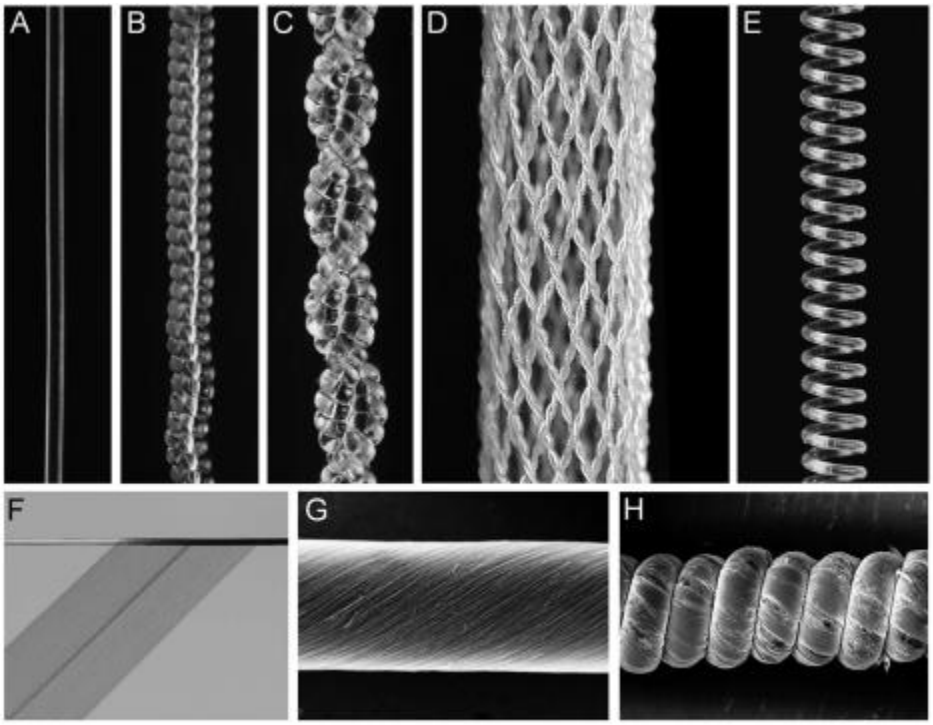

Figure 2-11: Muscle and precursor structures using nylon 6,6 monofilament sewing thread. Optical images of (A) a nontwisted 300-mm-diameter fiber; (B) the fiber of (A) after coiling by twist insertion; (C) a two-ply muscle formed from the coil in (B); (D) a braid formed from 32 two-ply, coiled, 102-mm-diameter fibers produced as in (C); (E) a 1.55-mm-diameter coil formed by inserting twist in the fiber of (A), coiling it around a mandrel, and then thermally annealing the structure; and (F) helically wrapping the fiber of (A) with a forest-drawn CNT sheet and scanning electron microscope images of a CNT-wrapped, 76-mm diameter (Haines et al. 2014)

These artificial muscles help alleviate many production concerns and can be made for extremely cheap. They demonstrate fast, scalable movement (which can be compounded further via bundling these fibers together), which produces non hysteric motion and a long life span. They are seeing some implementation already in the automotive industry and the home improvement industry, where they are being used to create window shudders that can automatically open and close depending on how much heat they receive. Their actuation method is very simple and can be induced by heated liquids, ambient air, heated/cooled air, and thin wiring with an electric current passed through it.

These artificial muscles solve some major problems posed by more “traditional” actuation methods in the field of soft robotic earthworms. For one, they are very inexpensive to manufacture, requiring only a simple coiling/wire integrating linear actuation system, and a length of thread or fishing line which only costs a matter of cents. Their shell can be molded out of silicone or 3D printed in a specific 3D printer made for soft materials. Another advantage this method offers is the ease of creating a self-contained robot. Because they do not need air hoses or large power cables, they can house a small battery pack on-board, allowing for autonomous and unrestricted movement. With a segment of coiled fiber contracting at the same time another segment expands, peristaltic movement can easily be replicated with these muscles. There are some limitations of this method, however. Their energy use is quite inefficient – wasting as much as 99% of energy to heat loss. The solution to this is to ensure that the muscle coils are tightly packed, and that the coiled wire used to heat them (if that is the desired method of heating) is at a consistent spacing throughout the muscle. Another issue lies in turning and steering the robot. This problem has not been very thoroughly researched yet, but there are emerging methods where the artificial muscles can be manufactured to produce torsional movement, which can allow for turning and steering.

This previous research has laid out the blueprint for how to manufacture and collect data for an earthworm robot, and what should be considered for future manufacturing techniques, experimental setups, and actuation principles. Many innovations have been made in the field of earthworm robotics, with researchers building on one another to continually improve previous designs, but it is also clear that there is still room for improvement. Various design choices have been changed and adjusted, all making their respective designs slightly better and more efficient at peristaltic crawling, burrowing, etc. These robots have fallen into their niche and will prove to

be invaluable in many fields – medicine, hole digging, pipe inspection, and more. To allow them to truly make waves in these industries, their viability must be proven experimentally, and they must allow for an economic advantage over more traditionally methods they are replacing or supplementing. One solution to this economic issue is the introduction of cheap, easy to manufacture fibrous driven soft earthworm robots. They solve many of the problems posed by their pneumatic counterparts and can enable true autonomy via an onboard power source.

CHAPTER 3

METHODOLOGY

Part 1: Fabricating Artificial Muscles

Naturally, the first step to devising a method of utilizing fibrous artificial muscles to drive a soft earthworm robot is to first fabricate the muscles themselves. The muscles are made via 4 stepper motors, a sliding linear carriage, and a linear actuator.

The material used for this setup is Eagle Claw™ nylon monofilament 80 lb-test fishing line with a diameter of 0.8mm. The fishing line is fed through a small ¼" cylindrical adapter and held in place with 2 set screws, ensuring not to overtighten the set screws to avoid the line snapping while twisting. The ¼" cylindrical adapter is fastened into a Thomson™ Industries Linear Quickslide™ System via two set screws. Another fishing line is used to fasten a deadweight – whose weight is proportional to the pound-test fishing line being used – and this deadweight is dangled from the edge of the table attached to the linear sliding system with an ultra-low friction pulley system. This setup can be seen in Figure 3-1.

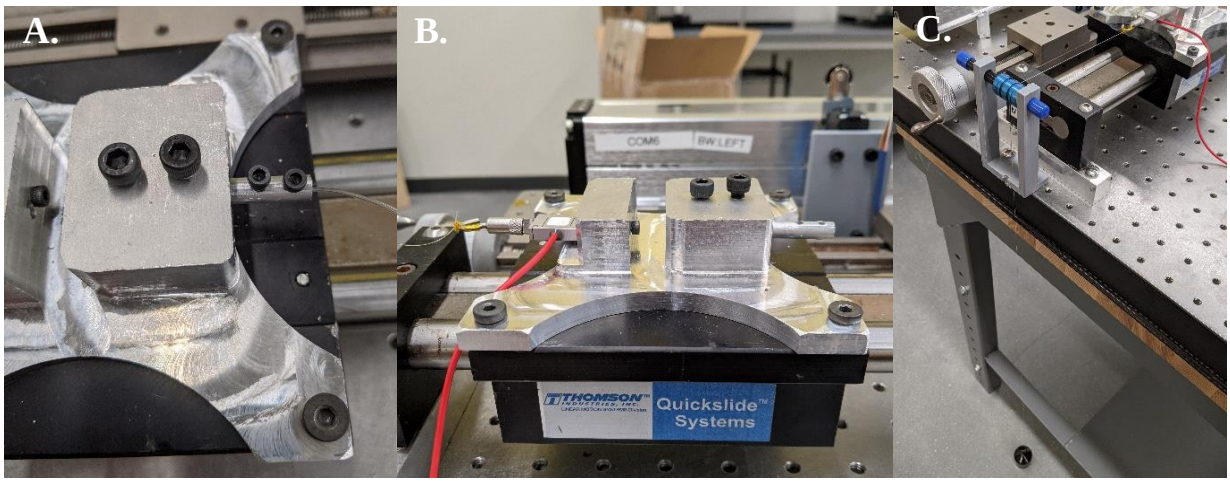

Figure 3-1: (a) Fastening of Fishing Line into ¼" Cylindrical Adapter, and Insertion of Cylindrical Adapter into Linear Sliding System (b) Linear Quickslide System (c) Low-Friction Pulley with Deadweight

The other end of the fishing line is then attached to a larger ½" cylindrical adapter, which is mounted to the motor shaft of an Autonics™ stepper motor. These motors are controlled by a PLC program that can be modified to allow for various RPMs. A control panel is used to manually control the rotation of the 4 stepper motors as well as the movement of the linear actuator. The stepper motor used for the initial twisting of the line is an Autonics™ A4K-M245 stepper motor labeled M2. The motor spins at a rate of 10,000 pulses per second. As the line twists and potential energy is introduced, the linear sliding system will begin to move, allowing for the line to shorten until it reaches a critical point where coiling begins. As soon as this begins, M2 is stopped to allow for the next step.

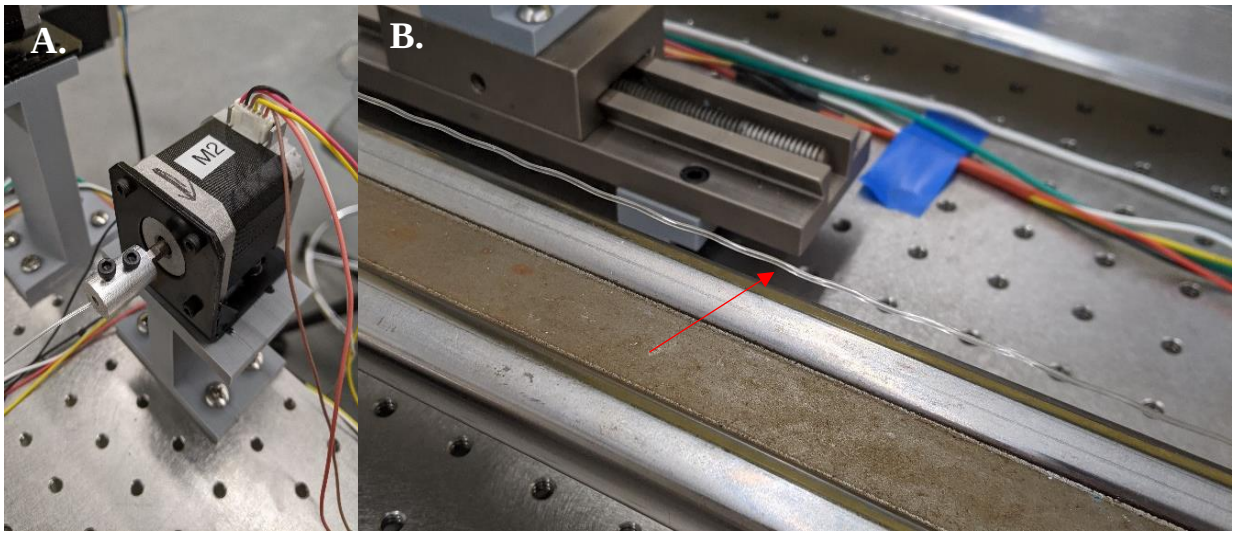

Figure 3-2: (a) The Fishing Line is Attached to M2 via a ½" Cylindrical Adapter (b) Twists are Introduced into the Fishing Line

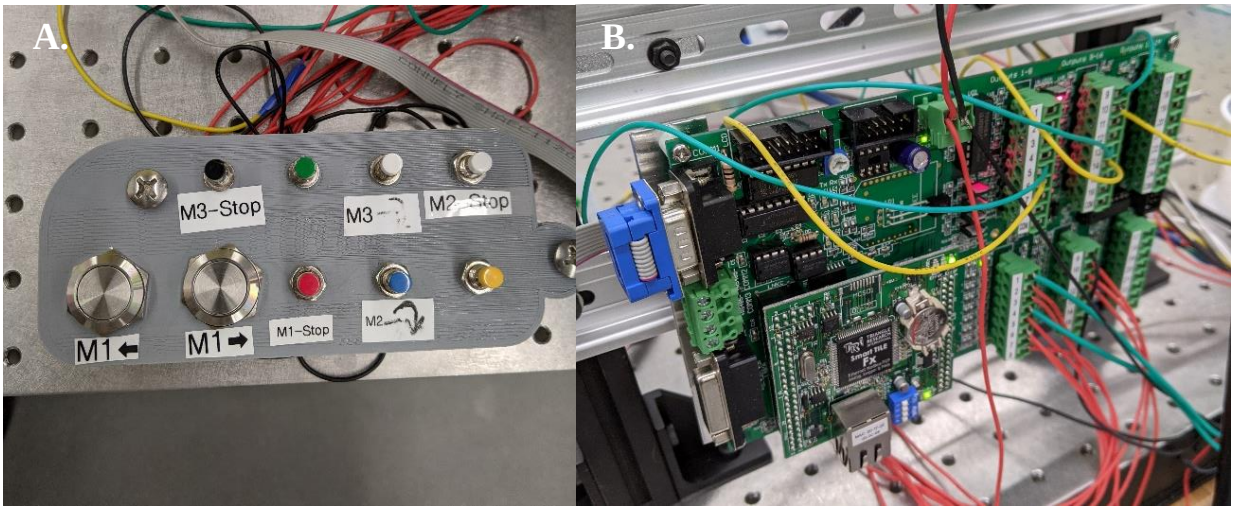

Figure 3-3: (a) The Manual Control Panel for the Motors/Linear Actuator (b) PLC for Controlling Motor/Linear Actuator Behavior

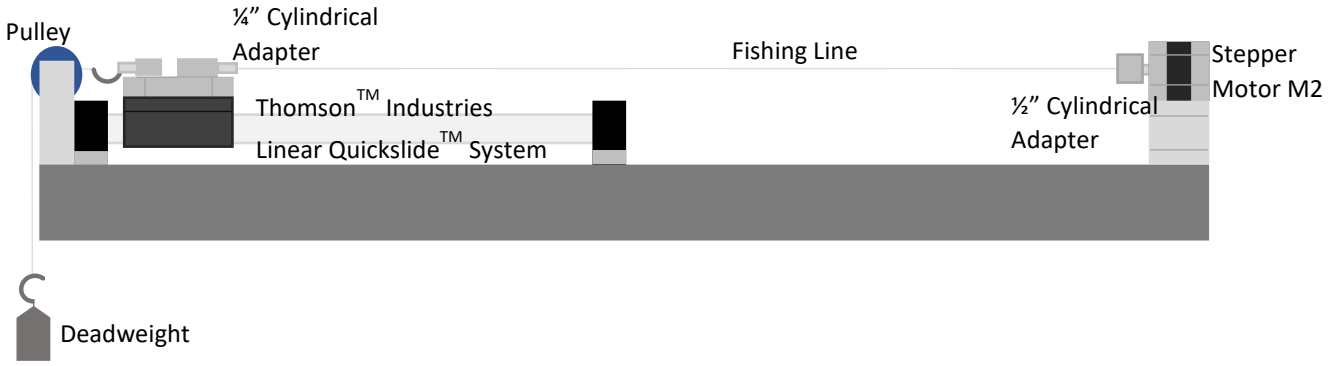

Figure 3-4: Line Twisting Setup

The fishing line is then transferred very carefully from the line twisting setup to wire wrapping setup with two AutonicsTM A4K-M243 stepper motors labelled M3. Tension must be kept on the line, or it will have the tendency to bunch up or have kinks introduced that can cause negative effects later in the process. A small nickel chromium wire with a diameter of 0.076mm is wrapped around the set screw of the right hand M3, and the two M3 motors (right and left) are turned on simultaneously with the Fuyu FSL80 linear actuator (M1) using the control panel. The stepper motors rotate at a speed of 4,000 pulses per second while the linear actuator moves at a speed of 0.5 in/sec. To ensure the conducting wire does not get bunched up within the feeding mechanism, a small 10g weight is attached to ensure that the wire stays taut. The wire is woven around the twisted line through this method, allowing for electricity to be induced through the wire, causing joule heating which allows for contraction, expansion, and torsion of the artificial muscle. The process must be closely monitored to ensure that the wire is woven evenly throughout the fishing line. If a section of wire becomes too close together, the heat produced in this segment can melt the fishing line.

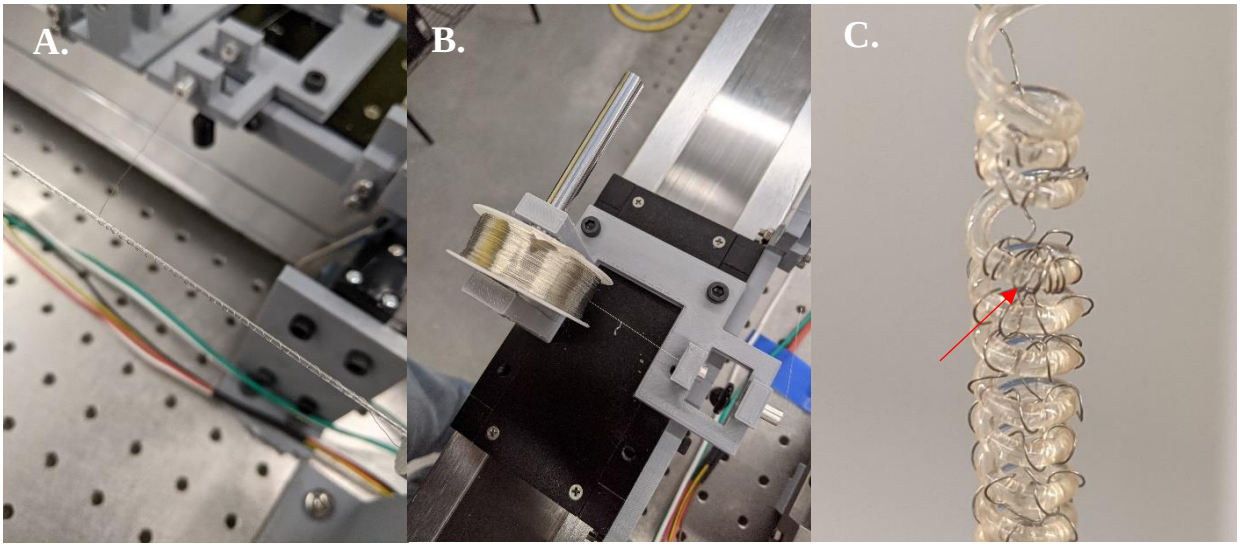

Figure 3-5: (a) Interweaving the Wire with the Fishing Line (b) Linear Actuator Wire Feeding Mechanism (c) Section of too Dense Conductive Wire

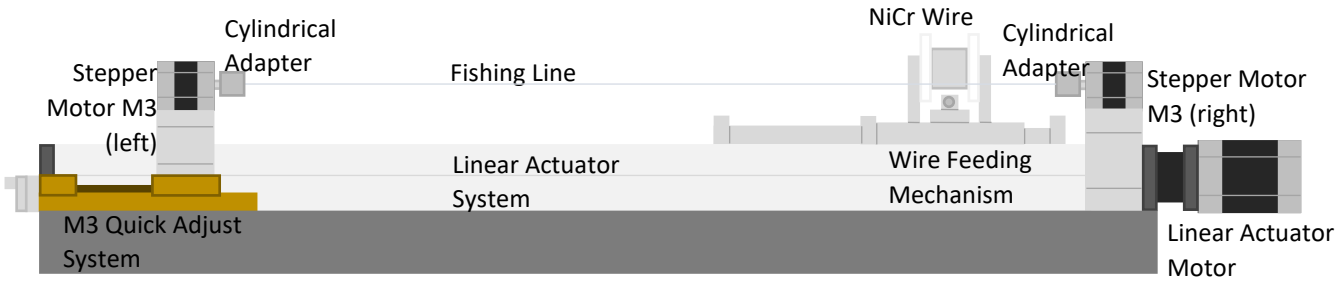

Figure 3-6: Wire Wrapping Setup

After the twisted line is wrapped with heating wire, it is taken off the M3 stepper motors, ensuring that it always has ample tension on it to disallow any untwisting. Another Autonics™ A4K-M243 stepper motor, also labelled M3, is mounted between the other M3 motors with a 3D printed adapter. An aluminum mandrel rod is fastened between the left-most M3 motor and the newly placed M3 motor. The end of the fishing line is tied to the left end of the aluminum rod, and the other free end of the twisted line is held by hand, ensuring to not allow any slack. The M3 motors are turned on at a speed of 600 pulses per second. The fishing line is wrapped onto the rod, and the free hand-held end is tied off. From here, the two adapters on the M3 motors can be detached and placed in an oven (pictured in Figure 3-8 is a Memmert™ 1.1 Cu. Ft. Gravity Universal Oven), where the coiled line is set at a temperature of 180 degrees Celsius for 90 minutes.

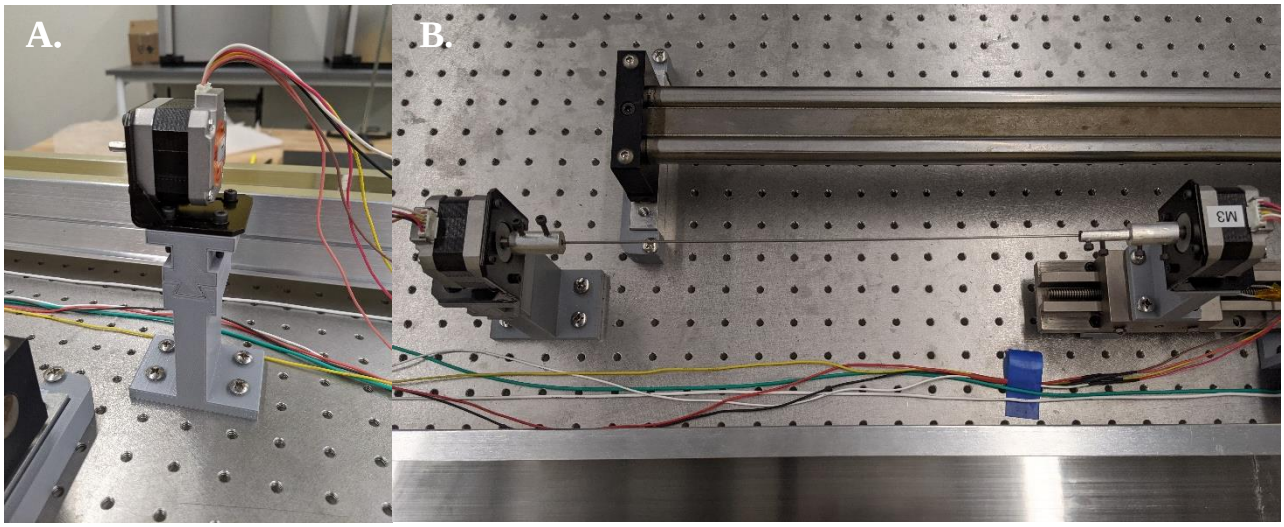

Figure 3-7: (a) M3 motor on 3D printed adapter (b) Coiling Rod Mounted between Two Stepper Motors

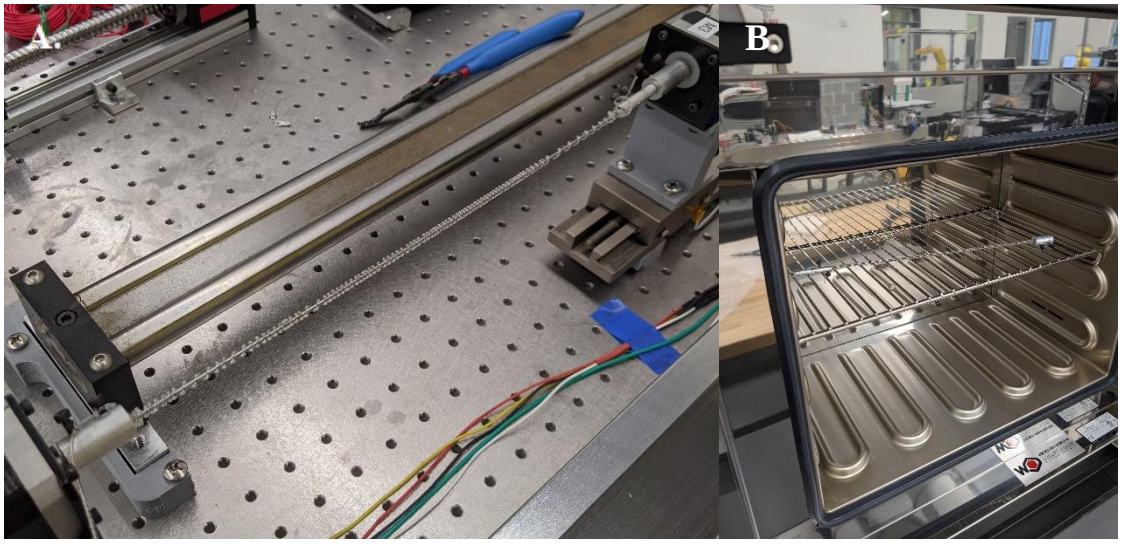

Figure 3-8: (a) Coiled fishing line on aluminum rod (b) Coiled fishing line in Oven

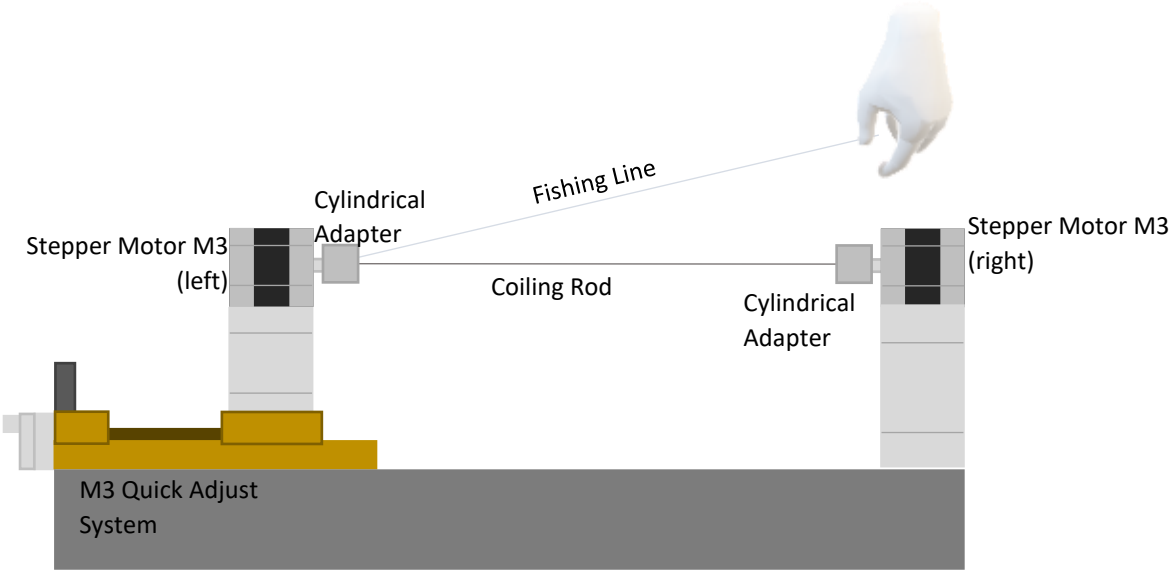

Figure 3-9: Line Coiling Setup

Part 2: Artificial Muscle Experimental Setup

Before attempting to implement these artificial muscles into a soft earthworm robot, it is necessary to collect data on the amount of displacement and heating produced by muscles of varying spring constants. The spring constants of each muscle can be tuned by changing the diameter of the mandrel rod used to coil them. Two experimental setups were used to gather data on the muscles – one for expansion muscles and one for contraction muscles.

2.1: Expansion Muscles

The fabrication process for each muscle type varies to produce the desired end effect. In the case of expansion muscles, stepper motors M2 and M3 must rotate clockwise when viewed from the front for twisting, wrapping, and coiling as shown in Figure 3-10.

Figure 3-10: Autonics™ Stepper Motor

To determine the joule heating and displacement produced by the expansion muscles, a setup is used as pictured in Figure 3-11.

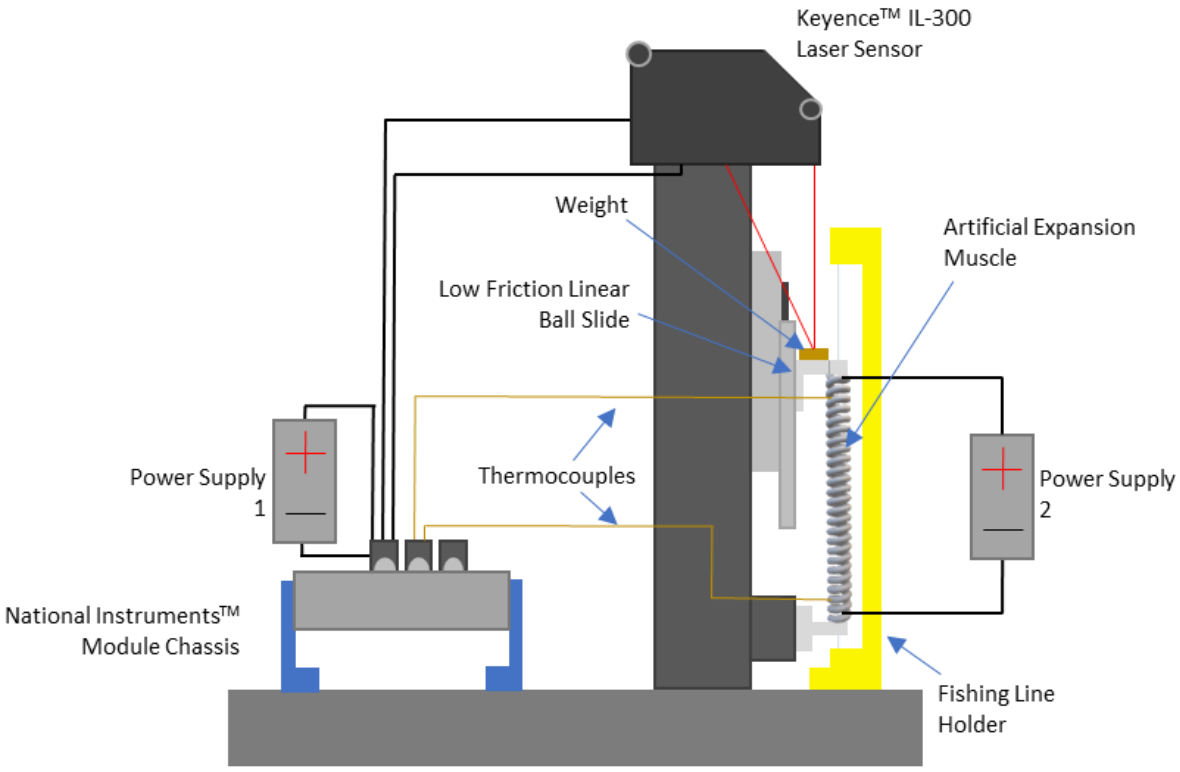

Figure 3-11: Expansion Test Setup – Clockwise Twisting, Clockwise Heating Wire Wrapping, and Clockwise Coiling

To first determine the muscle configuration with appropriate spring index for optimal displacement, three expansion muscles were produced with varying rod diameters of 0.035”, 0.041”, and 0.055”. Each muscle was loaded into the test setup by running a thin fishing line through the center and fastening the line to the yellow fishing line holder. The fishing line kept the muscle upright while remaining electrically insulated to prevent it from interfering with the electrical current running through the muscle. Two wires attached to a B&K PrecisionTM 9206 multi-range programmable DC power supply were connected at both ends of the muscles to induce a varying voltage and current. A KeyenceTM IL-300 Laser Sensor was used to measure displacement produced by the muscles as they expanded and contracted. Two thermocouples were used to determine the temperature at both ends of each muscle. Before testing each muscle,

they were trained via 10 cycles of heating and cooling to eliminate the lonely stroke while testing. A 60 second cycle was used during data collection – 15 seconds on at 0.18A, and 45 seconds off at 0A to allow for adequate cooling. This cycle was repeated five times for a total time of 300 seconds. Data was acquired via a Labview program and was placed into graphs via a Matlab program. This data was used to determine the optimal mandrel rod diameter for fabricating expansion muscles.

From here, the 0.055" rod diameter muscle was used for further expansion testing due to its larger displacement compared to the other rod diameters. Different variables were manipulated to determine their effect on the expansion properties of the artificial muscles. The primary variables tested were induced current and applied deadweight. These tests were done simply by manipulating the current at steps of 0.18A, 0.20A, and 0.22A for the former variable, and varying the applied deadweight in increments of 20g, 40g, and 60g for the latter. Two more tests were done afterwards - one to test the cyclical fatigue properties of the muscle by cycling the muscle 1000 times, and one to test the effect of pulsing high current into the muscle at 0.55A, 0.60A, and 0.65A.

2.2: Contraction Muscles

To manufacture contraction muscles, the line must be twisted clockwise in the twisting step of the muscle fabrication process with M2. The heating wire wrapping and coiling must be done counterclockwise with M3. The contraction muscles were inserted into the experimental setup seen in Figure 3-12 and tested for their heating and displacement.

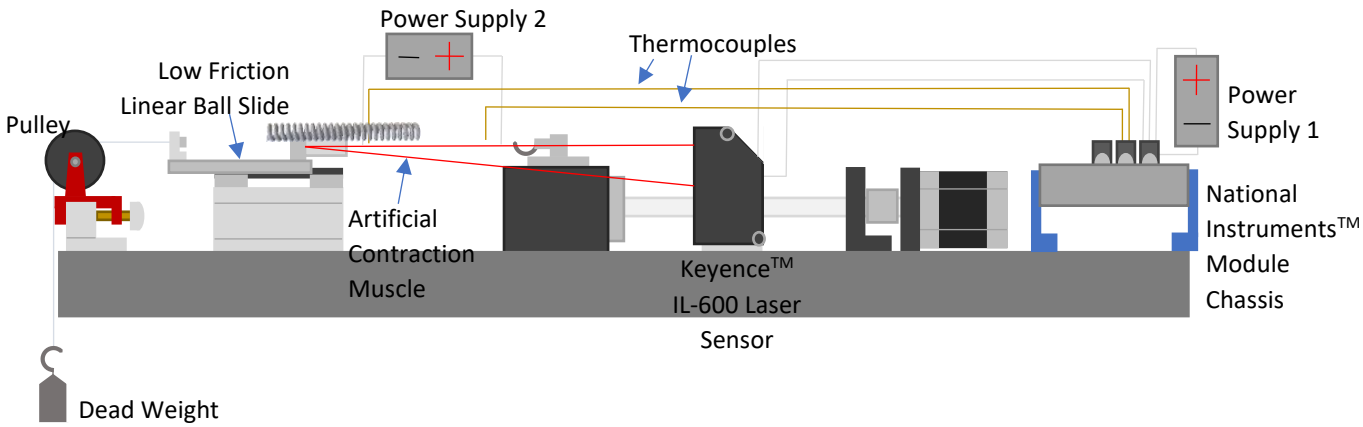

Figure 3-12: Contraction Test Setup – Clockwise Twisting, Counterclockwise Heating Wire Wrapping, and Counterclockwise Coiling

This test setup was used first to determine the optimal coiling rod diameter between a 0.035" rod, 0.041" rod, and 0.055" rod, like the expansion setup. The programmable DC power supply was again attached at both ends of the contraction muscles, along with two thermocouples to measure the temperature. A Keyence™ IL-600 laser sensor was used to measure the displacement produced by the muscles, and a 100g deadweight was attached to the linear slide system on one end of the muscle via a pulley. Each muscle was trained 10 cycles before the final Labview program was run – 15 seconds of 25V and 0.18A, and 45 seconds of 0V and 0A, for a total of five times (300 seconds). The data produced was sent to a Matlab program to be compiled into graphs.

Part 3: Earthworm Robot Prototype

The goal of creating the earthworm robot prototype was to produce a functional locomotive robot driven by a combination of expansion and contraction artificial muscles. Another focus was on modularity – if the robot could function in one section, then it would allow

for easy modification and lengthening in future research. In more traditional earthworm soft robots, locomotion was done peristaltically with at least three segments – these segments expand and contract in such a manner that the front and rear segments act as anchors to whatever surface they are moving on or through. The challenge then with a single segment robot is generating friction on either end of the robot. Two main methods were theoretically crafted in this research – one method was to use a mix of TPU and PLA to create a soft shape memory polymer endcap which would be actuated with heat to cause the endcap to shrink in size, allowing for less contact with the surface and therefore less friction. The 3D model for this can be seen in Figure 3-13.

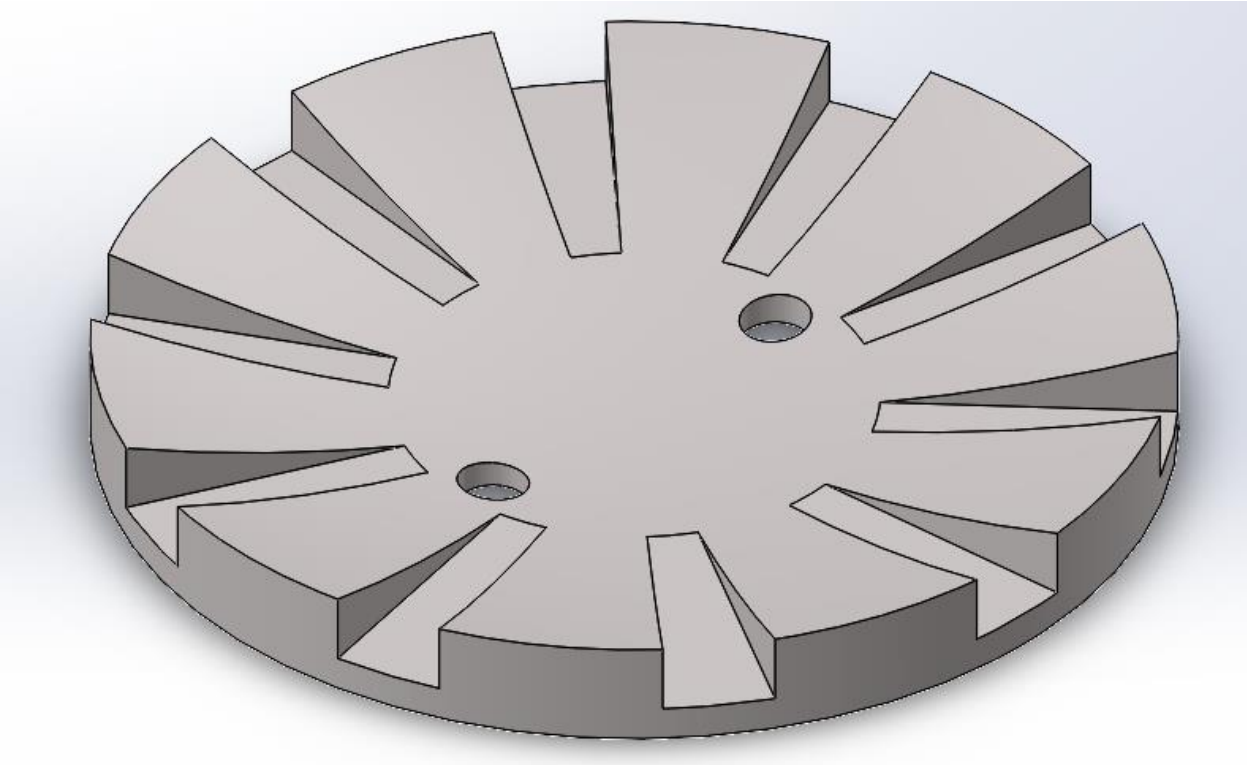

Figure 3-13: Shape Memory Polymer Variable Friction End Cap

The concave shape in tandem with the cutout channels would allow for the material to fold in on itself. One major issue with this design is the difficulty of evenly heating it, especially

in the presence of other heat sensitive entities such as the artificial muscles. For these reasons, this design was not utilized.

Instead, the end caps were created by utilizing an expansion artificial muscle. A small U-shaped piece is pushed down by the expansion muscles to reduce friction with the surface. When reduced friction is no longer desired on the front or rear, the natural cooling and retraction of the muscles pull the friction piece up into the body of the end cap. The end caps are made with a flat bottom design to ensure that the prototype does not rotate at an angle where the U-shaped friction pieces are not in contact with the surface. At the base of the design rubber tips are added to ensure that there is more friction when the U-shaped pieces are retracted within the body, and less friction when they are deployed.

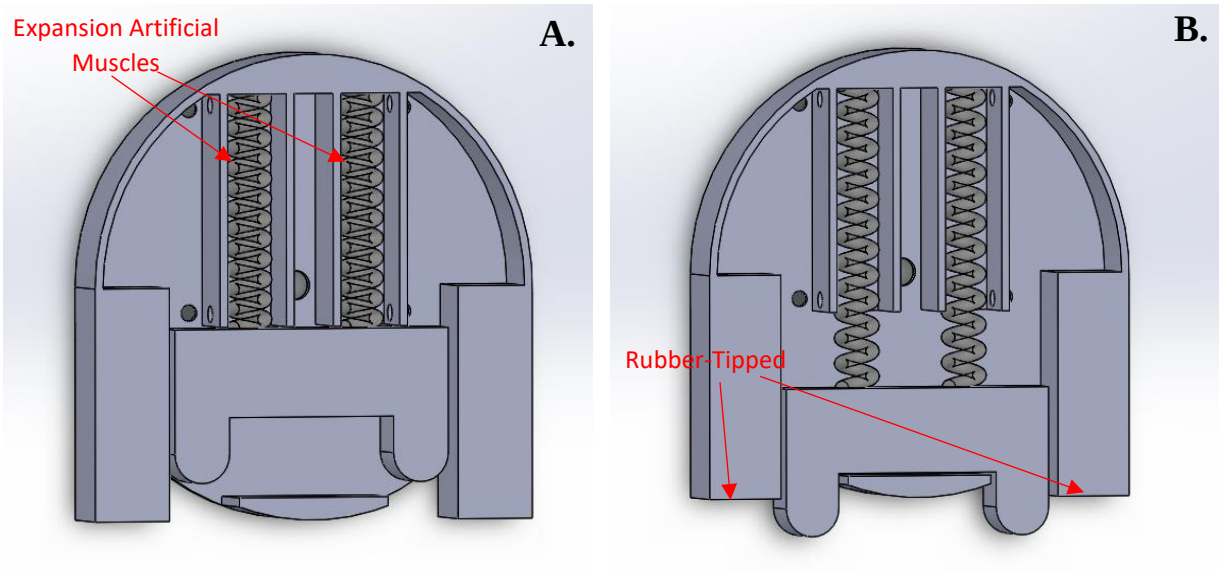

Figure 3-14: Antagonistic Spring/Expansion Muscle Variable Friction End Cap (a) In High Friction Mode (b) In Low Friction Mode

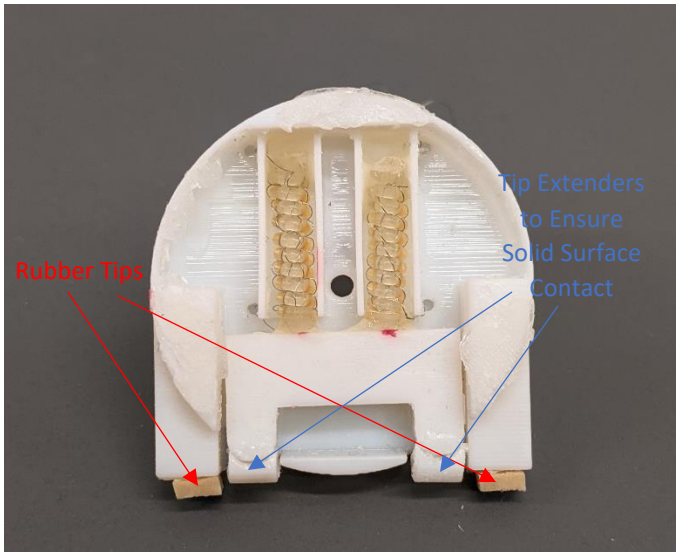

Figure 3-15: Variable Friction End Cap

Figure 3-14 shows the two states of the end cap – the left model shows with the U-shaped variable friction piece in the up position, and the right model shows the muscle actuated which pushes the U-shaped variable friction piece out of the end cap. The holes in the model allow for wires to be separated to prevent any accidental heating of the driving muscles of the robot.

When creating the prototype, ensuring that the NiCr heating wires remained separate was paramount to successful locomotion. A multi-part end cap section with cut out wire channels allowed for the wires to remain separated as they were bundled together on either end of the robot.

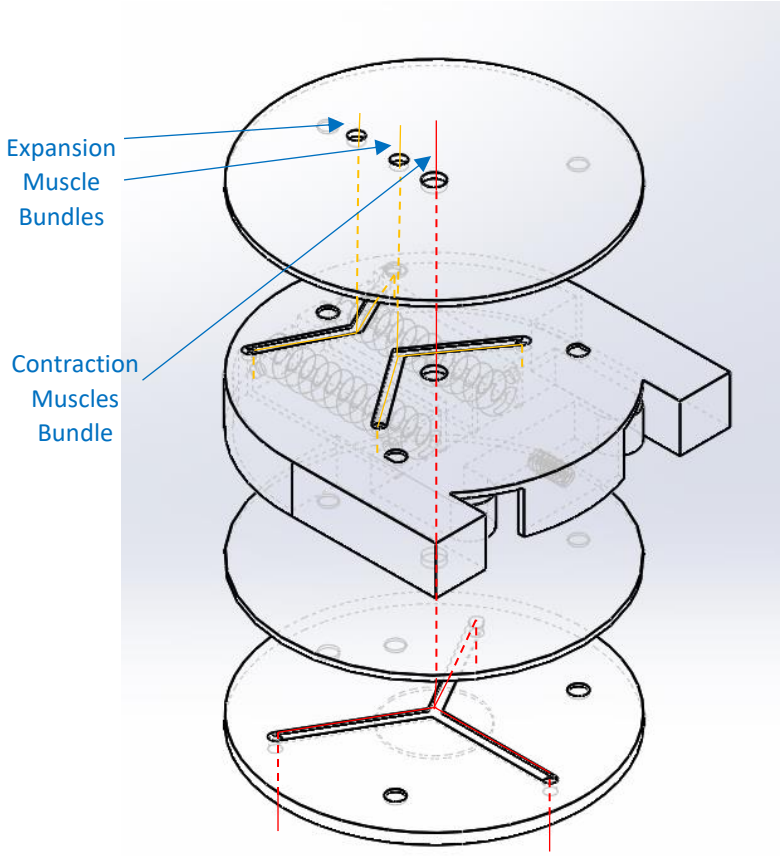

Figure 3-16: Multi-part End Cap Section with Wire-Separating Channels

A total of seven muscles are used for this prototype – three contraction muscles in the primary middle locomotion section, and four expansions muscles housed in either end of the robot. The three contraction muscles are cut to a length of 40mm and are placed equidistant away

from one another in the middle section of the robot with a 40mm long spring in the center of the robot. Data on this spring can be seen in Table 3-1.

Spring Type	Compression
Length	40 mm
OD	6.35 mm
ID	5.49 mm
Wire Diameter	0.43 mm
Spring Constant	0.111 N/mm
Material	302 Stainless Steel

Table 3-1: Prototype Center Spring Metrics

A silicone shell was created using a Hyrel Hydra 16A multi-material 3D printer. This shell serves a few purposes. It helps keep dust and debris out of the central cavity that houses the artificial muscles and center spring, it helps keep a more rigid body shape for the prototype, and it helps keep the muscles from bending out of shape. A shell was created first by producing a hollow mold of water-soluble PVA (done on painters' tape to allow for better built plate adhesion). The processing parameters for the PVA printing can be seen in Table 3-2.

Material	Kodak™ 1.75mm PVA
Print Speed	5 mm/s
Layer Height	0.15mm
Print Head Temperature	220 degrees C
Print Bed Temperature	45 degrees C
Print Time	11 hr 38 min

Table 3-2: PVA Printing Parameters

After the PVA mold was finished, dynamic mixing heads were then used to fill the mold with SmoothOn™ Ecoflex™ 00-30 silicone. This is a two-part silicone mixture that was mixed in a 1:1 ratio between parts A and B and was allowed to set for 4 hours before taking the entire build out of the printer and placing it into a Vevor™ 26-30L Digital Ultrasonic Cleaner at 35 degrees Celsius. With the heated water and sonic agitation, the PVA was fully dissolved within 3 hours, and the result was an easily customizable 3D printed silicone shell. The processing parameters for the silicone can be seen in Table 3-3.

Material	SmoothOn™ Ecoflex™ 00-30
Print Speed	5 mm/s
Print Head Temperature	Not heated
Print Bed Temperature	Not applicable
Print Time	7 min

Table 3-3: Silicone Printing Parameters

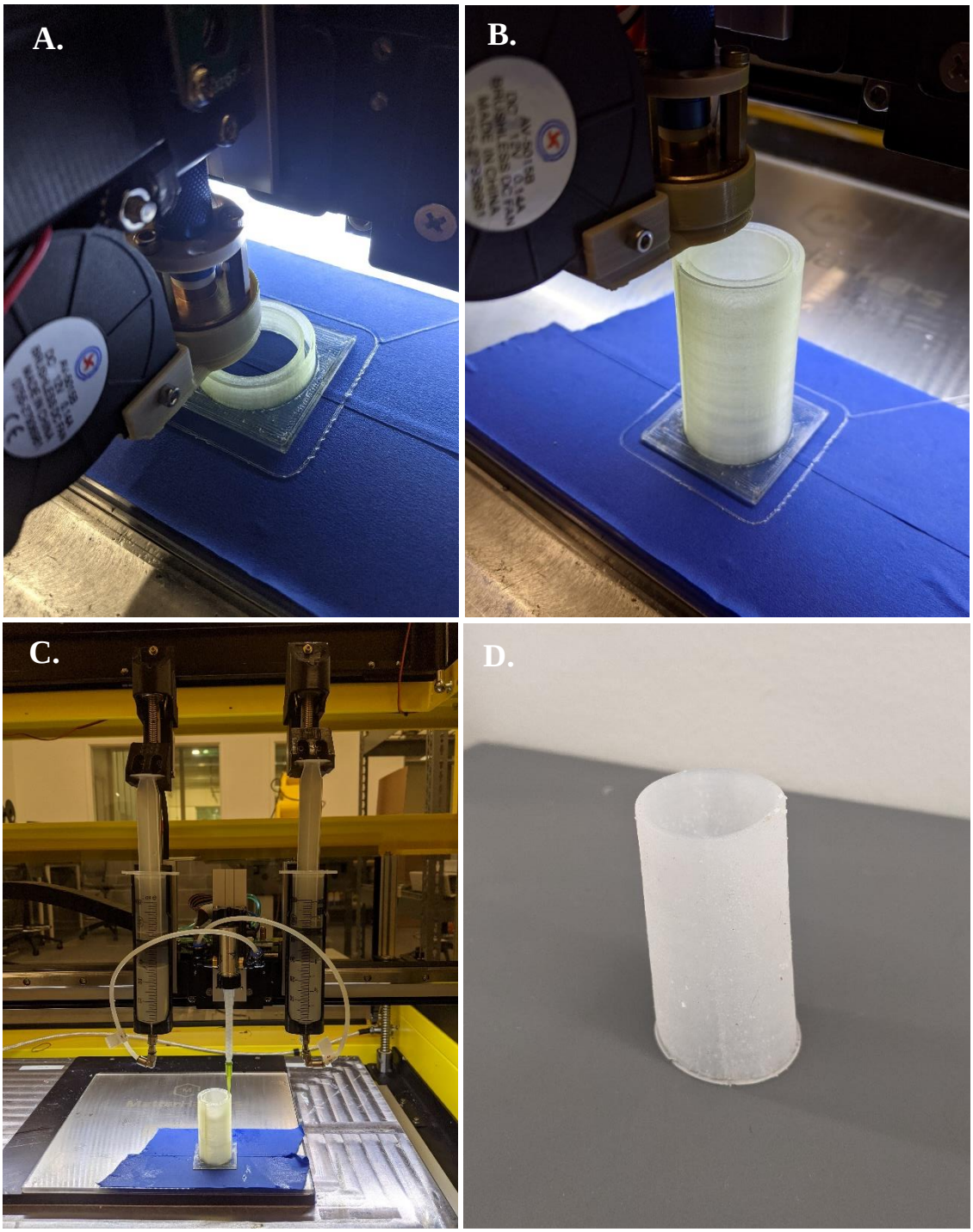

Figure 3-17: (a) PVA Printing First Stages (b) PVA Printing Final Stages (c) Dynamic Silicone Mixing Head Inserting Silicone into PVA Mold (d) Finished Silicone Shell

The three contraction artificial muscles were attached to the base of the end caps after their wires were fed through the wire channels and bundled with Tuofeng^{TM} heat shrink wire

tubes. The muscles themselves were attached to the end caps with Loctite™ Instant Mix™ Epoxy. The silicone shell was attached to the end cap around the artificial muscles via Loctite™ Instant Mix™ Epoxy. The end caps were aligned with alignment pegs and secured in place via Loctite™ Ultragel Control™ Super Glue. The multi-section end caps were assembled and placed with Loctite™ Instant Mix™ Epoxy.

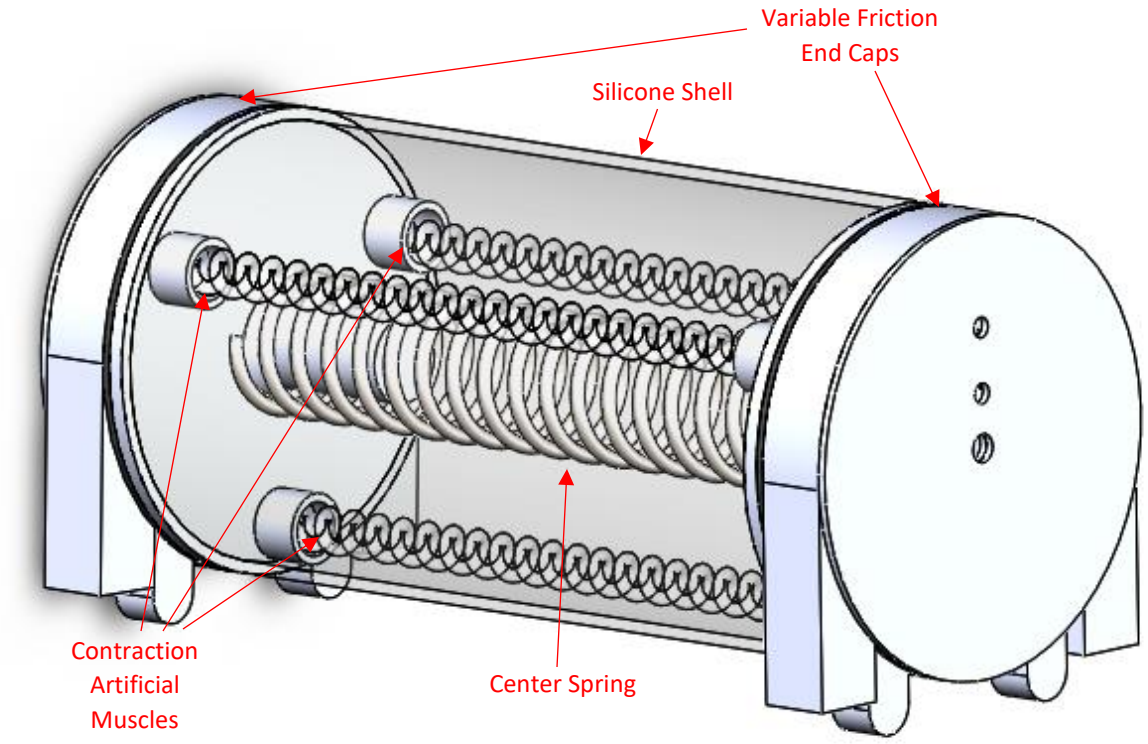

Figure 3-18: 3D Model of the Earthworm Robot Prototype

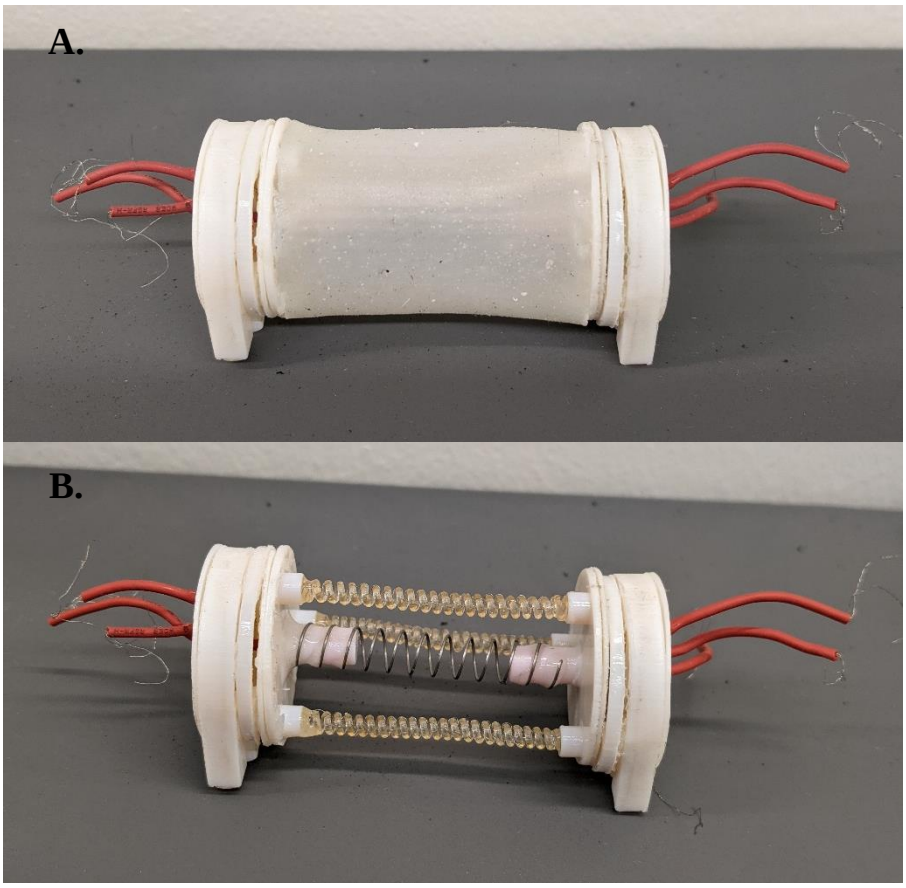

Figure 3-19: Real-Life Earthworm Robot Prototype with Silicone Shell attached (a) and without Silicone Shell attached (b)

Length	62.6mm
Diameter	28mm
Number of Segments	1
Weight	16g
Actuation Method	Artificial Muscles
Cycle Frequency	1 cycle/60 seconds

Table 3-4: Earthworm Robot Prototype Metrics

When the contraction muscles are heated, the length of the prototype decreases. When heat is no longer applied to the contraction muscles, the central spring allows the prototype to return to its original length. By periodically actuating the contraction muscles in tandem with the

expansion muscles within the variable friction endcaps, the prototype robot can move forward with only one segment. The movement can be seen broken into 4 repeating steps below in Figure 3-20. In step 1, from 0-15 seconds, the front variable friction actuator is powered on. In step 2, from 15-30 seconds, the central actuator is powered on, and the front variable friction actuator is powered off. In step 3, from 30-45 seconds, the rear variable friction actuator is powered on, and the central actuator is powered off. In step 4, from 45-60 seconds, the rear variable friction actuator is powered off, meaning all actuators are off and cooling. The cycle restarts after 60 seconds.

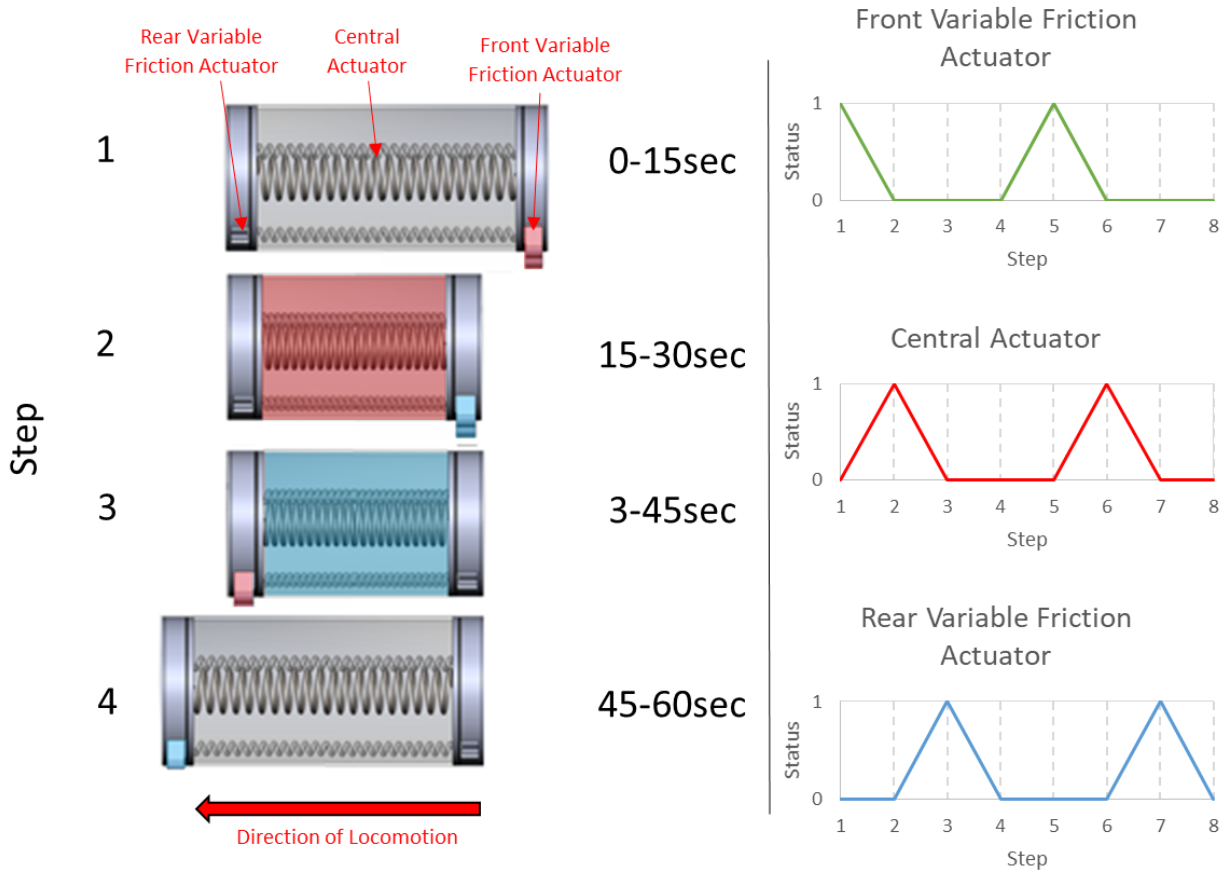

Figure 3-20: Movement Breakdown of Prototype – Status 1 represents that actuator receiving power; Status 0 represents that actuator not receiving power. Red highlights represent heating, blue highlight represent cooling

This movement was programmed through electrical pulses in the form of sequential commands controlled via a PLC and three solid-state relays.

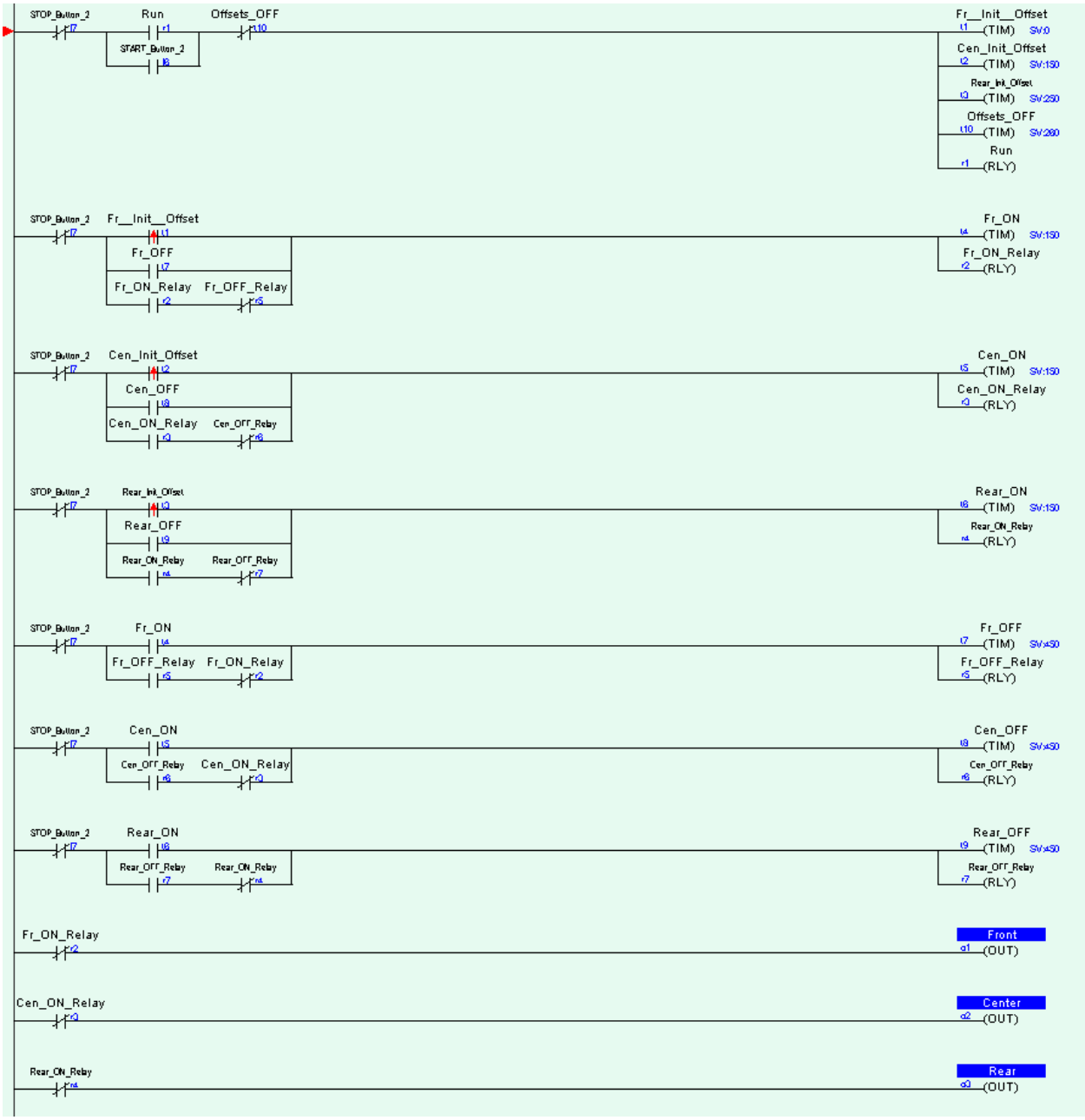

Figure 3-21: Ladder Logic Diagram for Earthworm Segment Propagation

The ladder logic seen in Figure 3-21 uses a series of cascading and cyclically repeating timers to signal each segment to actuate on or off in the pattern seen in Figure 3-20. These timers

induce a wavelike, peristaltic movement technique that induces locomotion in the prototype. This program was transferred to a Triangle Research™ Fx2424 PLC, which was used to control Schneider Electric™ SSM1D26BD solid state relays (SSRs) that can apply currents to the different segments. The SSRs and PLC were powered with two programmable power supply units (PSUs) – one unit controlled the voltage and amperage of the variable friction end caps, and one unit controlled the voltage and amperage of the central actuator. The SSRs, PSUs, and PLC were wired together using a breadboard and attached to the prototype using insulated copper wiring held on with electrician's tape.

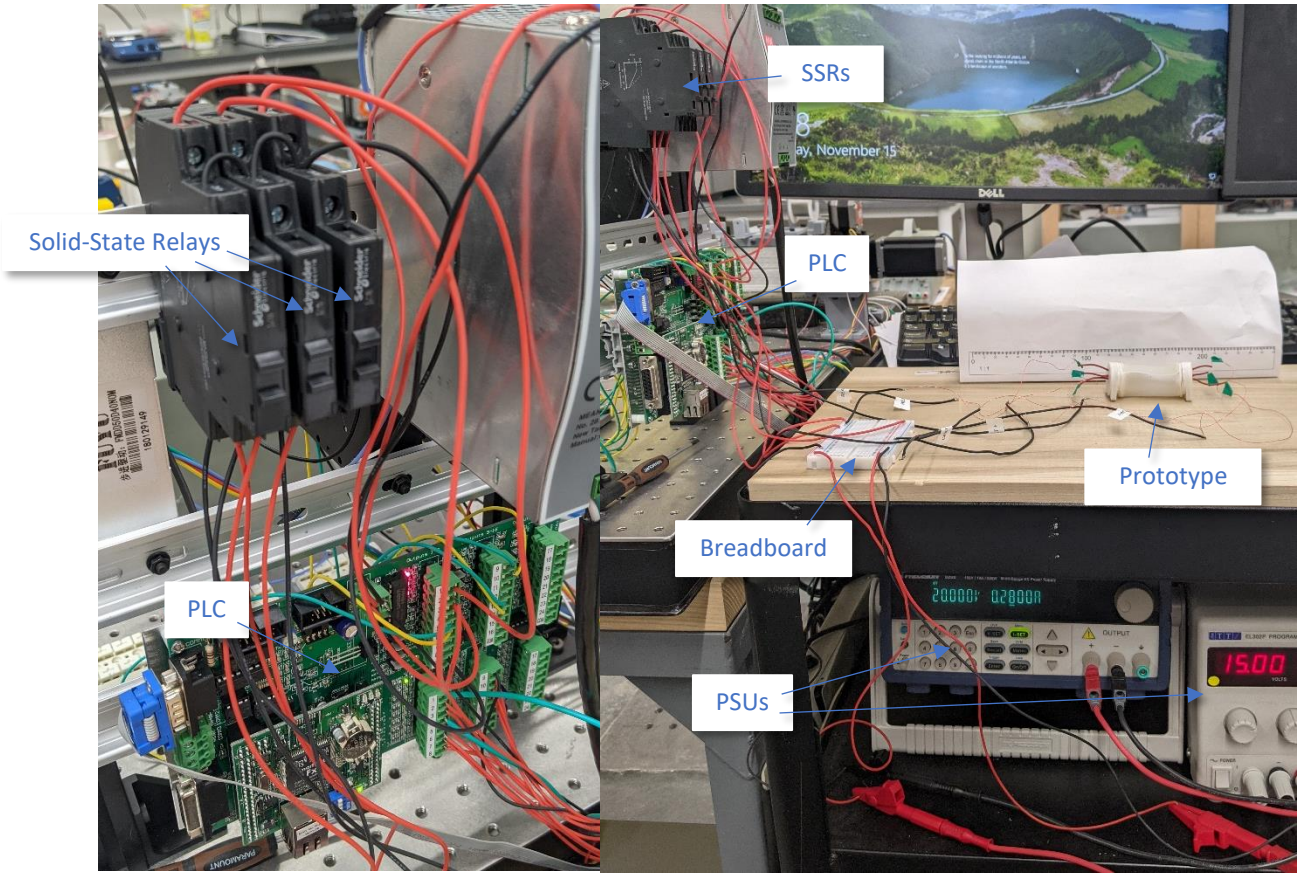

Figure 3-22: Wiring for Prototype Test Setup

Various metrics were used to quantify the performance of the prototype. These metrics were axial deformation, velocity, and maximum payload. These metrics were also tested at varied induced amperages to the central actuator to test the effects of greater axial deformation during cycles. Two main setups were used to gather the required data. The first one was configured to measure axial deformation and velocity of the prototype. A Logitech™ C922 Pro camera was placed to record the movement of the prototype in front of a metric scale. The prototype was programmed to begin locomotion for 120 seconds or two cycles. The camera was programmed to take a picture of the prototype at 0 seconds to record the initial position, a picture at 30 seconds (when the central actuator reaches peak displacement) to measure the value of axial deformation, and then take a picture at 120 seconds to measure total displacement and therefore velocity. The setup can be seen in Figure 3-23.

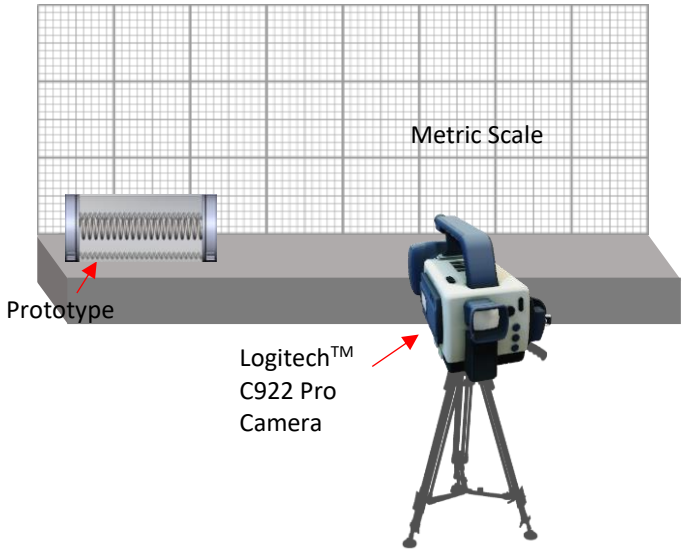

Figure 3-23: Prototype Velocity and Axial Deformation Testing Setup

The second setup was used to determine maximum payload. This setup is similar in appearance and functionality to the setup used for contraction artificial muscle data collection. A dead weight is dangled over the edge of a table and attached to the prototype with fishing line

guided through a pulley. The fishing line is tied to the dead weight and to the center of the end cap of the prototype. The same camera and metric scale setup from the previous test were used to measure the axial deformation, total displacement, and velocity of the prototype over the course of 120 seconds with the varying dead weights. The setup can be seen in Figure 3-24.

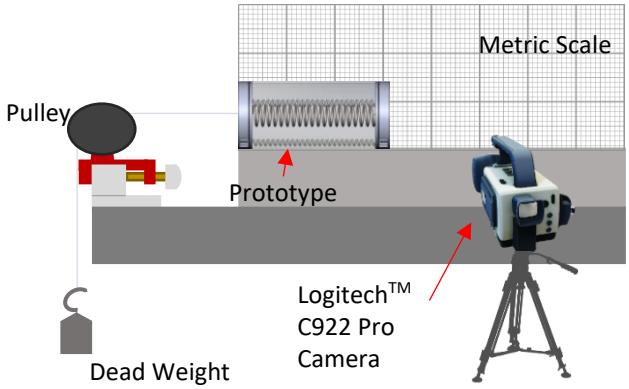

Figure 3-24: Prototype Maximum Payload Testing Setup

CHAPTER 4
RESULTS AND DISCUSSION

Part 1: Expansion Test Results

A total of five expansion experiments were conducted to obtain data on the properties of expansion fishing line artificial muscles in regard to their performance when varying the rod diameters used to manufacture them, varying the deadweights, varying the applied current, running a 1000 cycle fatigue test, and when using high current, low duration electrical pulses. The muscle pitch (distance between coils) for these muscles was 1.59mm. The coil bias angle – the angle between the fiber and the coil's cross-section - is shown in Figure 4-1 and was 15.6 degrees for these muscles. The image used to measure the coil bias angle was taken with a HAYEAR™ HY-150X USB microscope and was processed with HAYEAR™ proprietary microscope image processing software. The results of these tests can be seen in subsections 1.1-1.5.

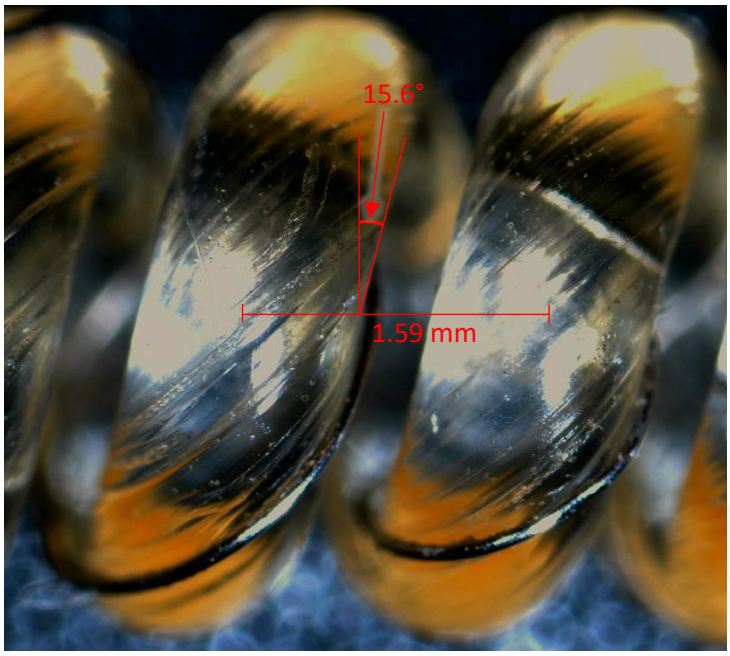

Figure 4-1: Coil Bias Angle of an Expansion Artificial Muscle Measured from a Microscopic View. Taken with HAYEAR™ HY-150X USC Microscope

1.1: Varied Rod Diameter

Three rod diameters were used – 0.035”, 0.041”, and 0.055” with a length of 73.4mm, 73.2mm, and 68.3mm respectively. The spring index – a correlation between the mean diameter of a spring and the wire diameter of a spring - of each muscle was calculated with Equation 4-1.

Equation 4-1:

$$Spring\ Index\ (C) = \frac{Mean\ Coil\ Diameter\ (D)}{Fiber\ Diameter\ (d)}$$

The spring index of the 0.035” rod diameter muscle was 2.98, the spring index of the 0.041” rod diameter muscle was 3.23, and the spring index of the 0.055” rod diameter muscle was 3.63. No deadweight was applied to the expansion carriage for this experiment. A current of 0.20A was applied to each muscle. The loaded length of the 0.035” rod diameter muscle was 73.4mm, the loaded length of the 0.041” rod diameter muscle was 73.2mm, and the loaded

length of the 0.055” rod diameter muscle was 68.3mm. Heating time was 15 seconds, and cooling time was 45 seconds. This cycle was repeated five times for a total duration of 300 seconds.

Rod Diameter	Spring Index	Loaded Length	Deadweight	Current	Heating Time	Cooling Time
0.035”	2.98	73.4	0g	0.20A	15s	45s
0.041”	3.23	73.2				
0.055”	3.63	68.3				

Table 4-1: Experimental Conditions for Expansion Muscles Varied Rod Diameter Experiment

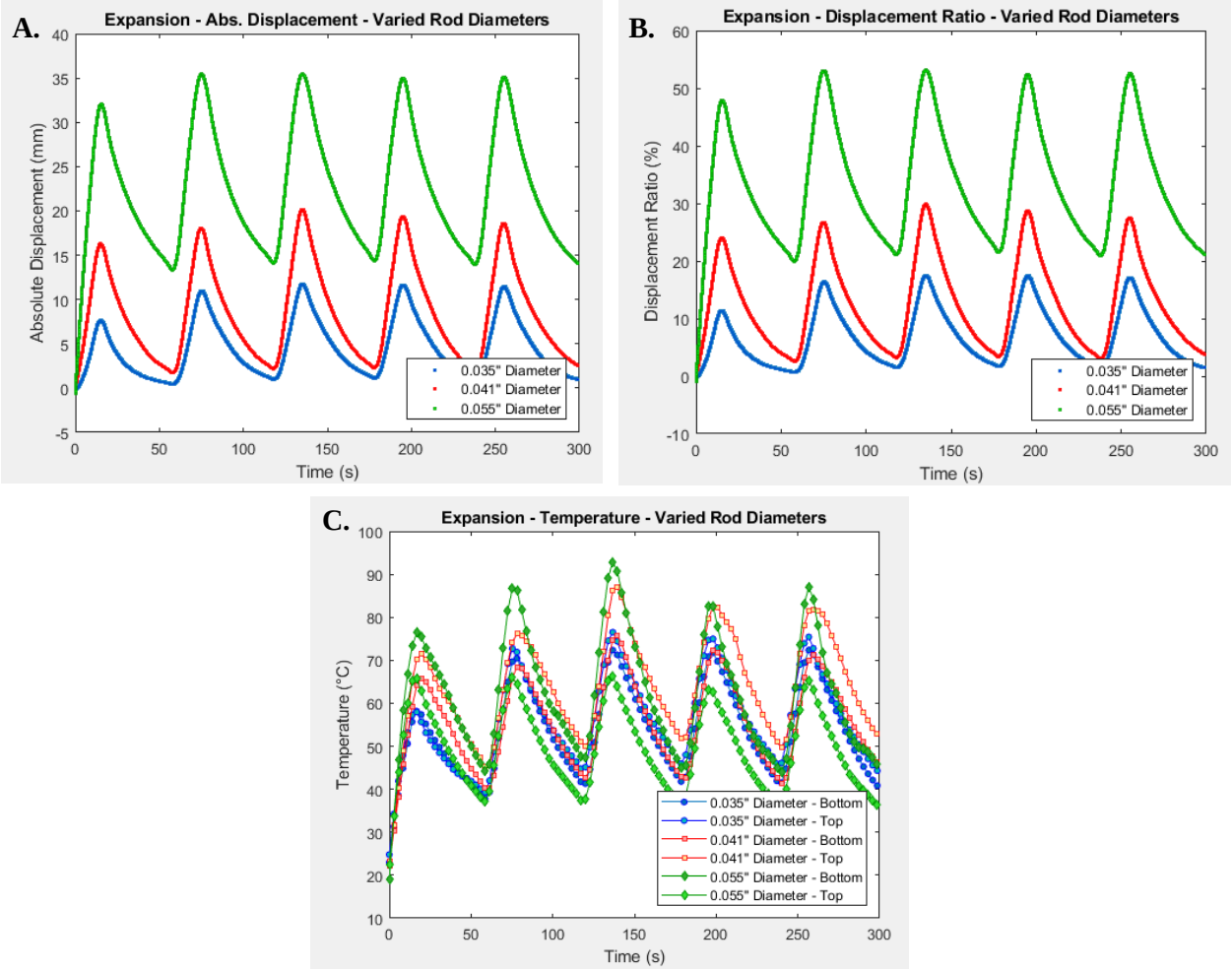

Figure 4-2: Expansion Muscles – Varied Rod Diameters (a) Absolute Displacement produced (b) Displacement Ratio calculated as a ratio of displacement produced and muscle length (c) Probe Temperatures at the top and bottom of each muscle

Figure 4-2 shows the results gathered from this experiment. It is obvious when viewing graphs A and B that the 0.055” rod diameter muscle produced the largest absolute displacement with a peak value of 35.3mm as well as the largest displacement ratio reaching up to 54%. The next highest was the 0.041” rod diameter muscle with a peak absolute displacement value of 20.1mm and a peak displacement ratio of 29.8%. The lowest peaks corresponded to the 0.035” muscle with a peak absolute displacement of 11.7mm and a peak displacement ratio of 17.5%. The 0.055” rod diameter muscle reached the highest peak temperature of 92.8 degrees Celsius,

the 0.041” rod diameter muscle reached a peak temperature of 86.9 degrees Celsius, and the 0.035” rod diameter muscle reach the peak temperature of 76.5 degrees Celsius. The data shows a clear trend that the larger the rod diameter used, and consequently the larger the spring index of the muscle, the higher the displacement produced as well as the higher the peak temperature produced.

1.2: Isotonic Test (Varied Dead Weight)

The 0.055” diameter muscle was used in this experiment as well as subsequent experiments due to its attractive displacement qualities. For the varied dead weight experiment, three weight increments were used: 20g, 40g, and 60g. The pre-loaded muscle lengths were 67.6mm, 67.4mm, and 67.3mm respectively. Like the prior experiment, a current of 0.20A was applied. Heating time was 15 seconds, and cooling time was 45 seconds. This cycle was repeated five times for a total duration of 300 seconds.

Rod Diameter	**Loaded Lengths**	**Deadweight**	**Current**	**Heating Time**	**Cooling Time**
0.055”	67.6mm	20g	0.20A	15s	45s
	67.4mm	40g			
	67.3mm	60g			

Table 4-2: Experimental Conditions for Expansion Muscles Isotonic Experiment

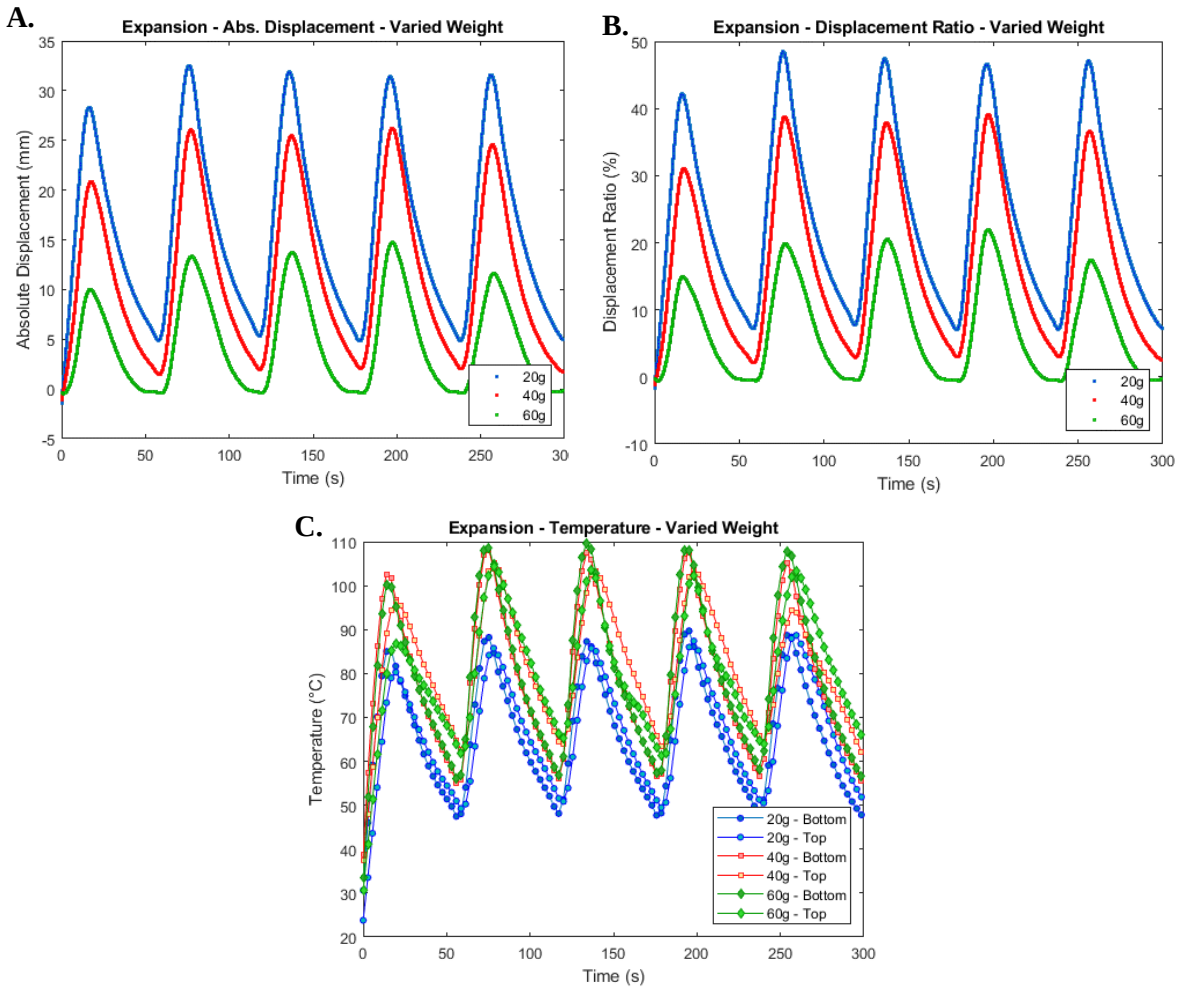

Figure 4-3: Expansion Muscles – Varied Dead Weight (a) Absolute Displacement produced (b) Displacement Ratio calculated as a ratio of displacement produced and muscle length (c) Probe Temperatures at the top and bottom of each muscle

Figure 4-3 shows a clear relationship between dead weight and displacement. A deadweight of 20g produced a maximum absolute displacement of 32.6mm, whereas a deadweight of 40g and 60g produced a maximum absolute displacement of 26.1mm and 14.6mm respectively. The maximum displacement ratio for each was 48.2% for 20g, 38.9% for 40g, and 21.8% for 60g. The temperature produced seemed to also be affected by deadweight – the lowest peak temperature correlated to 20g at 97.5 degrees Celsius, the 40g deadweight had a peak

temperature of 109.2 degrees Celsius, and the 60g deadweight had the highest peak temperature of 111.2 degrees Celsius.

1.3: Varied Current Test

The third test conducted was to determine the effect of varied currents running through the 0.055" rod diameter muscle. Three currents were used – 0.18A, 0.20A, and 0.22A. The voltage applied to the terminals of the muscles was also measured. 30g of dead weight was used for this experiment due to its desirable 30-40% peak displacement ratio when induced with a 0.20A current as measured in the varied dead weight experiment. The pre-loaded muscle length for all three currents was 67.6mm. The same cycle of 15 seconds on and 45 seconds off was used. This cycle repeated five times for a total duration of 300 seconds.

Rod Diameter	**Loaded Length**	**Deadweight**	**Current**	**Heating Time**	**Cooling Time**
0.055"	67.6mm	30g	0.18A	15s	45s
			0.20A		
			0.22A		

Table 4-3: Experimental Conditions for Expansion Muscles Varied Current Experiment

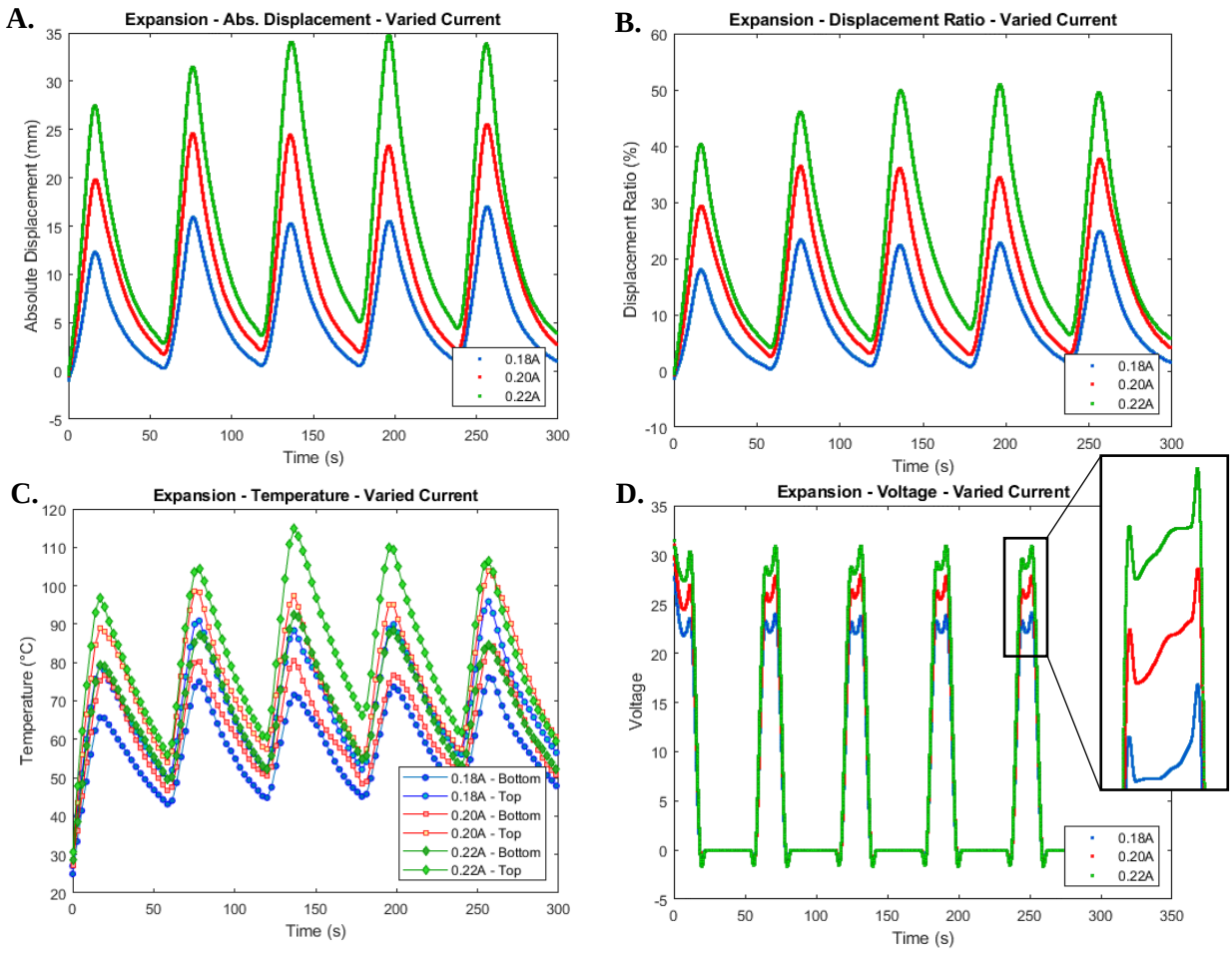

Figure 4-4: Expansion Muscles – Varied Current (a) Absolute Displacement produced (b) Displacement Ratio calculated as a ratio of displacement produced and muscle length (c) Probe Temperatures at the top and bottom of each muscle (d) Voltage produced

Figure 4-4 demonstrates the relationship between the applied current and the displacement, temperature, and voltage. Graphs A and B exemplify the profound effect of a higher current in regard to displacement – 0.18A produced an absolute displacement of 17.2mm and a displacement ratio of 25.2%, 0.20A produced an absolute displacement of 25.6mm and a displacement ratio of 37.9%, and 0.22A produced an absolute displacement of 35.5mm and a displacement ratio of 51.9%. The temperatures clearly correlate to the induced current – 0.18A produced a peak temperature of 96.6 degrees Celsius, 0.20A produced a peak temperature of

104.5 degrees Celsius, and 0.22A produced a peak temperature of 115.5 degrees Celsius. The voltages corresponded as follows – 0.18A maximum voltage was 24.5V, 0.20A maximum voltage was 27.9V, and 0.22A maximum voltage was 31V.

1.4: Fatigue Test

The fatigue test was performed to determine at what point the artificial muscles began to degrade to a point where they were no longer usable. A 0.055" rod diameter artificial muscle was used with a 20g deadweight. The muscle was cycled on at 0.18A for 15 seconds and off for 45 seconds a total of 1000 times. The total cycle ran for 60000 seconds. The loaded length of the muscle was 45.1mm.

Rod Diameter	**Loaded Length**	**Deadweight**	**Current**	**Heating Time**	**Cooling Time**
0.055"	45.1mm	20g	0.18A	15s	45s

Table 4-4: Experimental Conditions for Expansion Fatigue Experiment

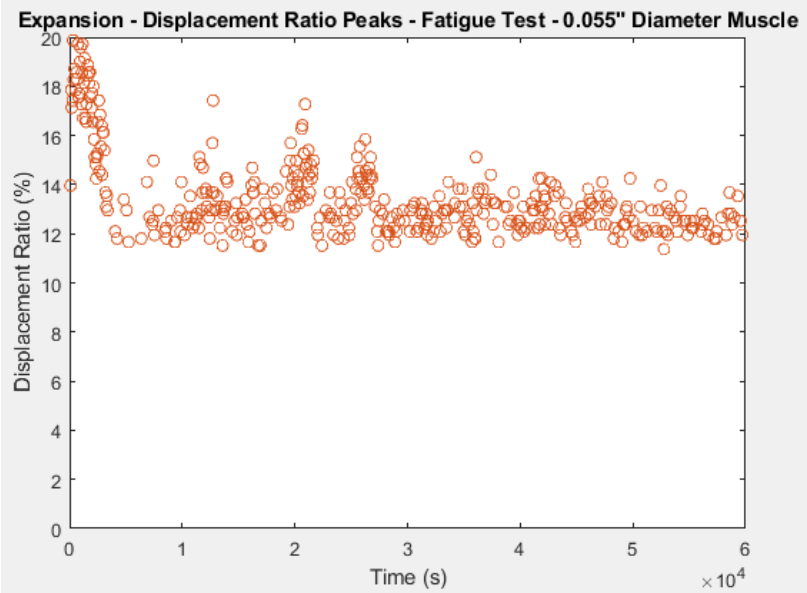

Figure 4-5: 0.055” Rod Diameter Expansion Muscle - Fatigue Test

Figure 4-5 shows the displacement ratio peaks produced by the muscle throughout the 1000 cycle fatigue test. The data was down sampled to a 1:100 ratio too allow for more visual clarity. It is clear from the first section of the graph from 0 seconds to roughly 5000 seconds, the muscle is rapidly decreasing in its average peak value. This is due to slight degradation both in the nylon fishing line and in the NiCr heating wire. After the fishing line and heating wire are “broken in” so to speak, the maximum average peak displacement ratio values level out around the 12-15% range, with notable jumps around 12000 seconds, 20000 seconds, and 26500 seconds. Figure 4-6 shows a subtle visual change in the muscle from cycle 0 to the end of the fatigue test that allows for viewing of the degradation of the nylon fishing line and NiCr heating wire.

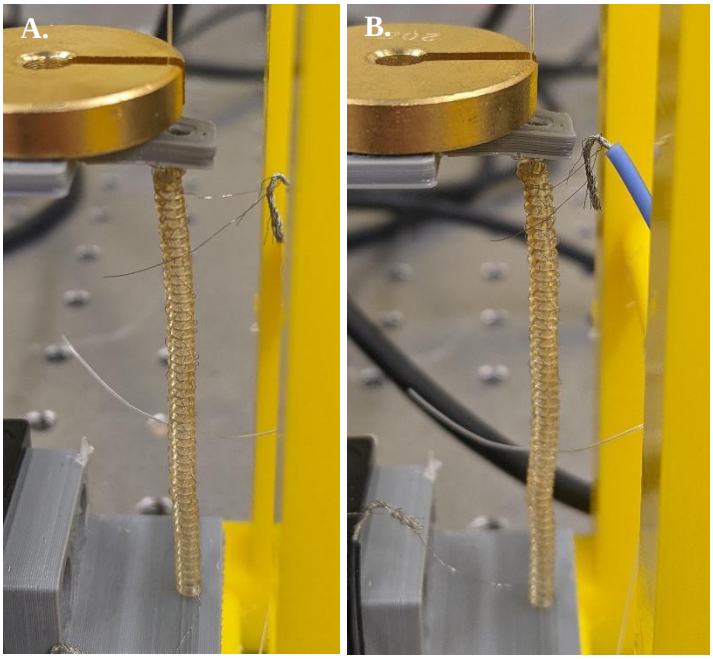

Figure 4-6: Expansion Fatigue Test (a) At 0 cycles and (b) At 1000 cycles – Very slight discoloration can be seen both in the fishing line and heating wire

1.5: Pulse Test

The goal of the pulse test was to generate a high current in a short time (1 second) and observe how the muscle reacts. This test was designed to observe the effect of high pulsed currents and how much displacement can be rapidly produced with these muscles. The amount of energy produced in the short 1 second cycle was made to match the energy produced in the typical 15 second ON period. This was calculated with Equation 4-2. Note that energy loss is ignored.

Equation 4-2:

$$I_1^2 R_1 t_1 = I_2^2 R_1 t_2$$

Simplified to:

$$I_2 = I_1\sqrt{\frac{t_1}{t_2}} \quad \rightarrow \quad I_2 = 0.18A\sqrt{\frac{15s}{1s}} \quad \rightarrow \quad I_2 = 0.7A$$

It was determined through this equation that the current should be set to 0.70A for 1 second during the pulse test. The same rest period of 45 seconds was used between ON periods. After testing increasing currents on the expansion muscles, it was found that around 0.65A permanent damage was being done to the muscles in the form of broken conductive wires, melted fishing line, and coils bunching together and sticking. Therefore, the pulse test was scaled back to three currents at 0.55A, 0.60A, and 0.65A to observe the trend of varying currents on the muscles. No deadweight was used for this test. The 0.055" rod diameter muscle was used for this test with a length of 62.9 mm. Five cycles of ON for 1 second and OFF for 45 seconds were conducted for a total cycle time of 230 seconds.

Rod Diameter	**Loaded Length**	**Deadweight**	**Current**	**Heating Time**	**Cooling Time**
0.055"	62.9mm	0g	0.55A	1s	45s
			0.60A		
			0.65A		

Table 4-5: Experimental Conditions for Expansion Muscles Pulse Experiment

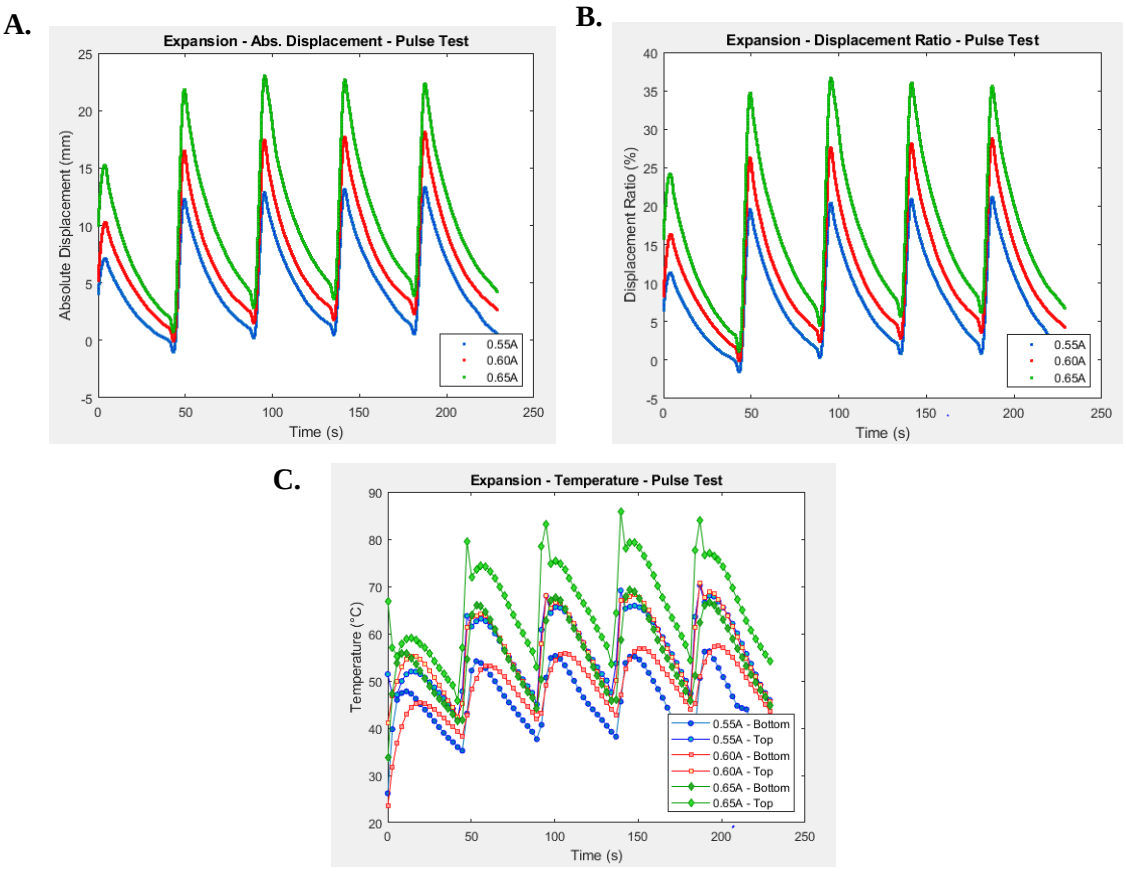

Figure 4-7: Expansion Muscles – Pulse Test (a) Absolute Displacement produced (b) Displacement Ratio calculated as a ratio of displacement produced and muscle length (c) Probe Temperatures at the top and bottom of each muscle

Figure 4-7 exemplifies the relationship between the higher amperage pulses and higher absolute displacement, displacement ratio, and temperature. The 0.65A pulse allowed for the highest overall absolute displacement of 22.8mm, the highest displacement ratio of 36%, and the highest maximum temperature of 86.9 degrees Celsius. The 0.60A pulse yielded an absolute displacement of 18.4mm, a displacement ratio of 29.4%, and a maximum temperature of 74.1 degrees Celsius. As expected, the 0.55A pulse yielded the lowest in the three metrics with an absolute displacement of 13.4mm, a displacement ratio of 21.3%, and a maximum temperature of 68.6 degrees Celsius.

The data collected from these experiments was compiled together and can be seen in Table 4-6 barring the fatigue test data.

Expansion Muscle Data					
	Parameters	**Max. Abs. Displacement**	**Max. Displacement Ratio**	**Max. Temperature**	**Voltage**
Varied Rod Diameter	0.035"	11.7mm	17.5%	76.5°C	-
	0.041"	20.1mm	29.8%	86.9°C	-
	0.055"	35.3mm	54.0%	92.8°C	-
Varied Dead Weight	20g	32.6mm	48.2%	97.5°C	-
	40g	26.1mm	38.9%	109.2°C	-
	60g	14.6mm	21.8%	111.2°C	-
Varied Current	0.18A	17.2mm	25.2%	96.6°C	24.5V
	0.20A	25.6mm	37.9%	104.5°C	27.9V
	0.22A	35.5mm	51.9%	115.5°C	31.0V
Pulse Test	0.55A	13.4mm	21.3%	68.6°C	-
	0.60A	18.4mm	29.4%	74.1°C	-
	0.65A	22.8mm	36.0%	86.9°C	-

Table 4-6: Expansion Muscle Data

Part 2: Contraction Test Results

The same five experiments that were done for the expansion muscles were also performed for the contraction muscles. These experiments, like previously stated, were designed to measure empirically the properties of contraction artificial muscles. They were done in the following order: varied rod diameter, varied dead weight, varied applied current, 1000 cycle fatigue test, and a high-current low-actuation-period test. The muscle pitch for the contraction muscles was 1.26mm and the coil bias angle was 13.5 degrees. These values are both smaller than the ones measured for the expansion muscle. This is because the contraction muscles form a much tighter coil due to the fact that the clockwise twisting and counterclockwise coiling cause the coils to form tighter around the mandrel rod.

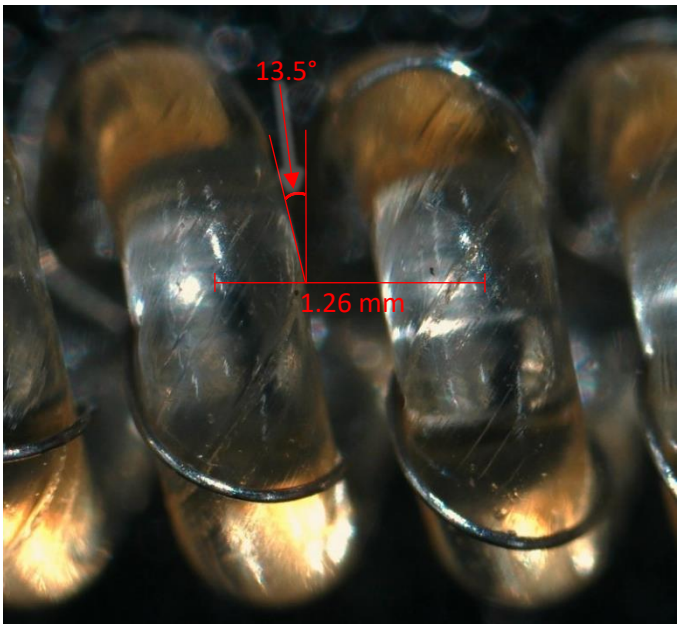

Figure 4-8: Coil Bias Angle of Contraction Artificial Muscle Measured from a Microscopic View. Taken with HAYEAR™ HY-150X USC Microscope

2.1: Varied Rod Diameter

Again, the same three rod diameters were used in the creation of the contraction muscles – 0.035", 0.041", and 0.055". The loaded lengths of the three muscles with a 100g deadweight were 91.4mm, 93.8mm and 95.4mm respectively. Spring index was calculated again using Equation 4-1. The spring index of the 0.035" rod diameter muscle was 2.98, the spring index of the 0.041" rod diameter muscle was 3.23 and the spring index of the 0.055" rod diameter muscle was 3.63. These values are the same as the expansion muscles because spring index is a calculation of mean diameter and fiber diameter – both of which are the same regardless of whether the muscle is contraction or expansion. A current of 0.18A was applied to the muscles with a heating time of 15 seconds and a cooling time of 45 seconds. This was repeated five times for a total duration of 300 seconds.

Rod Diameter	Spring Index	Loaded Length	Deadweight	Current	Heating Time	Cooling Time
0.035”	2.98	91.4mm	100g	0.18A	15s	45s
0.041”	3.23	93.8mm				
0.055”	3.63	95.4mm				

Table 4-7: Experimental Conditions for Contraction Muscles Varied Rod Diameter Experiment

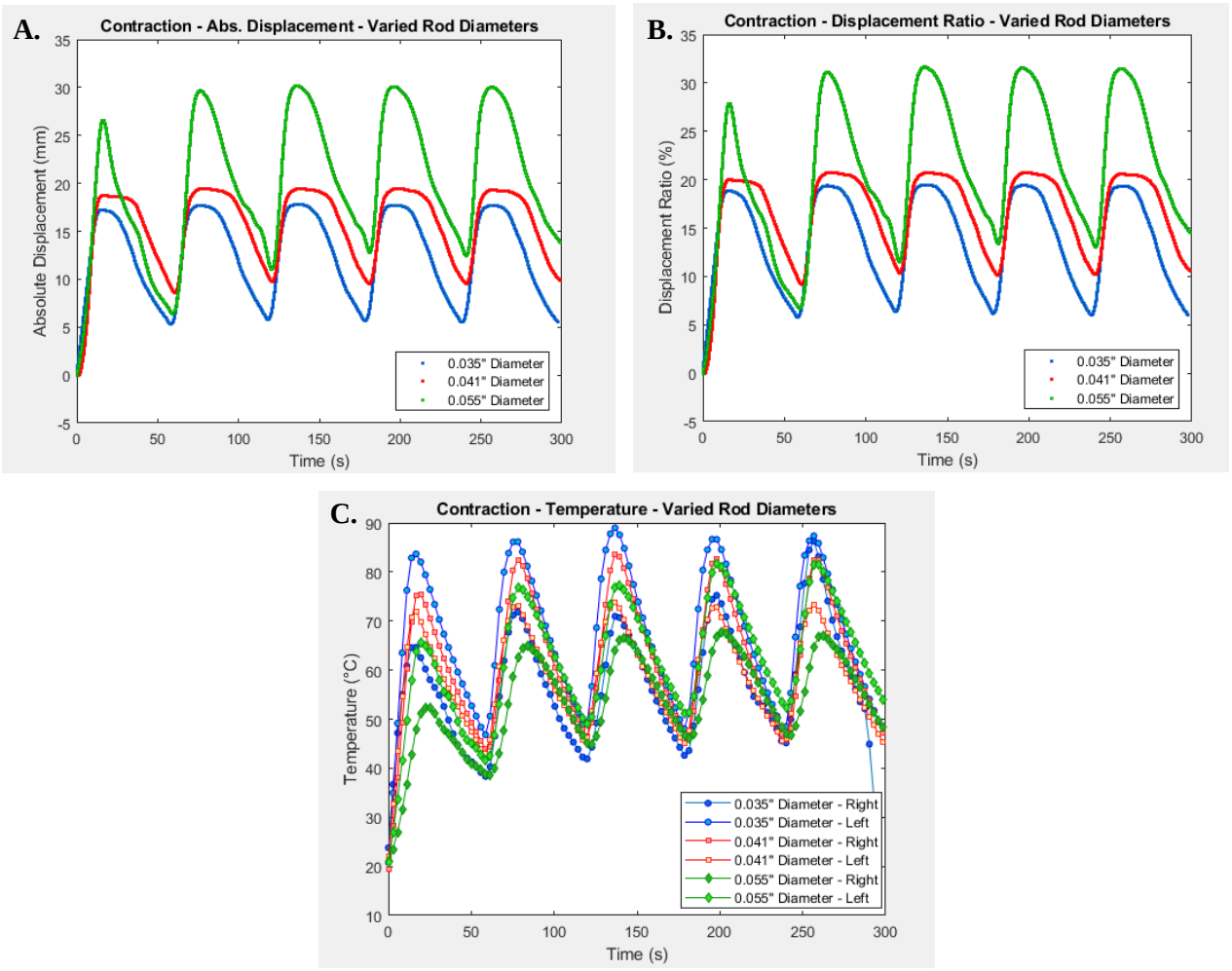

Figure 4-9: Contraction Muscles – Varied Rod Diameters (a) Absolute Displacement produced (b) Displacement Ratio calculated as a ratio of displacement produced and muscle length (c) Probe Temperatures at the left and right of each muscle

The results showed in Figure 4-9 are similar to the ones from the varied rod diameter experiment done on the expansion muscles. Graphs A and B clearly show the trend of higher displacement with larger rod diameter. The 0.055” rod muscle once again provided the largest absolute displacement of 31.2mm, as well as the largest displacement ratio of 32.9%. The 0.041” rod muscle had an absolute displacement of 19.5 mm and a displacement ratio of 20.7%, and the 0.035” rod muscle had an absolute displacement of 17.7 mm and a displacement ratio of 19.2%. Interestingly, the 0.055” rod muscle provided the lowest peak temperature value – directly contrasting the 0.055” rod expansion muscle. The 0.035” rod muscle featured a maximum temperature of 89.1 degrees Celsius, the 0.041” rod muscle reached a maximum temperature of 83.9 degrees Celsius, and the 0.055” rod muscle reached a maximum temperature of 81.6 degrees Celsius.

2.2: Isotonic Test (Varied Dead Weight)

The 0.055” rod muscle was used for this experiment and all following experiment due to its higher displacement produced comparatively. Three deadweights were used for the contraction muscles much like the expansion setup, however, because these weights were not applied directly atop the muscles but rather attached via a pulley system, they could be heavier than the ones used in the expansion experiment. The weights used for the contraction varied dead weight experiment were 50g, 100g, and 150g, and a current of 0.18A was used. Heating time as 15 seconds, and cooling time was 45 seconds. This was repeated five times for a total duration of 300 seconds. The preloaded lengths of the muscle with the three weights were as follows: 50 g – 91.5mm, 100g – 93.8mm, 150g – 94.9mm.

Rod Diameter	Loaded Length	Deadweight	Current	Heating Time	Cooling Time
0.055”	91.5mm	50g	0.18A	15s	45s
	93.8mm	100g			
	94.9mm	150g			

Table 4-8: Experimental Conditions for Contraction Muscles Isotonic Experiment

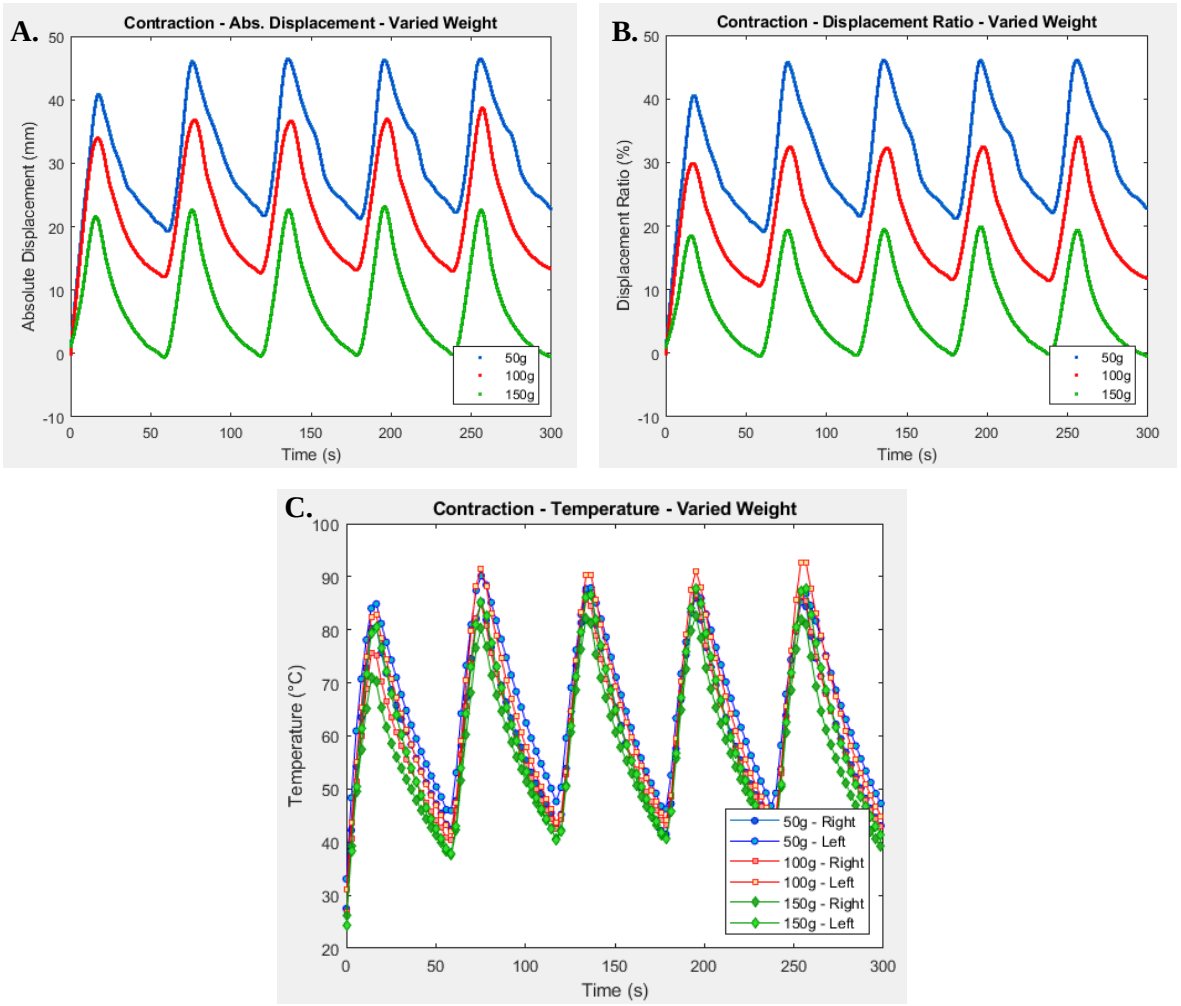

Figure 4-10: Contraction Muscle – Varied Resistance Dead Weight (a) Absolute Displacement produced (b) Displacement Ratio calculated as a ratio of displacement produced and muscle length (c) Probe Temperatures at the left and right of each muscle

Again, there is a clear relationship between the deadweight and the displacement produced. The lightest deadweight – 50g – produced an absolute displacement of 45.8mm and a displacement ratio of 45.5%. The second heaviest deadweight – 100g – produced an absolute displacement of 38.9mm and a displacement ratio of 34.3%. The heaviest deadweight – 150g – produced an absolute displacement of 23.6mm and a displacement ratio of 20.5%. There is no clear relationship between the weight of the deadweight and the temperature produced. All deadweights produced a maximum temperature within a range of 89 and 93 degrees Celsius.

2.3: Varied Current

The third test was done to determine the relationship between currents and displacement/temperature. The three varied currents used were the same was the three used in the expansion experiment – 0.18A, 0.20A, and 0.22A. A 50g deadweight was used for this experiment. The preloaded length of the 0.055" rod muscle was the same for all currents at 109.88mm. The same cycle was used for this experiment – 15 seconds of heating and 45 seconds of cooling five times for a total time of 300 seconds. Voltage was also measured for this experiment.

Rod Diameter	**Loaded Length**	**Deadweight**	**Current**	**Heating Time**	**Cooling Time**
0.055"	109.88mm	50g	0.18A	15s	45s
			0.20A		
			0.22A		

Table 4-9: Experimental Conditions for Contraction Muscles Varied Current Experiment

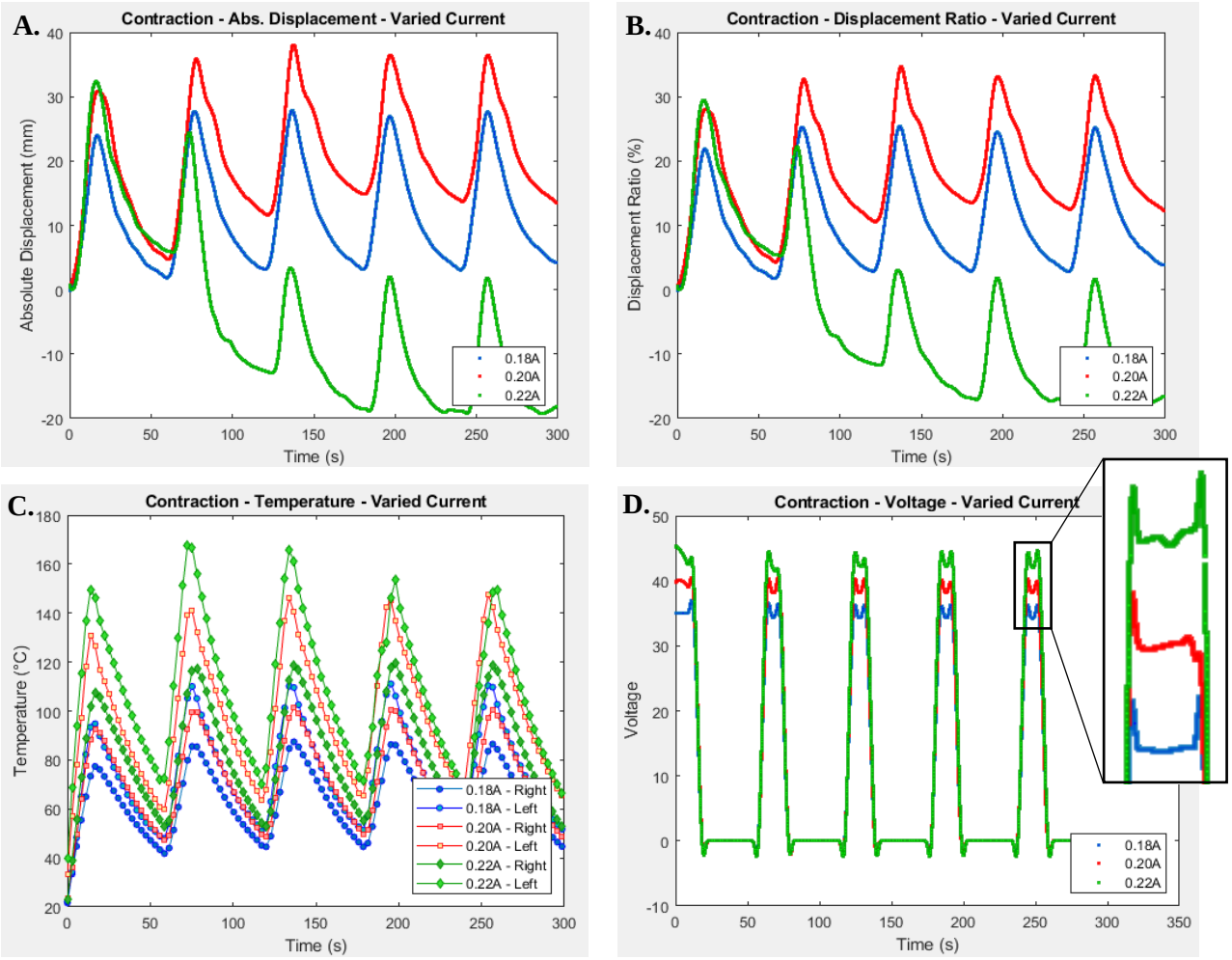

Figure 4-11: Contraction Muscle – Varied Current (a) Absolute Displacement produced (b) Displacement Ratio calculated as a ratio of displacement produced and muscle length (c) Probe Temperatures at the left and right of each muscle (d) Voltage produced

Clearly it can be noted that there was significant muscle degradation/failure evident when looking at graphs A and B. This data is valuable because it clearly shows the amperage limit with a 15 second heating period for the 0.055" rod muscle. Any subsequent operation of these contraction muscles should utilize a current of no higher than 0.20A for the same heating duration, which produced an absolute displacement of 38.4mm and a displacement ratio of 35%. The 0.18A experiment yielded an absolute displacement of 28mm and a displacement ratio of 25.5%. There is a clear relationship between temperature and current as shown in graph C. The

0.22A cycle, although highly degraded still produced consistently high temperatures with a peak temperature of 169.4 degrees Celsius. The glass transition temperature of the Eagle Claw™ 80 lb-test nylon monofilament fishing line is only 70 degrees C, with the melting point being 230 degrees C. After training the muscles, this melting point is likely reduced, causing degradation and melting when exposed to temperatures seen in the 0.22A cycle. The 0.20A cycle produced a peak temperature of 150.3 degrees Celsius, and the 0.18A cycle produced a peak temperature of 113 degrees Celsius. The voltages were measure as 44.5V for 0.22A, 40.4V for 0.20A, and 37V for 0.18A.

2.4: Fatigue Test/Pulse Test

The fatigue test, like stated previously in section 1.4 regarding expansion muscles, was used to determine the point at which the muscles degraded to a point where they were no longer usable. Established work by Lianjun Wu, Indrajeet Chauhan, and Yonas Tadesse in a paper published in Advanced Materials Technologies was referenced (Wu, Chauhan, and Tadesse 2018). Their test setup is similar to what is used in this research for contraction muscles. The setup can be seen in Figure 4-12.

This test was combined with the pulse test. A pulsed current of 0.50A was induced into the muscle for 1 second while the cooling cycle was 100 seconds. This cycle was repeated 2300 times for a total duration of 232,300 seconds. A dead weight of 50 grams was used for this test.

Loaded Length	**Deadweight**	**Current**	**Heating Time**	**Cooling Time**
50mm	50g	0.50A	1s	100s

Table 4-10: Experimental Conditions for Contraction Muscles Fatigue Experiment

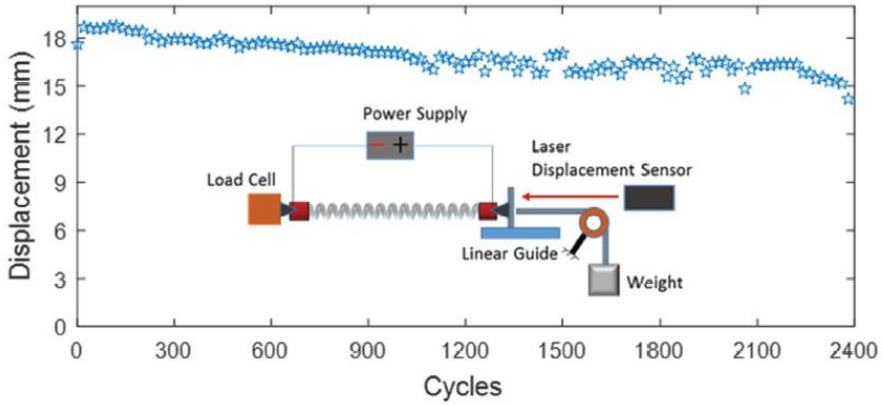

Figure 4-12: Contraction Muscle – Fatigue/Pulse Test Setup and Acquired Data (Wu, Chauhan, and Tadesse 2018)

Figure 4-12 shows the slight degradation in performance. The displacement near the beginning of the test peaked at 18.9mm, and near the end of the test only around 15.4mm.

2.5: Improper Training – Pulse Test

Equation 4-2 (ignoring heat loss) was again used to determine the energy needed to match the typical 15 second heating period used in prior experiments for the 0.55" rod muscle. 0.70A was found to be the current needed to do this, so testing was done starting at 0.50A moving up in increments of 0.05A to determine at which point the muscles would begin to melt or otherwise fail. For the contraction muscles, this point was found to be 0.60A, so the test was done at the following currents for 1 second of heating – 0.45A, 0.50A, and 0.55A. The rest period of 45 seconds remained, as well as the typical five cycle repeated setup used in the previous experiments. The total experiment time was 230 seconds, a deadweight of 50g was used, and the preloaded length for all three currents was 95.2mm.

Rod Diameter	Loaded Length	Deadweight	Current	Heating Time	Cooling Time
0.055”	95.2mm	50g	0.45A	1s	45s
			0.50A		
			0.55A		

Table 4-11: Experimental Conditions for Contraction Muscles Pulse Experiment

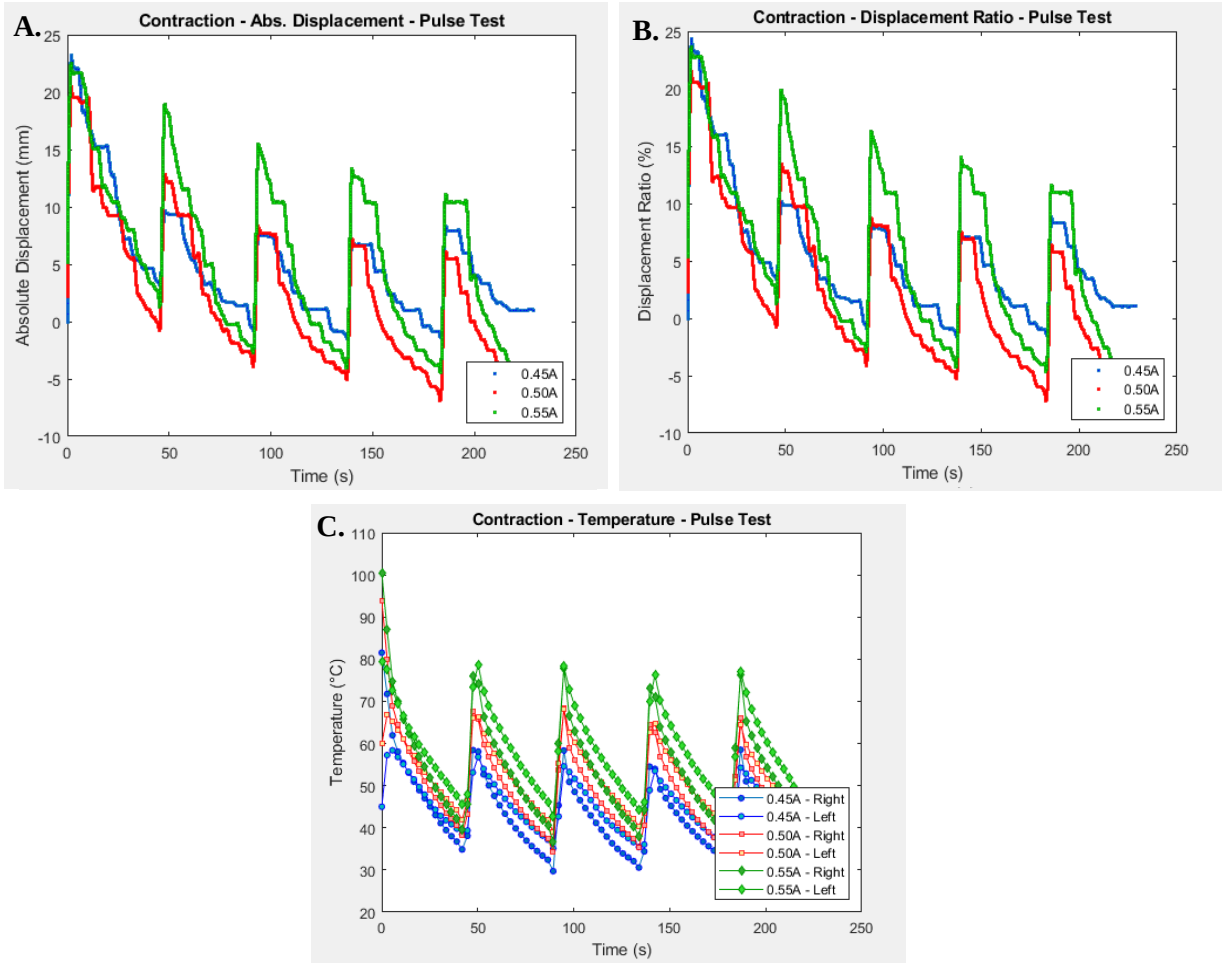

Figure 4-13: Contraction Muscle – Pulse Test with Improper Training (a) Absolute Displacement produced (b) Displacement Ratio calculated as a ratio of displacement produced and muscle length (c) Probe Temperatures at the left and right of each muscle

Figure 4-13 shows the effect of improper training on muscles. Training must be done for at least 10 cycles on each muscle before testing at the desired current or deadweight conditions.

Because the muscles tested here were trained at lower currents (0.18A – 0.20A), they were not properly prepared for the much higher currents. This causes the downward trend in displacement seen in graphs A and B, while the temperature in graph C peaks around the same point each cycle.

The data collected from these experiments was compiled together and can be seen in Table 4-12 barring the fatigue and pulse test data.

Contraction Muscle Data					
	Parameters	**Max. Abs. Displacement**	**Max. Displacement Ratio**	**Max. Temperature**	**Voltage**
Varied Rod Diameter	0.035"	17.7mm	19.2%	89.1°C	-
	0.041"	19.5mm	20.7%	83.9°C	-
	0.055"	31.2mm	32.9%	81.6°C	-
Varied Dead Weight	50g	45.8mm	45.5%	90.8°C	-
	100g	38.9mm	34.3%	92.8°C	-
	150g	23.6mm	20.5%	89°C	-
Varied Current	0.18A	28mm	25.5%	113°C	37.0V
	0.20A	38.4mm	35.0%	150.3°C	40.4V
	0.22A	31.7mm	28.8%	169.4°C	44.5V

Table 4-12: Contraction Muscle Data

Part 3: Soft Earthworm Robot Prototype Data

As mentioned in the methodology section, there were two test setups used to collect data on the earthworm robot prototype. The second setup, pictured in Figure 4-14, can simply be altered to test under no load conditions by detaching the deadweight from the prototype. When the dead weight is desired again, it can easily be reattached to the prototype via fishing line.

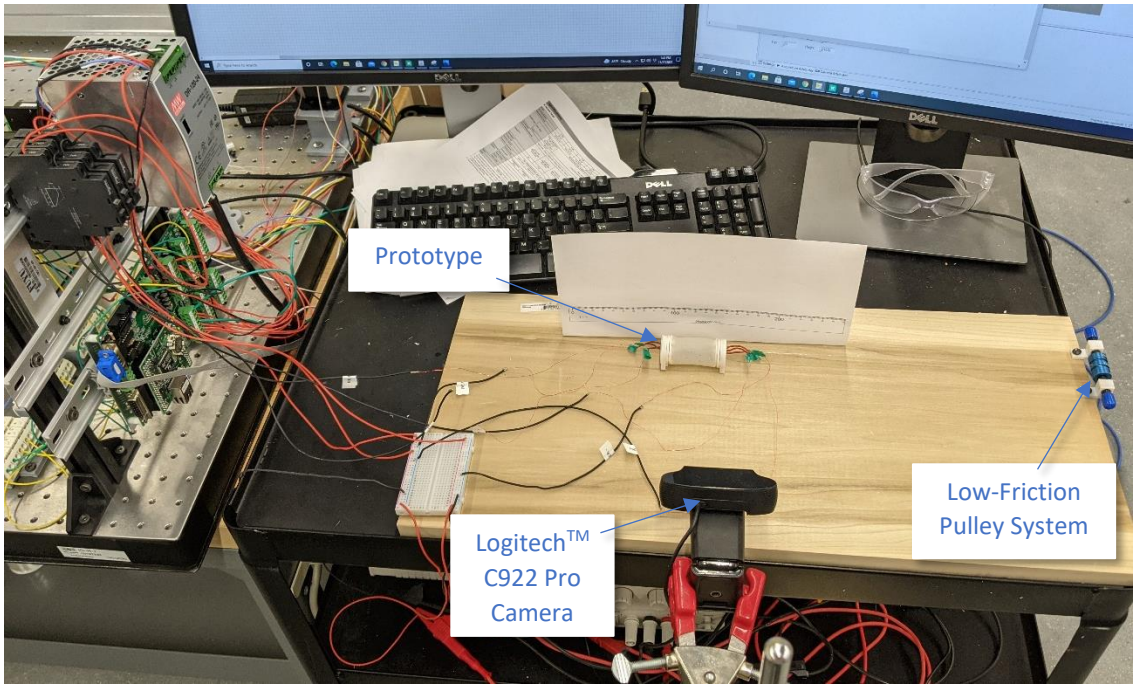

Figure 4-14: Test Setup used for Prototype Data Collection

3.1: Prototype Data under No Load

Testing for the no load experiment was done at 0.28A, 0.32A, and a maximum of 0.36A (any higher and there is a risk of permanent muscle damage) induced into the central actuator. The three varied amperage tests and their corresponding pictures at 0 seconds (initial state), 30 seconds (peak central actuator state), and 120 seconds (final state) can be seen in Figures 3-15, 3-16, and 3-17.

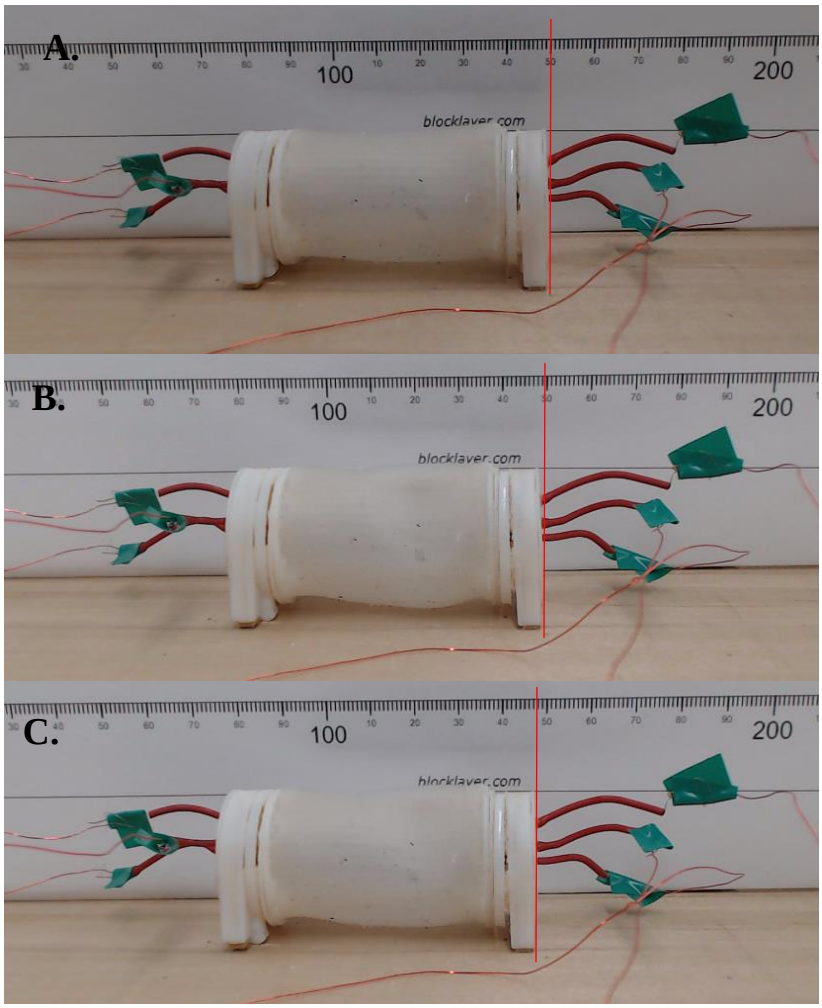

Figure 4-15: 0.28A Current at (a) 0 seconds, (b) 30 seconds, and (c) 120 seconds

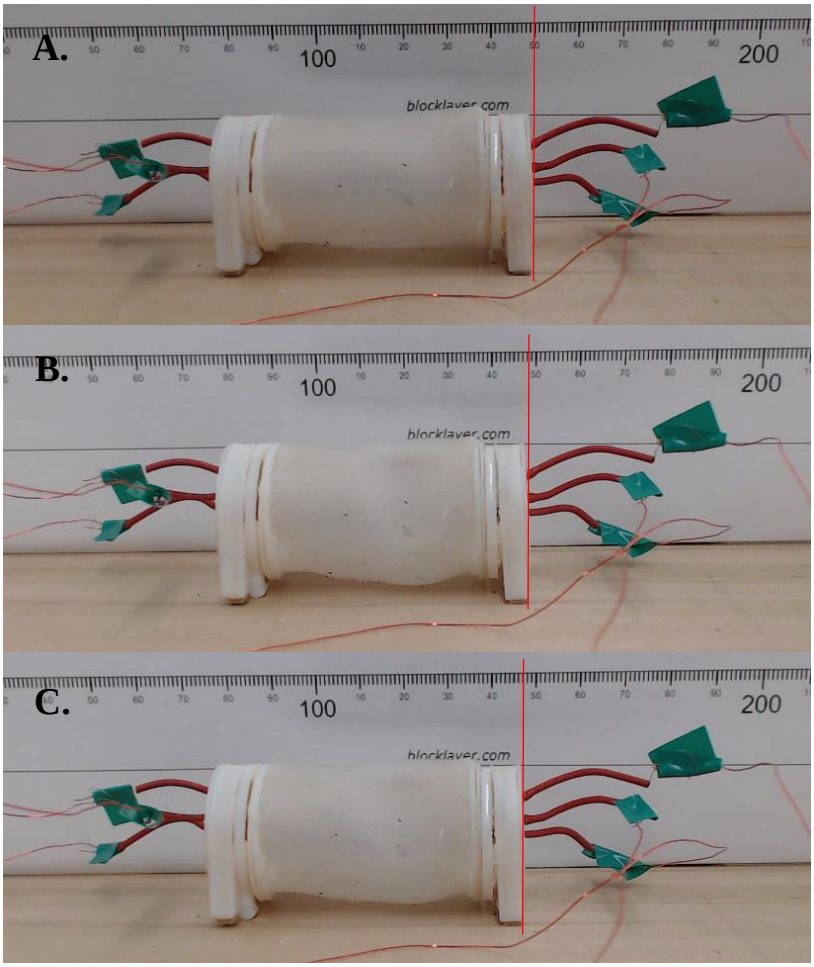

Figure 4-16: 0.32A Current at (a) 0 seconds, (b) 30 seconds, and (c) 120 seconds

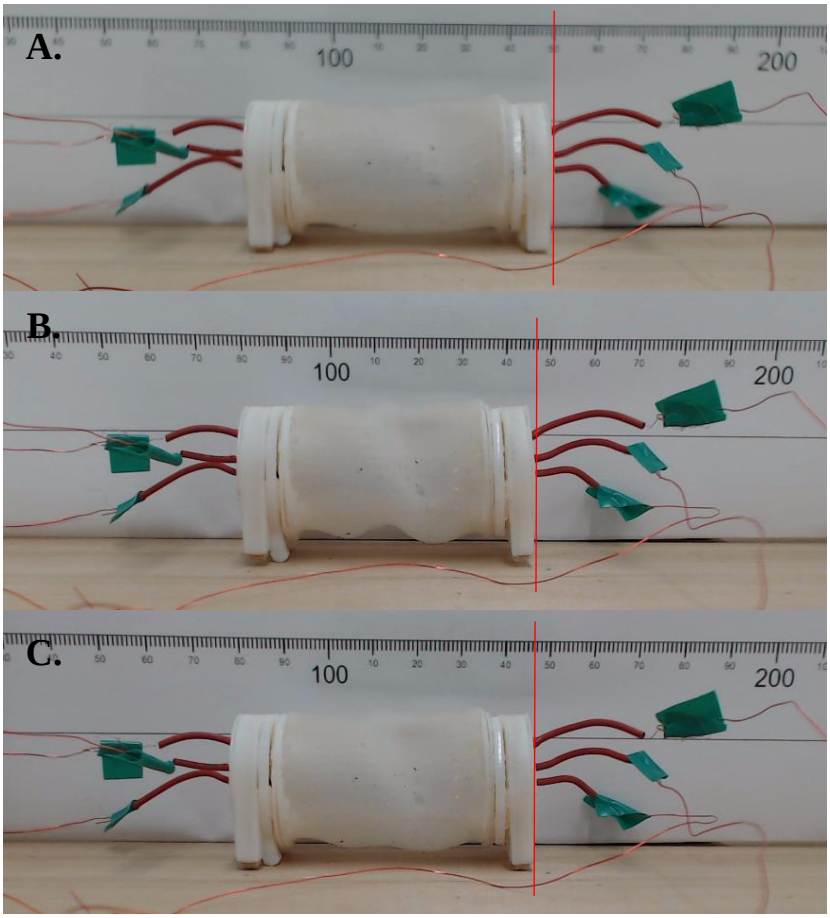

Figure 4-17: 0.36A Current at (a) 0 seconds, (b) 30 seconds, and (c) 120 seconds

The data gathered from these three tests was compiled into Table 4-13. The distance between the red displacement line in frames A and B in the Figures was used to find axial deformation, and the distance between the red displacement line in frames A and C were used to find total displacement and velocity.

Current	Max. Axial Deformation	Total Displacement	Velocity
0.28A	0.5mm	2.1mm	1.05mm/min
0.32A	1.2mm	2.8mm	1.4mm/min
0.36A	2.8mm	3.1mm	1.55mm/min

Table 4-13: Prototype Data under no Load

3.2: Prototype Data under Varied Load

The largest axial deformation, total displacement, and velocity corresponded to the highest induced current – 0.36A. For this reason, 0.36A was used for all subsequent tests under a loaded condition. The goal of this experiment was to determine how heavy of a deadweight the prototype can handle before it halts its movement or begins to move in the wrong direction. The initial deadweight used was 5g, and from there more weight was added in 2.5g increments until the prototype could no longer move. The data collected can be seen in Figures 4-18, 4-19, and 4-20.

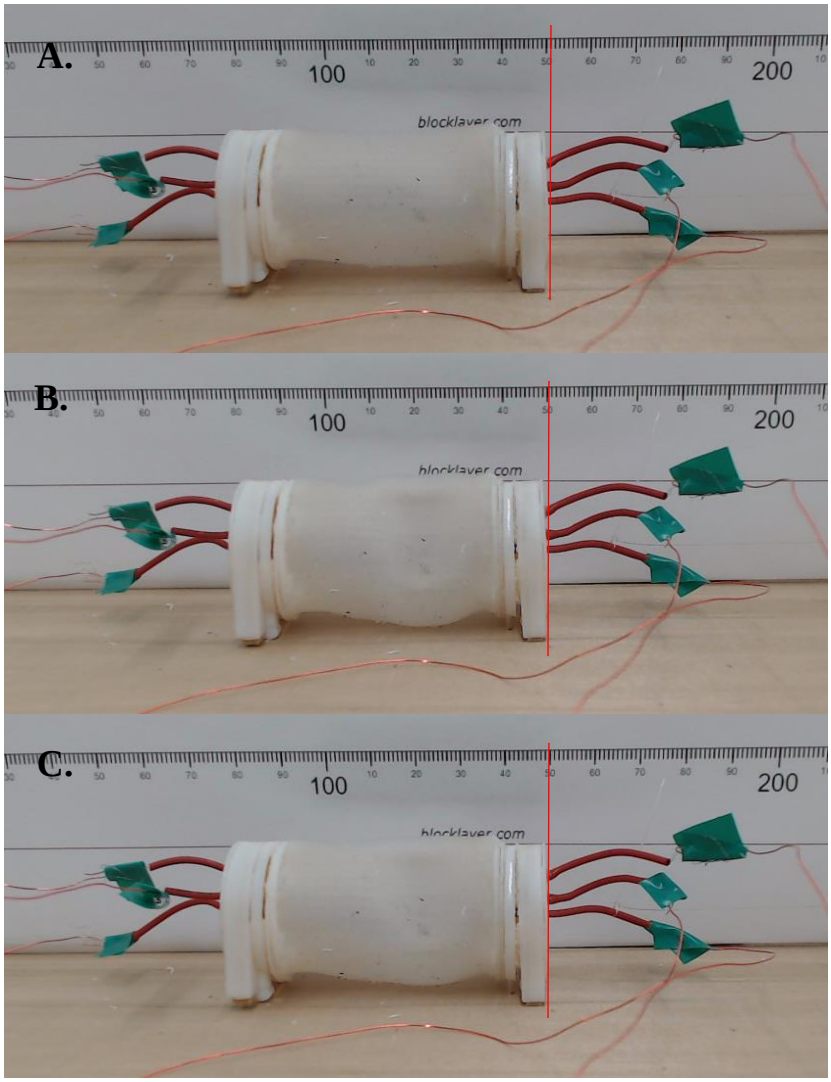

Figure 4-18: 0.36A Current with 5g Deadweight at (a) 0 seconds, (b) 30 seconds, and (c) 120 seconds

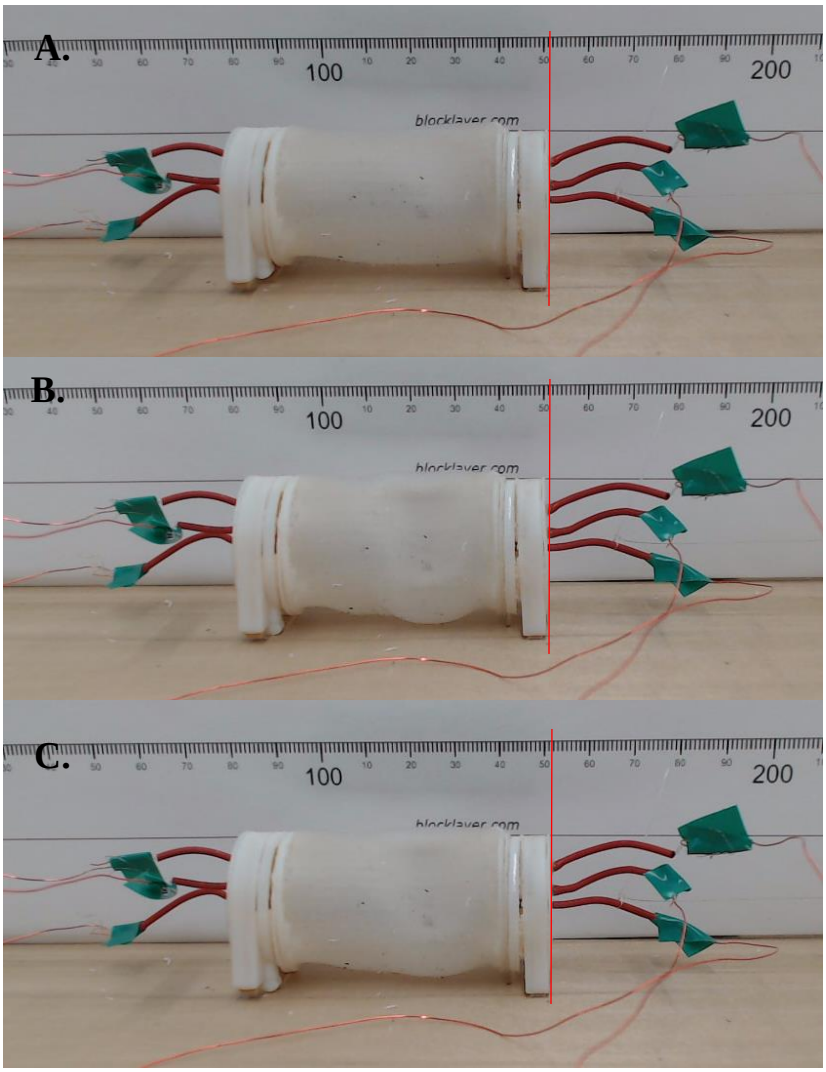

Figure 4-19: 0.36A Current with 7.5g Deadweight at (a) 0 seconds, (b) 30 seconds, and (c) 120 seconds

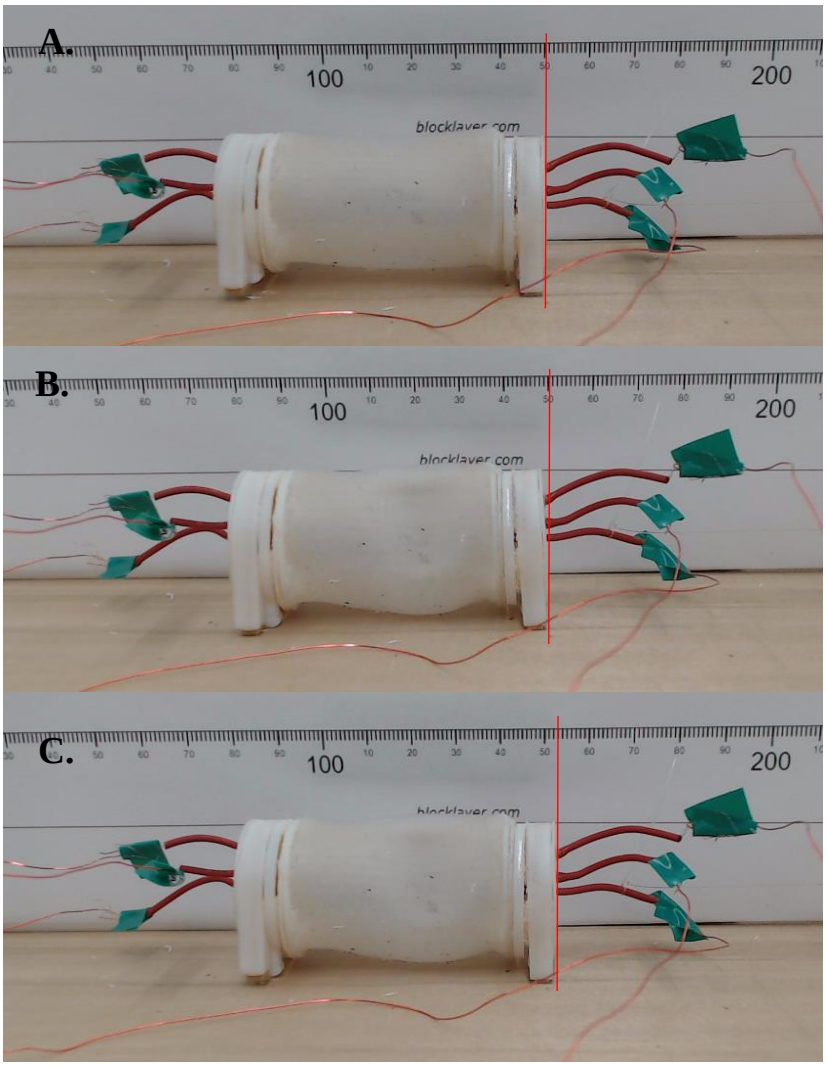

Figure 4-20: 0.36A Current with 10g Deadweight at (a) 0 seconds, (b) 30 seconds, and (c) 120 seconds

Again, measuring the difference between the red displacement lines in each picture was used to determine maximum axial deformation, displacement, and velocity under a loaded condition. It was observed that at 7.5g, the prototype was unable to move in the correct direction, and at 10g, the prototype began to move backwards. The data from this experiment was compiled into Table 4-14.

Deadweight	Max. Axial Deformation	Total Displacement	Velocity
5g	0.4mm	1.1mm	0.55mm/min
7.5g	0mm	0mm	-
10g	-0.1mm	-2.7mm	-

Table 4-14: Prototype Data under Varied Load

CHAPTER 5
CONCLUSION

The goal of this thesis is to provide an overview of the current landscape of soft robotics, biomimetic earthworm robots, and artificial muscles as well as to introduce a new and innovative soft earthworm robot into the field that utilizes both expansion and contraction artificial muscles. Accomplishing this involved comprehensive research in the aforementioned fields, testing and data collection on the characteristics of fishing line artificial muscles, and categorization for the final earthworm robot prototype.

Data collection was done initially in 5 categories for expansion and contraction muscles - varied rod diameter, varied dead weight, varied current, a 1000 cycle fatigue test, and a high current but low activation time pulse test. For expansion muscles, it was found that the 0.055" rod diameter muscle produced the largest displacement compared to 0.041" and 0.035" rod diameter muscles, as well as the largest peak temperature. The varied deadweight test showed the effect of 20g, 40, and 60g weights on a 0.055" rod diameter muscle with displacements being lower for heavier weights and peak temperatures being higher for heavier weights. The varied current experiment predictably showed that higher induced currents meant higher displacements and higher peak temperatures. The fatigue test showed the effects of nylon and NiCr heating wire degradation as well as long term performance of the muscle. The pulse test showed the ratio of higher pulsed currents on displacement as well as peak temperature - higher pulsed currents unsurprisingly leading to higher displacements and peak temperatures.

These tests were repeated for contraction muscles. The varied rod diameter tests once again confirmed that the 0.055" rod diameter muscles produced the higher displacement and

temperature. The varied dead weight tests showed the relationship between increasing weight and increased displacement and temperature – this time with 50g, 100g, and 150, deadweights. The heavier the deadweight, the lower the peak displacement and the higher the peak temperature produced. The varied current experiment again used the same 3 induced currents – 0.18A, 0.20A, and 0.22A – with the same results as the expansion experiment – higher current relates to higher maximum displacements and temperatures. This test also showed the maximum current that should be applied before the nylon fishing line reaches its melting point. The fatigue test was taken from prior research and shows again the slight degradation of contraction artificial muscles over long cyclic periods. The pulse test showed the relationship between higher amperage pulses and higher displacements and higher peak temperatures.

After designing and producing a working soft earthworm prototype, various metrics were obtained to properly characterize said prototype. These metrics were axial deformation, velocity, and maximum payload capability. Two major tests were done – one under no load and one under varied load. The first test was repeated three times varying induced currents in the central actuator at 0.28A, 0.32A, and 0.36A. No higher current than 0.36A was used to avoid damaging the artificial muscles. Through this experiment it was found that higher induced current corresponded to higher axial deformation and velocity. 0.28A produced an axial deformation of 0.5mm and a velocity of 1.05mm/min. 0.32A produced an axial deformation of 1.2mm and a velocity of 1.4mm/min. Finally, 0.36A produced an axial deformation of 1.5mm and a velocity of 1.85mm/min.

To measure the maximum payload that the prototype could tow, varying deadweights were attached to it until its locomotion was halted. These deadweights started at 5g and were increased at 2.5g intervals. A 5g deadweight produced an axial deformation of 0.4mm and a

velocity of 0.55mm/min, a 7.5g deadweight produced an axial deformation of 0mm and a velocity of 0mm/min, and at 10g, the prototype began to move in the wrong direction.

Although the scope of this thesis was relatively large – touching on many varying topics including artificial muscles, automation, multi-material 3D printing, and more – there are still many avenues that can be expanded on for future research or for a doctoral thesis. One major component that could be added to this research is in the form of torsional artificial muscles. These muscles are produced in a manner similar to the expansion and contraction muscles, however they are not coiled around a rod. Instead, they are simply twisted and then wrapped with conductive wire before they are allowed to sit stationary for a predetermined waiting period. This waiting period, which should be no shorter than 7 -10 days depending on the thickness of the fishing line, essentially accomplishes what the oven heating accomplishes for the contraction or expansions muscles – it allows the shape of the muscle to set. When these torsional muscles are heated, they produce a rotational torque force that can be used to steer future earthworm robot prototypes. Collecting data for these muscles would require the use of a torque transducer and rotary encoder.

Another major avenue that could be explored further is the topic of multi-material simultaneous 3D printing. As discussed in part 3 of the methodology section, for this research a hollow PVA mold was first printed with a traditional 3D print head, and then a static mixing silicone head was moved above the mold to fill the mold with uncured silicone. Another method - which could be a paper in itself - is to alternate layer-by-layer between the PVA print head and the silicone print head during the print. This would allow for a highly consistent and controllable 3D print that could also be used to create more complex mold geometries.

Finally, many further applications of this soft earthworm robot could be realized with untethered locomotion. The inclusion of an onboard power source and micro controller would allow for this, and is certainly feasible if implemented within an extended end cap design.

Possible additions to this research that could allow for a more comprehensive paper include: determining the relationship between fishing line lb.-test and artificial muscle performance, determining the relationship between heating wire material and artificial muscle performance, viewing pre-trained, post-trained, and fatigued muscles under a microscope to observe changes at the molecular level, and determining the effect of surface material and prototype axial deformation/velocity.

REFERENCES

Alici, Gursel. 2018. 'Softer is Harder: What Differentiates Soft Robotics from Hard Robotics?', *MRS Advances*, 3: 1-12.

Chatterjee, S., R. Niiyama, and Y. Kawahara. 2017. "Design and Development of a Soft Robotic Earthworm with Hydrostatic Skeleton." In *2017 IEEE International Conference on Robotics and Biomimetics (ROBIO)*, 1-6.

El-Atab, Nazek, Rishabh B. Mishra, Fhad Al-Modaf, Lana Joharji, Aljohara A. Alsharif, Haneen Alamoudi, Marlon Diaz, Nadeem Qaiser, and Muhammad Mustafa Hussain. 2020. 'Soft Actuators for Soft Robotic Applications: A Review', *Advanced Intelligent Systems*, 2: 2000128.

Fujiwara, A., T. Nakatake, N. Tadami, K. Isaka, Y. Yamada, H. Sawada, T. Nakarnura, and T. Kubota. 2018. "Development of Both-Ends Supported Flexible Auger for Lunar Earthworm-Type Excavation Robot LEAVO." In *2018 IEEE/ASME International Conference on Advanced Intelligent Mechatronics (AIM)*, 924-29.

Ge, Joey Z., Ariel A. Calderón, Longlong Chang, and Néstor O. Pérez-Arancibia. 2019. 'An earthworm-inspired friction-controlled soft robot capable of bidirectional locomotion', *Bioinspiration & Biomimetics*, 14: 036004.

Goldoni, Riccardo, Yasemin Ozkan-Aydin, Yun-Soung Kim, Jongsu Kim, Nathan Zavanelli, Musa Mahmood, Bangyuan Liu, Frank L. Hammond, Daniel I. Goldman, and Woon-Hong Yeo. 2020. 'Stretchable Nanocomposite Sensors, Nanomembrane Interconnectors, and Wireless Electronics toward Feedback–Loop Control of a Soft Earthworm Robot', *ACS Applied Materials & Interfaces*, 12: 43388-97.

Haines, Carter S., Márcio D. Lima, Na Li, Geoffrey M. Spinks, Javad Foroughi, John D. W. Madden, Shi Hyeong Kim, Shaoli Fang, Mônica Jung de Andrade, Fatma Göktepe, Özer Göktepe, Seyed M. Mirvakili, Sina Naficy, Xavier Lepró, Jiyoung Oh, Mikhail E. Kozlov, Seon Jeong Kim, Xiuru Xu, Benjamin J. Swedlove, Gordon G. Wallace, and Ray H. Baughman. 2014. 'Artificial Muscles from Fishing Line and Sewing Thread', *Science*, 343: 868.

Hayato, Omori, Hayakawa Takeshi, and T. Nakamura. 2008. "Locomotion and turning patterns of a peristaltic crawling earthworm robot composed of flexible units." In *2008 IEEE/RSJ International Conference on Intelligent Robots and Systems*, 1630-35.

Heung, H., P. W. Y. Chiu, and Z. Li. 2016. "Design and prototyping of a soft earthworm-like robot targeted for GI tract inspection." In *2016 IEEE International Conference on Robotics and Biomimetics (ROBIO)*, 497-502.

Isaka, K., K. Tsumura, T. Watanabe, W. Toyama, M. Sugesawa, Y. Yamada, H. Yoshida, and T. Nakamura. 2019. 'Development of Underwater Drilling Robot Based on Earthworm Locomotion', *IEEE Access*, 7: 103127-41.

Joyee, Erina B., and Yayue Pan. 2019. 'A Fully Three-Dimensional Printed Inchworm-Inspired Soft Robot with Magnetic Actuation', *Soft Robotics*, 6: 333-45.

Kandhari, A., Y. Huang, K. A. Daltorio, H. J. Chiel, and R. D. Quinn. 2018. 'Body stiffness in orthogonal directions oppositely affects worm-like robot turning and straight-line locomotion', *Bioinspiration & Biomimetics*, 13: 026003.

Kim, Byungkyu, Moon Gu Lee, Young Pyo Lee, YongIn Kim, and GeunHo Lee. 2006. 'An earthworm-like micro robot using shape memory alloy actuator', *Sensors and Actuators A: Physical*, 125: 429-37.

Liu, B., Y. Ozkan-Aydin, D. I. Goldman, and F. L. Hammond. 2019. "Kirigami Skin Improves Soft Earthworm Robot Anchoring and Locomotion Under Cohesive Soil." In *2019 2nd IEEE International Conference on Soft Robotics (RoboSoft)*, 828-33.

Marchese, Andrew D., Robert K. Katzschmann, and Daniela Rus. 2015. 'A Recipe for Soft Fluidic Elastomer Robots', *Soft Robotics*, 2: 7-25.

Naclerio, N. D., C. M. Hubicki, Y. O. Aydin, D. I. Goldman, and E. W. Hawkes. 2018. "Soft Robotic Burrowing Device with Tip-Extension and Granular Fluidization." In *2018 IEEE/RSJ International Conference on Intelligent Robots and Systems (IROS)*, 5918-23.

Nagaoka, K., T. Kubota, M. Otsuki, and S. Tanaka. 2008. "Experimental study on autonomous burrowing screw robot for subsurface exploration on the Moon." In *2008 IEEE/RSJ International Conference on Intelligent Robots and Systems*, 4104-09.

Nemitz, Markus P., Pavel Mihaylov, Thomas W. Barraclough, Dylan Ross, and Adam A. Stokes. 2016. 'Using Voice Coils to Actuate Modular Soft Robots: Wormbot, an Example', *Soft Robotics*, 3: 198-204.

Saga, Norihiko, and Taro Nakamura. 2004. 'Development of a peristaltic crawling robot using magnetic fluid on the basis of the locomotion mechanism of the earthworm', *Smart Materials and Structures*, 13: 566-69.

Tadami, N., K. Isaka, T. Nakatake, A. Tujiwara, Y. Yamada, T. Nakamura, M. Sugesawa, and H. Yoshida. 2018. "Underwater Excavation by Excavation Robot Equipped with Propulsion Unit Based on Earthworm Setae." In *2018 IEEE International Conference on Robotics and Biomimetics (ROBIO)*, 51-58.

Takashi, Kato, Iwanaga Tomohide, and Muranaka and Yoichi. 2006. *Journal of Robotics and Mechatronics VL - 18 IS - 3 SP - 299 EP - 304 PY - 2006 DO - 10.20965/jrm.2006.p0299 ER -*.

Wu, Lianjun, Indrajeet Chauhan, and Yonas Tadesse. 2018. 'A Novel Soft Actuator for the Musculoskeletal System', *Advanced Materials Technologies*, 3: 1700359.

Xavier, M. S., A. J. Fleming, and Y. K. Yong. 2019. "Experimental Characterisation of Hydraulic Fiber-Reinforced Soft Actuators for Worm-Like Robots." In *2019 7th International Conference on Control, Mechatronics and Automation (ICCMA)*, 204-09.

Yamashita, A., K. Matsui, R. Kawanishi, T. Kaneko, T. Murakami, H. Omori, T. Nakamura, and H. Asama. 2011. "Self-localization and 3-D model construction of pipe by earthworm robot equipped with omni-directional rangefinder." In *2011 IEEE International Conference on Robotics and Biomimetics*, 1017-23.

Zhang, Chao, Pingan Zhu, Yangqiao Lin, Zhongdong Jiao, and Jun Zou. 2020. 'Modular Soft Robotics: Modular Units, Connection Mechanisms, and Applications', *Advanced Intelligent Systems*, 2: 1900166.

Zhang, Jinhua, Tao Wang, Jin Wang, Michael Yu Wang, Baotong Li, John X. J. Zhang, and Jun Hong. 2020. 'Geometric Confined Pneumatic Soft–Rigid Hybrid Actuators', *Soft Robotics*, 7: 574-82.